GEOLOGICA ULTRAIECTINA

Mededelingen van de
Faculteit Aardwetenschappen
Universiteit Utrecht

No. 125

ASPECTS OF HIGH RESOLUTION MARINE SEISMICS

NICO VERBEEK

GEOLOGICA ULTRAIECTINA

Mededelingen van de
Faculteit Aardwetenschappen
Universiteit Utrecht

No. 125

ASPECTS OF HIGH RESOLUTION MARINE SEISMICS

NICO VERBEEK

CIP-DATA KONINKLIJKE BIBLIOTHEEK, DEN HAAG

Verbeek, Nico Henricus

Aspects of high resolution marine seismics / Nico Henricus Verbeek. - Utrecht : Faculteit Aardwetenschappen, Universiteit Utrecht. - (Geologica Ultraiectina, ISSN 0072-1026 ; no. 125)
Thesis Universiteit Utrecht. - With ref. - With summary in Dutch
ISBN 90-71577-79-1
Subject headings: high resolution / marine seismics.

Aspects of high resolution marine seismics

Aspecten van hoge resolutie mariene seismiek

(met een samenvatting in het Nederlands)

PROEFSCHRIFT

TER VERKRIJGING VAN DE GRAAD VAN DOCTOR
AAN DE UNIVERSITEIT UTRECHT,
OP GEZAG VAN DE RECTOR MAGNIFICUS PROF. DR J.A. VAN GINKEL,
INGEVOLGE HET BESLUIT VAN HET COLLEGE VAN DECANEN
IN HET OPENBAAR TE VERDEDIGEN OP
WOENSDAG 29 MAART 1995 DES NAMIDDAGS TE 12.45 UUR

DOOR

NICO HENRICUS VERBEEK

GEBOREN OP 7 SEPTEMBER 1966 TE GELDROP

PROMOTOR: PROF. DR K. HELBIG

The research described in this thesis was carried out at the:

Department of Geophysics
Institute of Earth Sciences
Utrecht University
Budapestlaan 4
3584 CD Utrecht
The Netherlands

Contents

Chapter 2

Chapter 3

Chapter 4

Chapter 5

Introduction and Summary

Reflection seismic methods, widely used in the oil-exploration, can give detailed images of the earth's interior. Application of these methods with strongly enhanced resolution allows detailed imaging of the upper tens of meters of the subsurface. When these methods are applied in water covered areas (such as a lake, river or sea) they are called marine seismics. Practical applications of marine seismic methods can, for example, be found in the fields of dredging, construction and environmental engineering. This thesis deals with some aspects of high resolution marine seismic profiling. The intention is to give an overview of some aspects of high resolution marine seismic profiling. It is not the intention to give a detailed description of all aspects concerning high resolution marine seismic profiling. However, marine seismic sources and deconvolution techniques will be discussed in more detail.

The work in shallow marine high resolution seismic profiling in Utrecht started around 1987. For this work a data acquisition system and a receiver array were designed and built. They are described in Chapter 1 of this thesis. The importance of source-receiver geometry on the signal-to-noise ratio is explained. Noise in the recorded signal can obscure the useful data. Therefore, it is also shown how noise can be reduced during the data acquisition. Furthermore, several commonly used marine seismic sources are described. A detailed knowledge of the source signature is important for some processing steps. Several characteristics of these sources (dominant frequency, bandwidth, directivity and repeatability) are discussed in Chapter 2. Sometimes it is difficult to determine the bandwidth of a source from its spectrum. A method is proposed to calculate the bandwidth from the 'time signal' of the source wavelet.

To get a detailed image of the subsurface a good vertical resolution is required. This has its implication for the acquisition hardware (sources, receivers) and the acquisition parameters. The resolution can also be improved by processing. Assuming that the data can be expressed as a convolution between the source wavelet and a reflector model, deconvolution methods can be used to increase the resolution. In these methods the (complicated) seismic pulse is ideally 'collapsed' into a spike. This is often achieved by writing the data, the source wavelet and the reflector model in a matrix notation and inverting this matrix. The matrix inversion can be sensitive to noise in the data and therefore be unstable.

The method can be stabilized at the expense of a decrease in resolution. In Chapter 3 a deconvolution (inversion) method is presented which is less sensitive to noise. This is achieved by restricting the number of possible reflector positions (columns in the matrix). The resolution is preserved by shifting the reflectors to new positions in each iteration step. Another method which avoids the disadvantages of deconvolution by matrix inversion is presented in Chapter 4. In this chapter a genetic algorithm is used to find the reflector model. The advantage of using genetic algorithms for inversion is that only forward model calculations are needed. Therefore, the inversion is less sensitive to noise in the data.

Some other processing techniques are briefly discussed in Chapters 5, 6 and 7. In these chapters, the last part of this thesis, three case studies are described. The case studies show how high resolution marine seismic profiling was carried out at the Department of Exploration Geophysics in Utrecht. The first case study (Chapter 5) is the North-Sea study. The objective was to map the Holocene sediments north of the Dutch barrier islands. The aim of the second case study (Chapter 6) was to give a detailed description of the upper tens of meters of sediment along the Zeeland-Bridge in the south of the Netherlands. In the third case study (Chapter 7) four seismic sources were compared in the North-Sea Canal. The intention was to find the most suitable source to obtain the best result, in terms of resolution and penetration, in a busy canal.

Chapter 1

Principles of High Resolution Marine Seismic Data Acquisition

1.1 *Introduction*

In this chapter some aspects of shallow marine high resolution seismic profiling are discussed. The aim of this chapter is not to give a complete overview of all general principles, but to explain how high resolution marine seismics at the Department of Exploration Geophysics of Utrecht University is applied. First, a description of some, commonly used, marine seismic sources is given. The seismic sources are important for the vertical resolution of the seismic data. The choice of a seismic source for a survey is discussed as well as some acquisition techniques. Then, some aspects which should be considered when designing a streamer (linear array of hydrophones) and the importance of source-receiver geometry are demonstrated. Next, the development of PC-based data acquisition systems is described as well as the positioning equipment. The last part of this chapter deals with noise during marine seismic data acquisition.

1.2 *Marine Seismic Sources*

In this section some seismic sources, commonly used in high resolution marine seismics, will be discussed. These marine seismic sources can be divided into electrically driven and pneumatically driven sources. In Chapter 2 some aspects of marine seismic sources that are of importance to high resolution marine profiling are discussed.

1.2.1 *Electrical sources*

Electrical sources can be subdivided into sonar transducer sources and impulsive sources. Sonar transducers produce a pressure pulse shaped like a portion of a sinusoid and good control over the pulse shape is possible. The major advantage of using a sonar transducer source is that the pulse shape is well known, which significantly improves the ability to recognize it in the presence of noise. The emitted signal can be correlated with the received signal to increase the resolution and the signal-to-noise ratio.

Impulsive sources release energy in a sudden burst which, ideally, produces a wavelet with a fast first excursion and a short duration. The advantage of impulsive sources is that the produced wavelets can have broad bandwidths and well-defined polarities. The principle disadvantage is that the shape of the wavelet is not always known. Because of this, impulsive wavelets can be difficult to recognize in the presence of noise.

1.2.1.1 *Sonar Transducer*

A transducer intended primarily for the generation of an acoustic output signal in response to an electrical input is called a sonar transducer. Piezo-electric devices transform the electric energy to acoustic energy. The piezo-electric effect is normally associated with the behaviour of certain crystalline materials. An applied electric field results in a mechanical stress in the material proportional to the electric field strength. The sense of the stress reverses, from compression to tension or vice versa, with a reversal of the electric field polarity. Sonar transducers produce a signal shaped like a portion of a sinusoid. The frequency of the sinusoid is largely determined by the resonant frequency of the piezo-electric crystal. The peaks of the sinusoid (corresponding to pressures greater than ambient) are generated by the crystal expanding. The troughs (corresponding to pressures less than ambient) are generated by contraction of the crystal.

At shallow depths the output power may be limited by cavitation at a level far below that imposed by other factors, such as electrical and mechanical limitations. Cavitation occurs when, by contraction of the crystal, the pressure in the water decreases to a level where the water vaporizes, producing bubbles on the face of the crystal. The presence of a large number of bubbles near the face of the sonar transducer act like a pressure release surface and, therefore, drastically reduces the amplitude of the emitted signal.

The acoustic intensity at cavitation threshold (i.e. when cavitation starts) is primarily a function of depth (Burdic, 1984 and Urick, 1983). The cavitation threshold of a sonar transducer may be raised by: (1) increasing the frequency (Burdic, 1984 and Urick, 1983) (2) increasing the depth of the sonar transducer. The idea is that cavitation nuclei require a finite time interval to grow to a size where their effects are observable. Placing the sonar transducer at a greater depth increases the ambient pressure.

Increasing the amplitude of crystal oscillation beyond the cavitation limit does not increase the amplitude of the sonar pulse in the water. The only way to further increase the power transmitted to the water is to increase the pulse length. This means the number of cycles in the pulse must be increased, which results in a decrease of resolution. This limitation represents a major disadvantage of sonar transducers. Another disadvantage is that the amplitude of the pulse is tapered. It grows from zero to a certain value and after some time it decays back to zero. It is not clear whether the first excursion is positive or negative and consequently the wavelet polarity is ambiguous.

1.2.1.2 *Chirp Sonar Transducer*

A chirp sonar transducer is a variation of the sonar transducer. A chirp sonar transmits a computer generated FM pulse that sweeps over a certain frequency range (200 to 30,000 Hz, depending on the transducer configuration). The energy of the transmitted FM pulse can be varied within the range of 1 to 500 Joules by adjusting the power amplifier level and/or by selecting the pulse length, typically 5 to 200 ms (Schock et al., 1989).

Varying the amplitude and frequency of the emitted pulse in a predetermined pattern is known as "chirping". To obviate the ambiguity in polarity of the reflected signal, the received and emitted signals are correlated.

1.2.1.3 *Sparker*

Sparkers utilize the discharge of a capacitor to create a spark between two electrodes located in the water. The heat generated by the discharge vaporizes the water, creating a steam bubble. The bubble pulse effect (related to steam bubble) is described in paragraph 1.2.2.1. Several sparker units are often used in parallel. Large sparker arrays deliver as much as 200 kJ at 50 to 200 Hz and achieve penetrations of about 600 ms (Telford et al., 1990). Small sparkers operate with

several hundred Joules input energy at about 1000 to 2000 Hz, see Chapter 2.

An alteration of the sparker is needed in fresh water because fresh water has a low conductivity. One alteration involves connecting the electrodes by a thin wire which is vaporized in the discharge (Telford et al. 1990). A second method is to enclose the sparker in a bag of salt water which in turn is placed in the fresh water. When the sparker is fired, the signal is transmitted through the bag to the fresh water.

1.2.1.4 *Boomer*

A boomer consists of two plates that are forced apart suddenly by a heavy surge of electrical current through a coil on one of the plates. This generates eddy currents in the other plate, resulting in repelling it suddenly (Telford et al., 1990). This generates an acoustic wave in the water. The typical input energy for a boomer is several hundred Joules, the frequency ranges from several hundred Hz to about 10 kHz.

1.2.2 *Pneumatic sources*

Pneumatic sources are driven by compressed air. Pneumatic sources can be divided into exploders, like airguns, and imploders, like waterguns. Exploders use the sudden release of compressed air into the water to generate the seismic signal. Imploders create a region of very low pressure in the water. The collapse of water into this region generates the acoustic signal.

1.2.2.1 *Airgun*

The principle of operation of the airgun is an explosive release of a 'charge' of high pressure air in the water. The traditional design has two chambers, a control chamber and a firing chamber. The two chambers are divided by a moving shuttle with a hole in its shaft. Air from the upper chamber enters the lower chamber via this hole. The shuttle is held down by the pressure in the control chamber. At the instant the gun is to be fired, a valve is opened that injects high-pressure air in such a way that the shuttle moves upward at a high velocity (Parkes and Hatton, 1986).

Most airguns have four venting holes. As the shuttle moves upward, passing the venting ports, most of the high pressure air from the lower chamber is

suddenly spilled out into the water which creates an oscillating air bubble (like explosive sources). Initially, the pressure inside the bubble exceeds the ambient pressure, so the air bubble expands rapidly, even beyond the point where the internal pressure and the ambient pressure are equal. When the expansion stops, the internal bubble pressure is below the ambient pressure and the bubble starts to collapse. The collapse overshoots the (pressure) equilibrium and the cycle starts again. The oscillation period increases with increasing volume and pressure of the airgun (Parkes and Hatton, 1986). The oscillation period decreases with increasing source depth. The amplitude ratio of primary pulse to the bubble pulse increases with decreasing source depth (Dobrin and Savit, 1988).

To suppress the bubble oscillations, an array of airguns of different sizes and pressures can be used. The bubble periods of the guns in an array are different and the bubbles will partially cancel each other. The primary pulses will add constructively and the primary to bubble ratio is improved. Using guns with different input energies in the array gives the signal a broader frequency spectrum.

The airguns used in high resolution profiling are similar to those used in conventional marine work except that they are smaller; they can involve as little as 1 in^3 of air at 70 bar.

1.2.2.2 *Sleevegun*

The sleevegun is a variation on the traditional airgun. The principle of operation is the same, only the way in which the air is released is different. Instead of having four venting holes like the airgun, the sleevegun has a sleeve which is moved, allowing a full 360° venting.

1.2.2.3 *GI-airgun*

The GI-gun is another type of airgun, especially designed to suppress the bubble pulses. This is achieved by dividing the lower air-chamber into two parts. One part is opened when the gun fires. The other part is opened some time after the initial discharge, so that air will flow in the bubble at the moment it starts to contract. In this way the amplitude of the bubble pulses is damped.

1.2.2.4 *Watergun*

The watergun is basically an implosive source. In the traditional design of the watergun there are two chambers, an upper air chamber and a lower water chamber which has an open connection with the sea. A moving shuttle divides the chambers. High pressure air is fed into the top chamber. At firing time the shuttle is released, and the high pressure of the air forces the shuttle downwards. The water is thereby violently ejected from the lower chamber. As the shuttle slows down and the water continues to expand, a vacuum cavity is formed between them. The expansion slows, stops, and is followed by an implosion of the water into the cavity.

The collapse of water into the vacuum creates the main implosive pulse followed by a minimum tail. There is no compressed air to store energy for a subsequent expansion; hence there is no succession of bubble pulses. The main implosive pulse is preceded by a lower frequency pre-cursor produced at the water expansion stage. The time between the precursor and the implosion pulse is called the period of the gun. This period is affected by both the operating pressure of the gun and the water pressure at the gun ports (Tree et al.,1986).

1.2.3 *Energy of pneumatic sources*

The input energy of pneumatic sources can be calculated using Boyle's law. For an ideal gas at a constant temperature Boyle's law is:

$$pV = C \text{ hence } p = \frac{C}{V} \qquad [1.1]$$

where p is the pressure of the gas, V the volume of the gas and C is a constant. The energy, E, needed to compress air from volume V_0 to volume V_1 is given by (Alonso and Finn, 1983) :

$$E = \int_{V_0}^{V_1} p \, dV \qquad [1.2]$$

Using Boyle's law this can be rewritten as :

$$E = \int_{V_0}^{V_1} p \, dV = \int_{V_0}^{V_1} \frac{C}{V} \, dV = C \ln \frac{V_1}{V_0} \qquad [1.3]$$

For a 10 in^3 airgun at a pressure of 100 bar the input energy is calculated as follows. The constant C is calculated, then the volume of the uncompressed air, V_0, is calculated using Boyle's law and the pressure at sea level, p_0.

$$C = pV = 100\ bar \cdot 10\ in^3 = 100 \cdot 1.013 \cdot 10^5\ N/m^2 \cdot 1.5625 \cdot 10^{-4}\ m^3 = 1583\ Nm$$

$$p_0 = 1\ bar = 1.013 \cdot 10^5\ N/m^2$$

$$V_1 p_1 = V_0 p_0 = 1583\ Nm$$

$$V_0 = V_1 p_1 / p_0 = 1.5625 \cdot 10^{-2}\ m^3$$

The input energy, E, for a 10 in^3 airgun at a pressure of 100 bar is :

$$E = C \ln (V_1/V_0) = 1583 \ln (0.01) = -7290\ Joule$$

Since it requires energy to compress air, a negative value is obtained.

1.3 *Acquisition Techniques*

The objective of a survey and field circumstances determine which type of source should be used. The objective of the survey is defined in terms of depth penetration and resolution. The depth penetration is not necessarily defined in meters, it can also be defined in terms of reflection time or in geological terms such as 'the top of the pleistocene' or 'the moho' or 'below the sand layers'. The resolution can also be given in geological terms like 'the internal structure', or 'the mud layer on top of the bedrock'. Examples of field circumstances are the water depth, weather conditions, track lines, etc.

Sources with high dominant frequencies and large bandwidths are used to obtain high vertical resolution of the seismic recordings. Processing is also used to improve the vertical resolution (e.g. deconvolution techniques). Vertical resolution can also be improved by towing the sources close to the water surface. In doing so the surface (ghost) reflection will closely follow the source wavelet; hence the "source wavelet" includes the surface ghost reflection. Towing the array of hydrophones close to the surface also shortens the pulse length by shortening the surface (ghost) reflection delay on the receiver side.

Another advantage of towing the airguns close to the surface is that the primary bubble reaches the surface before it has its maximum diameter. This means that the air in the bubble is released into the air before the bubble starts contracting, thus before bubble pulses can be formed.

Improvement of the horizontal resolution can be obtained by decreasing the shot interval. In marine work this has some practical limitations. While recording the data the boat, the source and the streamer, are moving. With a fixed shot rate the distance between shots depends on the ship's speed. To decrease the shot interval the ship should go slower, but at lower speeds it is more difficult to stay on course. Moreover, towing the equipment becomes difficult. A second possibility is to increase the shot rate. This, however, also has some practical limitations. The time interval between shots should be at least the recording time. The next shot should not be fired before the multiple train of the current shot has died out. Besides this, the source must be able to produce the shot rate.

1.4 *Receivers and Source-Receiver Geometry*

In marine seismic profiling the receivers normally consist of piezo-electric elements, called hydrophones. The hydrophones produce an output voltage proportional to the (change in the) pressure field. This electric signal is normally very weak and easily affected by noise. The output voltage is therefore sent through an amplifier before recording the signal. Anti-alias frequency filters are needed before recording when the data are digitally recorded. Changes in pressure field are not only caused by the reflected seismic signal but also by other factors, such as other boats, the propulsion of the ship, the towing of the equipment, weather conditions, waves, etc. Changes in the pressure field due to these other factors are considered to be noise.

The most common way to improve the signal-to-noise (S/N) ratio is to put a number of hydrophones in a group (array) and sum the signals of these individual hydrophones. In the design of an array the (S/N) ratio should be considered. To add constructively, the recorded signals of all the hydrophones in a group must be in phase. This means that the difference in travel distance of the seismic signal between the nearest and the furthest hydrophone in a group must be smaller than a quarter of the wavelength of the signal. Figure 1 shows a common field geometry. If the shallowest depth of interest is close to the water bottom the water depth can be used for the array design. Assume a water depth D, an offset between source and nearest hydrophone in the array X and an array length L. The travel distance to the nearest hydrophone is:

$$r_1 = \sqrt{4D^2 + X^2} \qquad [1.4]$$

and the distance to the furthest hydrophone is:

$$r_2 = \sqrt{4D^2 + [X + L]^2} \qquad [1.5]$$

so the difference in travel distance is:

$$\Delta r = r_2 - r_1 = \sqrt{4D^2 + [X + L]^2} - \sqrt{4D^2 + X^2} \qquad [1.6]$$

The wavelength of the signal is mainly determined by the dominant frequency of the source, but the highest frequency of interest gives the minimum wavelength (λ) which should be used in the array design. The maximum array length is obtained when Δr equals a quarter of the minimum wavelength ($\Delta r = \lambda / 4$). The relation between the maximum array length, water depth, offset and minimum wavelength, with $\Delta r = \lambda / 4$, can be expressed as:

$$L = -X \pm \tfrac{1}{2}\sqrt{4X^2 + \lambda^2/4 + 2\lambda\sqrt{4D^2 + X^2}} \qquad [1.7]$$

Figure 2 shows the relation between maximum array length L and water depth D for six different minimum wavelengths λ_i and for various offsets X. The frequencies (f_i) in water corresponding to the minimum wavelengths (λ_i) are also shown in figure 2. Both shallower water and increasing offset require shorter arrays.

Another geometry is shown in figure 3. Here the source and receiver are parallel and the source is placed in the middle of the array. The travel distances to the nearest and furthest hydrophone in the array now are:

$$r_1 = \sqrt{4D^2 + X^2} \qquad [1.8]$$

$$r_2 = \sqrt{4D^2 + X^2 + L^2/4} \qquad [1.9]$$

The relation between the maximum group length, water depth, offset and minimum wavelength can now be expressed as:

$$L = \sqrt{\lambda^2/4 + 2\lambda\sqrt{4D^2 + X^2}} \qquad [1.10]$$

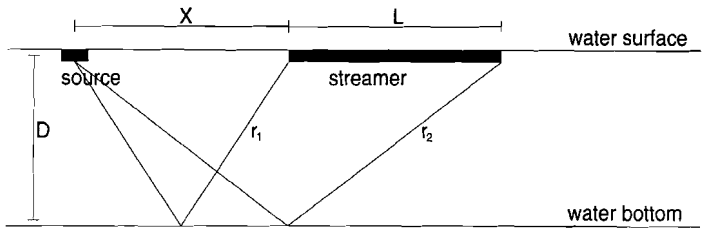

Figure 1. Commonly used Source - Receiver geometry (side view).

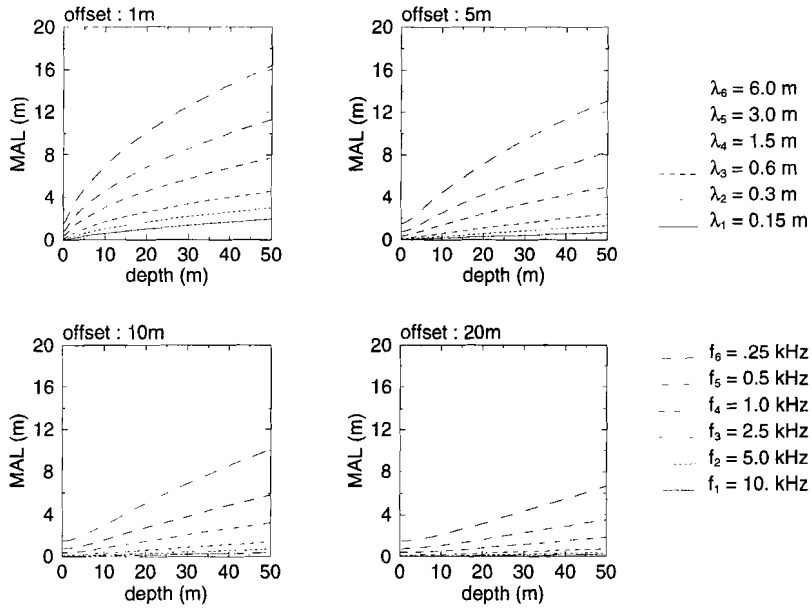

Figure 2. Relations between water depth, source-receiver offset, minimum wavelength (λ_i) or highest frequency of interest (f_i) and the maximum array length (MAL) for source-receiver geometry as shown in figure 1.

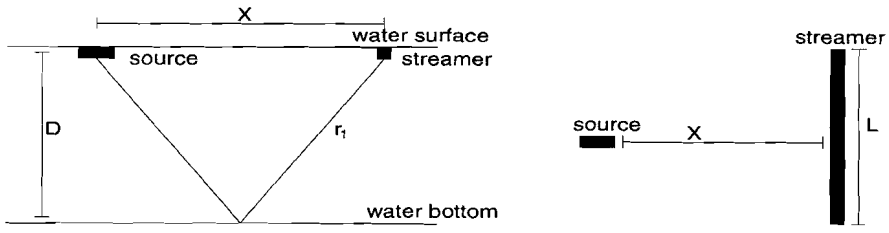

3.a 3.b

Figure 3. Alternative Source - Receiver geometry (a) side view and (b) bird's eye view.

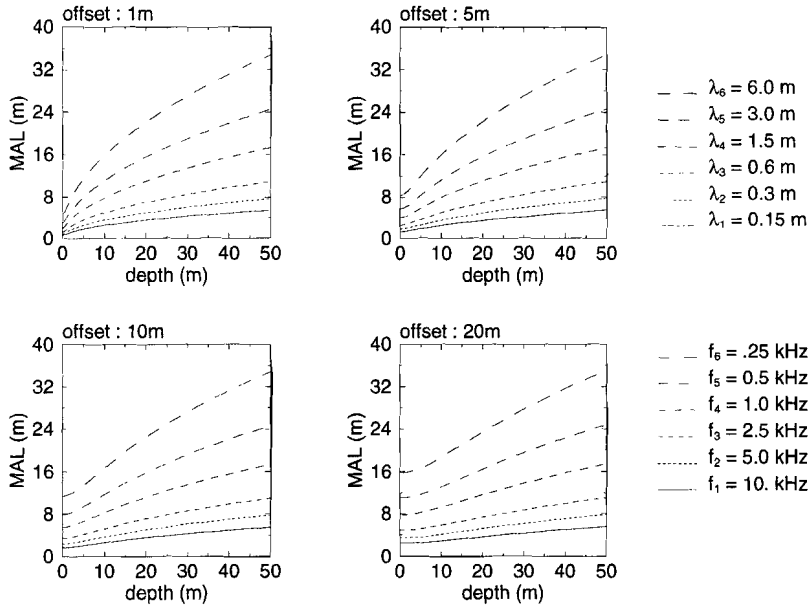

Figure 4. Relations between water depth, source-receiver offset, minimum wavelength (λ_i) or highest frequency of interest (f_i) and the maximum array length (MAL) for source-receiver geometry as shown in figure 1.

Figure 4 shows the relation between maximum array length L and water depth D for six different minimum wavelengths and for various offsets X. The frequencies (f_i) in water corresponding to the minimum wavelengths (λ_i) are also shown in figure 4. Comparison between figure 2 and figure 4 shows that in this second geometry the array can be longer and therefore contain more hydrophones which can improve the signal-to-noise ratio. Figures 2 and 4 show that the maximum array length strongly depends on the water depth. The water depth is often not constant and therefore the maximum array length varies, although the same seismic source is used (with the same minimum wavelength). To maximize the S/N ratio the array length should be adjusted to the water depth during the profiling.

It is not practical to change streamers during a survey, so a special multi-channel streamer was designed. This streamer consists of 30 hydrophones spaced 7 cm apart. The three groups of this streamer comprise 18, 4 and 8 hydrophones. The groups can be recorded separately and later, during the processing, be summed if the water was deep enough. Recording the groups separately gives the possibility to use one group for the 'near surface reflections' and sum the signals of the groups for the deeper part of the section to improve the S/N ratio, without losing resolution. If the water is deep enough the signals of several groups can be summed in the amplifier before recording to save storage space and processing time. The advantage of such a multi-channel streamer is that one streamer is suitable for various water depths.

For good penetration most of the energy should be transmitted through the water bottom and not be reflected. McGee (1991) shows that if the angle of incidence is smaller than 10° from the vertical most energy is transmitted as compressional waves. This means that the source-receiver offset can maximally be 1/5 of the water depth, or that the arrival time of the direct wave is 1/10 of the arrival time of the water bottom reflection. There are some practical limitations on trying to reach near zero offset. The towing mechanism of the source can introduce water turbulence noise and the low frequencies in the near field of the source can saturate the receiver pre-amplifiers. Also the source and receiver can bounce against each other, which will also saturate the receiver pre-amplifiers.

Often multi-channel arrays are used in seismics. The advantage is that speeds of propagation can be estimated from the offset measurements. For single channel data it is not possible to obtain the velocities from the seismic data only.

Another advantage of multi-channel data is that after some corrections the channels can be stacked to a trace with an improved signal to noise ratio (common

mid point trace, CMP trace). Some problems arise here. If the source wavelet is not well-repeatable, the signals that will be stacked are different and the S/N ratio will not be improved. The source-receiver geometry will be different for the traces involved in the stacking procedure. The angle of incidence of the signal is not the same for all the traces. Since some shallow marine seismic sources have a non-spherical response, the received signals can be different on the several traces and stacking can decrease the S/N ratio.

Stacking requires that the CMP points for the different shots must be in a small range, otherwise it is not a CMP point. To know which shots can be used for stacking means that the positions must be known very accurately (within a small part of the wavelength). This is not feasible in high resolution marine seismics. In shallow water there are also practical limitations on the use of a multi channel streamer. For example, long streamers can be difficult to tow in congested areas.

1.5 *Acquisition System*

In shallow marine profiling research vessels are often small. Therefore a small data acquisition system is needed. The system must be able to sample at high sample rates to cover the whole frequency range provided by the high resolution marine seismic sources (see also chapter 2). Because of this high sample rate the storage capacity must be large. Also a multi-channel system is sometimes required. Owen and Sinha (1991) described the design of a PC based acquisition system. This system had a resolution of 12 bytes and had a maximum sample rate of 4 kHz, so it was not very useful for high resolution seismics.

In Utrecht a better marine data acquisition system (MDAS) was designed and developed (Posthumus, 1991). The Utrecht system is based on a 286 PC with a 287 coprocessor. The system has a 16 bit A/D converter and 8 channels can be recorded simultaneously. The dynamic range is 16 bits of which 2 are system noise, giving a dynamic range of 84 dB. The sample frequency ranges from 203 kHz single channel to 50 kHz eight channel. The recording time is limited to 192,000 samples per shot. A delay time between shot trigger and the start of the recording can also be set.

The system is based on a PC with removable hard disks. The removable hard disks are necessary to ensure that data are not lost when one disk is full. In the event that one disk is full, the system switches to the other disk and the first disk can be replaced. Removable hard disks were used because they are small and fast enough to store the data and relatively cheap compared to tape units. The data

can be displayed real time in wiggle trace format on the screen and as a colored section on a color printer. Frequency analysis and clipping checking can also be done with this system. In 1991 the system was improved so that the Global Positioning System can be used and the position can be recorded at each shot.

The future of PC based acquisition systems lies in using faster processors for some simple real-time processing. More memory will be used to increase the number of samples recorded per shot. Larger (in capacity) storage media will be used, like DAT and exabyte tapes. Some commercially available system have some of these options.

All real data presented in this thesis have been recorded with the Utrecht MDAS acquisition system.

1.6 *Positioning*

The source and receivers are important for controlling the vertical resolution. Horizontal resolution is also important and therefore accurate positioning is required. Several positioning techniques exist. The simplest is to mark the record when special objects (such as buoys, bridge pillars, etc) are passed. One can also make time measurements for each shot and keep a log of special objects and the time when they were passed. It is normal practice to keep a log of time and position, even when the position is given by a positioning system. When the time of each shot is known, shot and position can be coupled via the time measurements. Another possibility is to record the position data at each shot and store the position data together with the seismic data.

Positioning systems have greatly improved over the years. The older systems along the North Sea coast, DECCA and SYLEDIS, work with a radio link to coastal stations. These systems measure phase differences between the signals transmitted by the coastal stations and obtain an accuracy of about 50 m. Their range of operation is some hundreds of kilometers.

For local measurements it is possible to set up laser or radio link systems. In these systems the time to several points and phase differences are measured. From these measurements the position is calculated. Laser and radio link systems can give resolutions in the order of decimeters (Henriët et al., 1992).

Newer systems are satellite positioning systems of which the Global Positioning System (GPS) is the best known. A GPS station uses travel times and phase differences to several GPS satellites to compute its location. Depending on the number and positions of the satellites an accuracy better than 20 m is possible.

In the differential GPS (DGPS) method an extra, fixed, base station is used. This can improve the accuracy to a couple of meters. The relative positioning can be better than one meter.

The advantage of laser systems is their very high accuracy. The disadvantage is the relatively difficult and expensive setup of such a system. GPS can be received all over the world, but the accuracy is lower than that of laser systems.

On the research vessel of Utrecht University we started with marking special objects on the recordings (see Chapter 7) because no positioning system was available. On other ships (see Chapter 6) we started with keeping log of the time-position measurements. Later our group obtained a DGPS system and the time and position were recorded for each shot. The position data of each shot were stored together with the seismic data.

1.7 *Noise*

Special attention should be paid to controlling and suppressing noise during the seismic recording. The S/N ratio can be improved by increasing the amplitude of the emitted signal or suppressing the noise or both. In general the amplitude of the signal is increased by increasing the input energy of the seismic source. Increasing the signal is a limited option, since in general an increase of the input energy of a source leads to a decrease of the resolution. The sources also have a limited maximum output. Therefore, noise suppression is always necessary.

The noise can be divided into three parts; electrical noise, operational noise, and 'noise' related to the source-receiver geometry. This last 'noise' is not really noise but a decrease in S/N ratio because of using an non-optimal source-receiver geometry (see section 1.3). In shallow water it is very important to keep the noise at a low level. In general, the S/N ratio cannot be improved by stacking of signals without losing resolution (see section 1.4).

Electrical noise is often caused by poor grounding of the system. The Utrecht research vessel had four electrical circuits: one for the acquisition PC, one for all controlling equipment (filters, amplifiers, trigger pulses, etc), one for the 12V equipment (like the GPS equipment) and a separate 220V 4000W generator for use with electrical sources like boomers and sparkers. The noise generated by interference between power and measurement cable can be reduced by isolating the cables from each other.

Operational noise is mostly ship noise and wave and water motion. The ship noise can be reduced by surveying at speeds such that the ship produces the least noise, or noise outside the bandwidth of the signal. The propulsion of the ship is also a source of water noise. The Utrecht research vessel also had electrical outboard propulsion, which is more quiet than a conventional outboard motor. Towing the receivers far from the propulsion helps to reduce this noise. The source should also be towed away from the motor to keep the correct source-receiver geometry. A long towing distance can give problems in congested areas. A small source-receiver offset can also be a source of noise (see section 1.4). The streamer should be stretched all the time so that the hydrophone spacing in the array remains constant during the recording. Varying hydrophone spacing can decrease the resolution. Also the depth of the streamer should be constant, otherwise the surface (ghost) reflection will arrive at different times at the hydrophones.

Since the source and receiver are kept close to the surface, weather conditions and sea state can be a source of noise. It is very important to choose a quiet period for the profiling whenever possible.

1.8 *Summary*

In high resolution marine seismic profiling it is common practice to operate the seismic sources and receivers close to the water surface. This is done to shorten the "ghost" reflection time. For airgun type sources this also reduces the strength of the bubble pulse. Towing the source and streamer in parallel has the advantage that longer streamers can be used. A small acquisition system that can record many samples at high sampling frequencies is desired. For accurate (local) positioning laser or radio link systems can be used. For larger areas DGPS seems more appropriate. The S/N ratio can be improved by suppressing noise during the data acquisition. This can be done by a good electrical grounding of the acquisition system and by sailing at speeds that generate little noise.

Chapter 2

Characteristics of High Resolution Marine Seismic Profiling Sources[1]

2.1 *Introduction*

A detailed knowledge of source characteristics is necessary for a successful implementation of some processing algorithms. This is especially true for processes involving inversion or parameter estimation.

Statistical methods are often used to estimate source wavelets from measured data. These methods rely on assumptions such as stationarity and minimum phase. It is often doubtful whether the resulting estimates are accurate representations of actual source wavelets (Ziolkowski, 1991). In theory, a detailed deterministic knowledge of actual wavelets would be better than statistical estimates. As a first step toward accumulating deterministic knowledge, a practical workshop for the recording of mid-water signatures from three high-resolution marine sources was conducted in the U.K. (McGee et al, 1992). Signatures from four other types of sources were recorded in the Netherlands during 1992 and 1993.

In this chapter some properties of these high resolution marine seismic sources, i.e. wavelet shape, frequency content, repeatability and directivity are discussed. Sometimes it is difficult to determine the bandwidth of a source from its spectrum. A method is proposed to calculate the bandwidth from the 'time signal' of the source wavelet.

---

1 Parts of this chapter have been accepted for publication as: Verbeek N.H and McGee T.M., Characteristics of high resolution marine profiling sources, Journal of Applied Geophysics, 1995.

type of source	operational parameters	input energy	deployment depth
conventional sonar transducer	3 cycles of 3.5, 5, 7, 10, 14 kHz	0.3, 0.4, 0.6, 0.8, 1.2 J	15 cm
Datasonics TTV-160 chirp sonar	1-10 kHz sweep over 5, 10, 20 ms	10, 20, 40 J	15 cm
O.R.E. "Geopulse" 5810B boomer	105, 175, 280, 350 J	105,175, 280, 350 J	5 cm
custom multitip sparker	100, 200, 300 J	100, 200, 300 J	20 cm
Sodera S15 watergun	15 in^3, 80 & 120 bar	8700 & 14300 J	30 & 60 cm
Bolt 600B airgun	10 in^3, 80 & 120 bar	5800 & 9500 J	25 cm
Texas Instruments SGI sleevegun	6 in^3 at 80 & 120 bar 10 & 25 in^3 at 100 bar	3500 & 5700 J 7600, 19000 & 27000 J	30 & 130 cm 200 cm

Table I. Measured source types, operational parameters, input energy and deployment depth.

2.2 *Data Acquisition*

The signatures recorded in the U.K. came from a chirped sonar transducer, a boomer and two sleeveguns. The sources measured in The Netherlands included a conventional sonar transducer, a multi-tip sparker, an airgun, a watergun and a sleevegun. The source types tested, the input energy levels and the operational parameters are tabulated in table I. The recording was done in deep water to avoid interference between the signature and the reflection from the water bottom. In the U.K. the measurements were carried out on Lake Windermere, which is about 70 m deep. In The Netherlands the measurements took place in a 20 m deep sand pit, along the river Rhine and in another sand pit near Haarlem.

The source signatures were recorded while the survey vessel was stationary with the engine turned off to reduce noise. Figure 1 shows the field geometry of the recordings. The source was at about 20 meters horizontal offset from the ship and was kept in place by a tether. Along this tether the hydrophone was placed at the desired offset from the source and lowered to the desired depth. It was not possible to use the tether for the watergun measurements. Therefore, the watergun

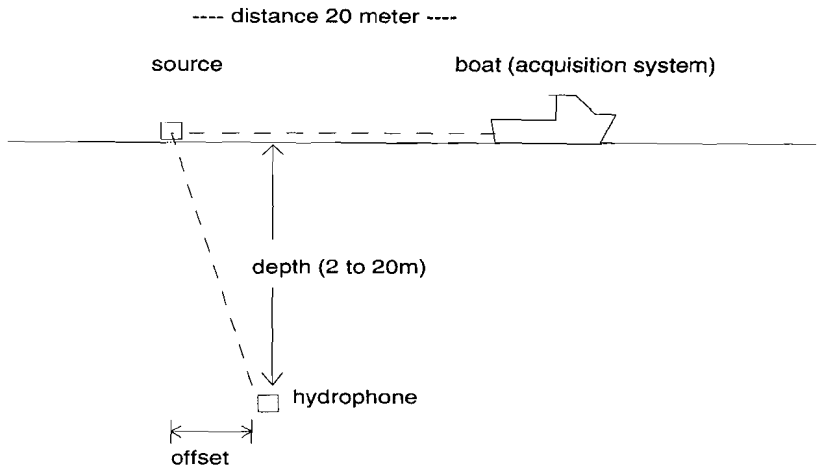

Figure 1. Schematic plot of the field geometry during the recording of the signatures. The angle between the source and the hydrophone ranged from 0° to 45°.

was placed about 2 meters from the boat with a crane.

It is common practice in high-resolution profiling to deploy the source at a very shallow depth in order to minimize the surface "ghost" reflection time. This also reduces the strength of "bubble" pulses associated with the airgun and sleevegun (see section 1.4). On Lake Windermere, the boomer and chirp sonar were deployed close to the surface. The sleeveguns were deployed at depths great enough to separate the surface "ghost" reflection from the direct arrival. In The Netherlands, all sources were deployed as close to the surface as possible. In addition, the watergun and the sleevegun were operated at greater depths also.

All signals were received by a single Bruel & Kjaer Type 8104 hydrophone which is specified by the manufacturer to be essentially omnidirectional with a flat (± 2 dB) frequency response to 80 kHz. It was suspended below the source at depths varying from 2 to 20 meters. In order to observe source directionality, the horizontal offset between source and hydrophone was varied from zero to distances equal to the depth of the hydrophone. The source was fired several times at each hydrophone position in order to check repeatability. In total, more than 5000 shots were recorded.

Each signature was passed through an analogue band-pass filter. The low-cut of this filter was 50 Hz and the high-cut of the filter was 50 kHz, both with a 12 dB/octave slope. The conventional sonar was filtered from 2.5 kHz to 29 kHz, due to a misunderstanding in the field. All signatures were recorded digitally with a PC-based data acquisition system (MDAS, see section 1.5). The signals were sampled as quickly as the equipment allowed; 203,846 kHz.

2.3 *Source Signatures and Spectral Characteristics*

In this section the source signals will be discussed in terms of time and spectral characteristics. An example field recording for each source type is shown in figures 2 to 8. Each plotted signature was recorded at near zero horizontal offset. The noise in the recordings is determined on the basis of the signal measured before the source wavelets arrived. Since some of the recorded traces include several types of seismic signals, a certain amount of data editing was required to isolate the signals comprising the source signatures. The wavelets representing the first onset of the recorded signal as well as any "ghost" or "bubble" associated with normal source deployment were considered to comprise the source signatures. The portion of the recording considered to be the signature of each source type is indicated in figures 2 to 8 by a dashed box. Signals not considered to be intrinsic to the signature are excluded from the box.

Each spectrum was characterized by three parameters; the frequency at which peak power occurs, the bandwidth at 40 dB below peak power and the bandwidth at 6 dB above the noise level (+6 dB NBW). These parameters are tabulated in table II (page 36) of every source type studied. The tabulated values are averages of measurements taken from ten individual signature recordings.

2.3.1 Sonar Transducer

Figure 2.a shows the recording of the 10 kHz conventional sonar transducer signature. The first arriving signal was taken to represent the source wavelet. It consists of about 4 cycles of a sine wave, tapered on both ends. The power spectrum of this wavelet is represented by the solid line in figure 2.b. The dominant frequency is 11 kHz and the -40 dB bandwidth is 25 kHz (3 to 28 kHz). The power spectrum of the noise is shown as a dashed line. The noise level is about 65 dB below peak power and the +6 dB NBW is 33 kHz.

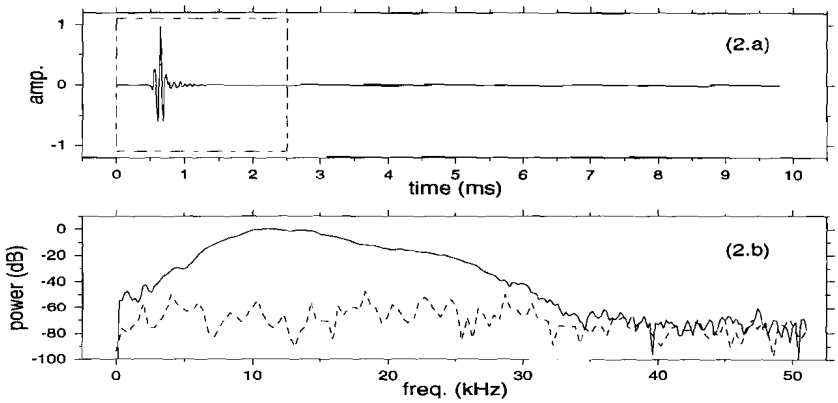

Figure 2. Example of a 10 kHz conventional sonar transducer signature and power spectrum. The source depth is 15 cm and the hydrophone location is 10 m deep at 1 m offset.

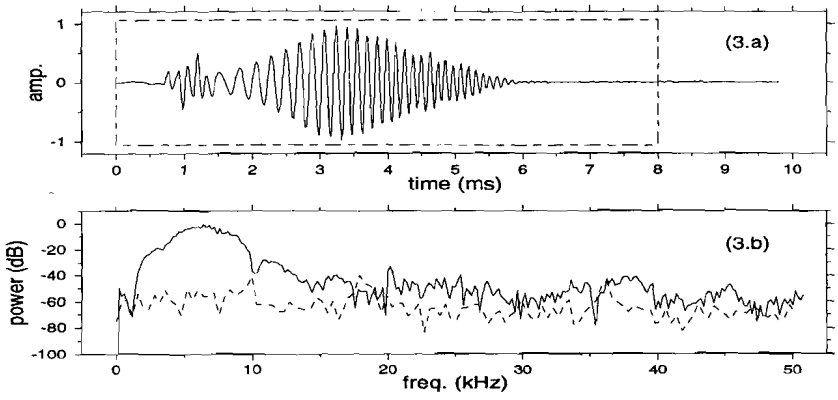

Figure 3. Example of a 5 ms sweep chirp sonar signature and power spectrum. The source depth is 15 cm and the hydrophone location is 10 m deep at zero offset.

All signatures of the conventional sonar consist of several cycles of a sine wave. Dominant frequencies of the sonar transducer signatures were found to be very similar to the nominal frequency setting. The bandwidth decreased with increasing pulse length.

2.3.2 Chirp Sonar Transducer

The source signature of the 5 ms sweep chirp sonar is shown in figure 3.a, its power spectrum in figure 3.b (solid line). The frequency was swept from 1 to 10 kHz with a taper on both ends. The main sweep (1.4 to 6 ms) is preceded by a short signal (0.6 to 1.4 ms). The dominant frequency of the 5 ms chirp sonar was 6.5 kHz. The measured noise level was about 60 dB below peak power. The -40 dB bandwidth is 8.5 kHz (1.5 to 10 kHz) and the +6 dB NBW is about 17 kHz.

The small 'precursor' before the main sweep is recorded for all chirp sonar signatures and is due to the construction of the chirp sonar. Neither the dominant frequency nor the bandwidth of the chirp sonar changed with pulse length. The sweep of the chirp sonar is normally 'collapsed' into a short signal by correlating the received and the emitted signal.

2.3.3 Boomer

The boomer signature is plotted in figure 4.a. It has a clear onset and a short duration. The power spectrum (figure 4.b, solid line) is smooth. The dominant frequency is 8 kHz and the -40 dB bandwidth is 40 kHz. The noise level is about 60 dB below peak power. The +6 dB NBW is determined by the anti-alias filter used during the measurements and not by the intrinsic features of the boomer. The measurement of the +6 dB NBW is 58 kHz. For the boomer, dominant frequency decreased and bandwidths increased as the energy level increased.

2.3.4 Sparker

The sparker coda includes a signal 1.9 ms after the signature onset. This is apparently an intrinsic feature of the signature because it occurs consistently in all sparker recordings. The time between the main signal and the second signal increases with increasing input energy. This indicates that this second pulse might be a bubble pulse of the sparker (see section 1.2.1.3). The surface ghost appears in the record as the second trough in the first "wavelet".

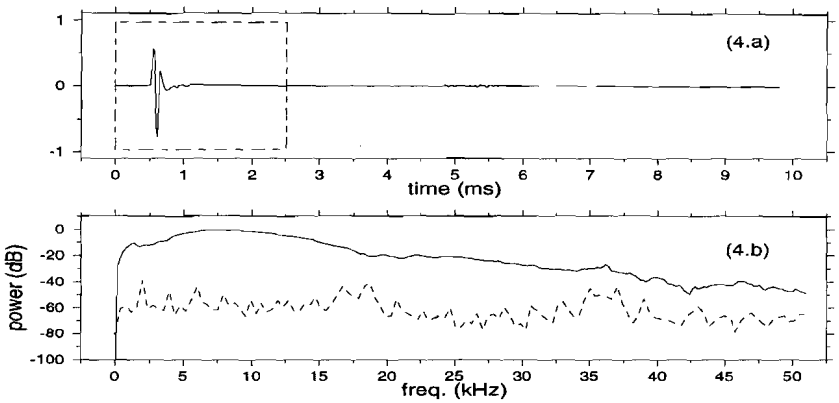

Figure 4. Example of a 175 J boomer signature and power spectrum. The source is at 5 cm depth and the hydrophone location is 10 m deep at 20 cm offset.

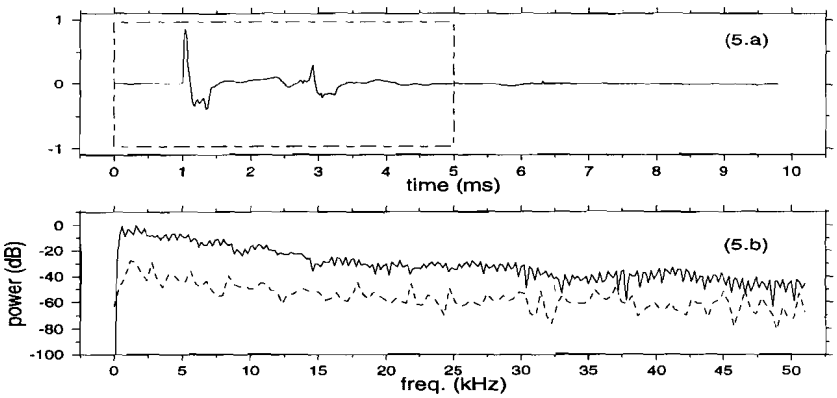

Figure 5. Example of a 300 J sparker signature and power spectrum. The source depth is 20 cm and the hydrophone location is 10 m deep at zero offset.

The power spectrum of the sparker is not smooth (figure 5.b, solid line). The dominant frequency of the sparker is 1.6 kHz. The -40 dB level is not clear due to the rough power spectrum. The noise level varies between 40 and 60 dB below peak power, therefore the +6 dB NBW is difficult to determine.

Both dominant frequency and bandwidth increase as the energy level of the sparker increases. This is probably due to there being an optimal energy level for this sparker and that 300 J is closer to this optimum than the lower energy levels.

2.3.5 Airgun

The airgun signature (figure 6.a) shows a small precursor, probably due to the movement of the shuttle of the gun. The dominant frequency of this signature is 0.5 kHz and the -40 dB bandwidth is 3.3 kHz. The noise level was about -60 dB and the +6 dB NBW is about 51 kHz, except for two points around 18 kHz and 36 kHz. Increasing the pressure of the 10 in^3 airgun did not change the dominant frequency but did increase the -40 dB bandwidth. The +6 dB NBW hardly changed when the pressure was increased.

2.3.6 Sleevegun

The signature of the 6 in^3 sleevegun is shown in figure 7.a. The sleevegun also shows a small precursor, here probably due to the movement of the sleeve of the gun. The noise level varies between 40 and 60 dB below peak power, therefore the +6 dB NBW is difficult to determine. The dominant frequency is equal to the dominant frequency of the airgun, 0.5 kHz. The -40 dB bandwidth is slightly higher than the -40 dB bandwidth of the airgun, 4.0 kHz. The dominant frequency and -40 dB bandwidth of the 6 in^3 sleevegun increased with increasing pressure and decreased with increasing depth. Neither increasing the chamber size nor clustering changed the spectral characteristics of the larger sleeveguns.

2.3.7 Watergun

A weak precursor was recorded about 13 ms before the main signal of the watergun. The amplitude of this precursor is about 1% of the amplitude of the signal shown in figure 8.a. This small precursor is not included in the analysis of the watergun signature.

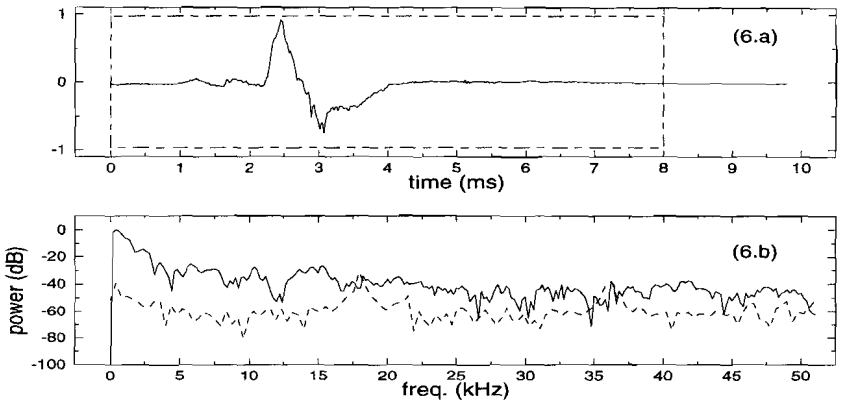

Figure 6. Example of a 10 in^3 airgun signature and power spectrum. The source depth is 25 cm and the hydrophone location is 10 m deep at zero offset.

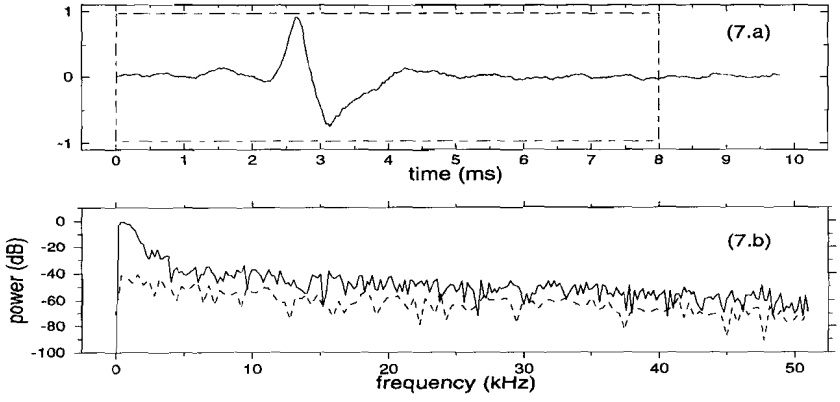

Figure 7. Example of a 6 in^3 sleevegun signature and power spectrum. The source depth is 30 cm and the hydrophone location is 8 m deep at zero offset.

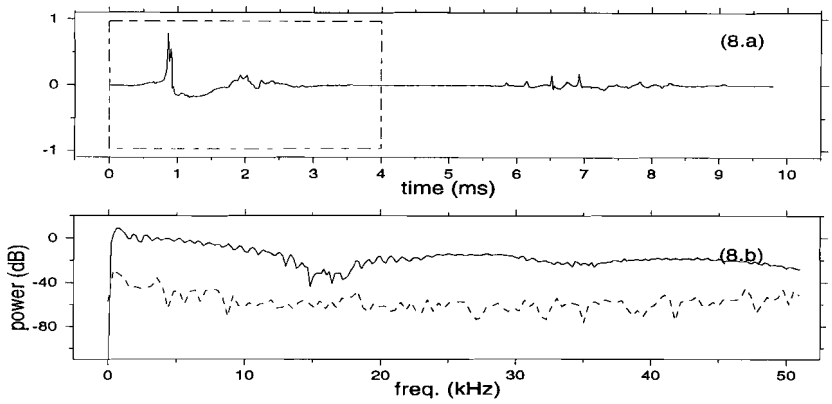

Figure 8. Example of a 15 in^3 watergun signature and power spectrum. The source depth is 30 cm and the hydrophone location is 10 m deep at zero offset.

The multi-peak shape of the watergun signal (at 0.9 ms) can be related to the complex interaction between the cavities created at the several venting ports of the gun. The small signals located about 6 ms after the onset of the watergun signature are extraneous reflections from within the test environment, possibly reflections from the hull of the boat.
The power spectrum of the watergun is shown in figure 8.b. The dominant frequency of the watergun is 0.7 kHz. The dominant frequency and bandwidth of the 15 in^3 watergun were unchanged as the pressure and depth increased within the depth and pressure range tested. The noise level is about -60 dB. The values of the -40 dB bandwidth around 53 kHz and the +6 dB NBW of about 56 kHz seemed to be determined more by the anti-alias filter than by intrinsic characteristics.

In general the electrically driven sources have higher dominant frequencies and broader bandwidths than pneumatically driven sources. Ghost reflections are most apparent in the sparker recordings. They are not as strong in the shallowly deployed pneumatic sources because the water surface was strongly disturbed and scattered the surface reflection. The conventional sonar transducer, the chirp sonar and the boomer do not generate ghost reflections because they are constructed in such a way that the emitted signals are directed downward.

2.4 *Calculated Bandwidth*

The bandwidths for the sleevegun and the sparker are difficult to determine from the +6 dB noise level in the power spectra, because the power spectra are rather rough. The bandwidths for the boomer and the watergun seemed to be partly determined by the anti-alias filter, which was set at 50 kHz. The 'true' bandwidths are even higher. The bandwidth can also be defined as the frequency at which the power spectrum becomes rough. This frequency is difficult to determine for the sparker, watergun and airgun. In these situations a method that gives the bandwidth based on the time signal can be used. One method to do this makes use of the duration, ΔT, of the signal. The minimum bandwidth is then found via the 'duration-bandwidth' product (Claerbout, 1992, McGee, 1994):

$$\Delta T \, \Delta F \geq 1 \text{ or } \Delta F \geq \frac{1}{\Delta T} \qquad [2.1]$$

where ΔF is the bandwidth. The duration of the signal can be defined with the second order moment (Berkhout, 1984, Claerbout, 1992):

$$(\Delta T)^2 = \frac{\int_0^\infty t^2 \, b(t)^2 \, dt}{\int_0^\infty b(t)^2 \, dt} \qquad [2.2]$$

Another definition of duration uses the first negative moment (Claerbout,1992):

$$\frac{1}{\Delta T} = \frac{\int_0^\infty \frac{1}{t} \, b(t)^2 \, dt}{\int_0^\infty b(t)^2 \, dt} \qquad [2.3]$$

Suppose the continuous-time response $b(t)$ decays to below a certain level after time duration $N\Delta t$. If the onset of $b(t)$ is taken to be digital time zero, $b(t)$ can be represented in discrete time as the sequence $\{b_n: b_0, b_1, \ldots, b_N\}$ and the discrete equivalent of equation [2.3] is of the form:

$$\Delta F \geq \frac{1}{\Delta T} = \frac{1}{\Delta \tau} \frac{\sum_{n=0}^{N} \frac{1}{n} b_n^2}{\sum_{n=0}^{N} b_n^2} \qquad [2.4]$$

The duration ΔT becomes shorter as the energy of the response function becomes more concentrated near the origin. Berkhout (1984) and Claerbout (1992) show that the minimum durations are obtained for the minimum phase equivalents of the (causal) signals. The bandwidths found via this method (using the first negative moment) are tabulated in table II and table III (page 36 and 37). How 'good' the calculated bandwidths (CBW) are can be checked by comparing these bandwidths with the -40 dB and the +6 dB NBW. The bandwidths based on equation [2.2] are too low to give an accurate description of the source wavelets.

For the sonar transducer the CBW lies around the -40 dB bandwidth. For the 3.5 and 5 kHz pulses the CBW is higher and for the 10 kHz pulse the CBW is lower than the -40 dB bandwidth. For the 7 and 14 kHz pulses the CBW is close to the -40 dB bandwidth. The CBW for the chirp sonar decreases when the pulse length increases. The CBW falls between the -40 dB bandwidth and the +6 dB NBW. The CBW for the boomer is less than half the +6 dB NBW and about 70 percent of the -40 dB bandwidth. For the sparker the CBW is about 70 to 80 percent of the -40 dB bandwidth. The CBW increases as the input energy is increased. For the watergun the CBW increases with source depth and increasing pressure. The CBW of the airgun also increases with increasing pressure and falls between the -40 dB bandwidth and the +6 dB NBW. The -40 dB bandwidth of the small sleevegun is close to the CBW. For the larger sleeveguns the CBW is higher than the -40 dB bandwidth.

In general the CBW does not indicate very high or low bandwidths. The CBW can be an alternative when methods based on the power spectrum (e.g. -40 dB and +6 dB NBW) fail to give useful bandwidths.

2.5 *Repeatability*

The repeatability of a seismic source is important. If a source has high repeatability, its signature can be measured once and used for further signal processing. Some processing techniques such as the stacking of different shots depend on the source repeatability. Also the quality of plotted profiles depends on repeatability. A brief study of repeatability has been made by comparing "equivalent" pulses, i.e. signatures from different shots for which all the recording parameters are identical. A repeatability index *RI* between two equivalent pulses $s_1(t)$ and $s_2(t)$ can be defined by:

$$RI = 100 \cdot \min(\, s(\tau)\,) \qquad [2.5]$$

where

$$s(\tau) = \frac{\sum_{n=0}^{N-1} |s_1(n) - s_2(n-\tau)|}{\frac{1}{2}\,(\max|s_1(n)| + \max|s_2(n)|) \cdot N} \qquad [2.6]$$

The time shift τ compensates for minor differences in depth of the source or receiver. The absolute differences for every sample are summed over a certain time interval and then divided by the number of samples in that time interval. The result is also divided by the average of the maxima of $s_1(t)$ and $s_2(t)$ to normalize the indices. When $s_1(t)$ and $s_2(t)$ are almost the same, the *RI* will be close to zero and the repeatability is considered to be good. Lower repeatabilities are indicated by larger *RI* values. This index is preferred over the conventional measure provided by the normalized cross-correlation because it has a more direct relationship with the amplitude of the signal. As defined here, the repeatability index can be seen as a percentage of the peak amplitude that changes between the compared signals. A representative value of *RI* for each source type is given in table II (page 36).

Noise in a signature measurement can contribute to the *RI* value. The values in table II are corrected for the contribution of noise by subtracting the noise *RI* from the *RI* values calculated for the signatures. The *RI* for the noise was calculated by doing the summation in the nominator of equation [2.6] over a time interval prior to the onset of the source signature. The denominator in equation [2.6] is unchanged.

The *RI* values of the conventional sonar and the boomer are similar and the best of all sources investigated. The *RI* values for the chirp sonar are about twice as large, except for the 20 ms sweep. The sparker produced *RI* values 7 to 10 times poorer, depending on the energy level. Its values improved with increasing energy level, probably because the energy level approached the optimal energy per electrode. The *RI* values for the watergun, airgun and sleevegun were comparable and about 5 to 6 times poorer than the boomer. The low repeatability of the 6 in^3 sleevegun is probably due to the fact that the water surface was somewhat rough during the measurements.

2.6 *Directivity*

The directivity of each source type was determined from measurements of dominant frequency and bandwidth at various locations in the far-field. The horizontal offset between source and hydrophone was varied from zero to a distance large enough for the signatures to be recorded between angular offsets of 0° (vertically below the source) to 45° from the vertical. At each hydrophone position a number of shots was recorded. Dominant frequency, -40 dB bandwidth and +6 dB NBW were measured from the power spectrum of each signature and an average determined over the number of shots. The results of the directivity measurements are tabulated in tables II and III.

In figure 9 two spectral characteristics are plotted versus the offset angle for each source type shown in figures 2 to 8. The energy levels are the same as in plots 2 to 8. The dominant frequency is plotted on the left-hand side and the -40 dB bandwidth on the right-hand side. Figure 10 shows the comparison between the zero-offset signatures (solid line) and the signatures measured at approximately 30° (dashed line) in the time domain.

The chirp sonar exhibits no directivity in the frequency or the time domain and the conventional sonar shows some directivity. The boomer shows the strongest directivity. Its dominant frequency and bandwidth generally decrease as the offset angle increases. Thus the boomer cannot be considered to be a point source with a spherical radiation pattern (Verbeek, 1992). This is to be expected because the nominal dimension of the boomer plate (50 cm) is not small compared to the wavelength of the peak frequency of the boomer signature (15 cm).

The sparker shows strong directivity in bandwidth. This can be explained by the dimensions of the sparker (a line source of two meters length). The surface ghost in the non zero offset measurements arrives at a different time than in the zero offset measurement and is much more prominent.

The watergun exhibits almost no directivity in either dominant frequency or bandwidth. In the time domain we see some minor changes, especially in the position and shape of the multi peak. These changes are of the same order of magnitude as the changes from shot to shot. It is not clear whether these changes are due to directivity or to a poor repeatability.

The airgun is essentially non-directional. The sleevegun shows some changes in the time domain and the spectral bandwidth. The dominant frequency of the sleevegun remains constant with varying offset angle.

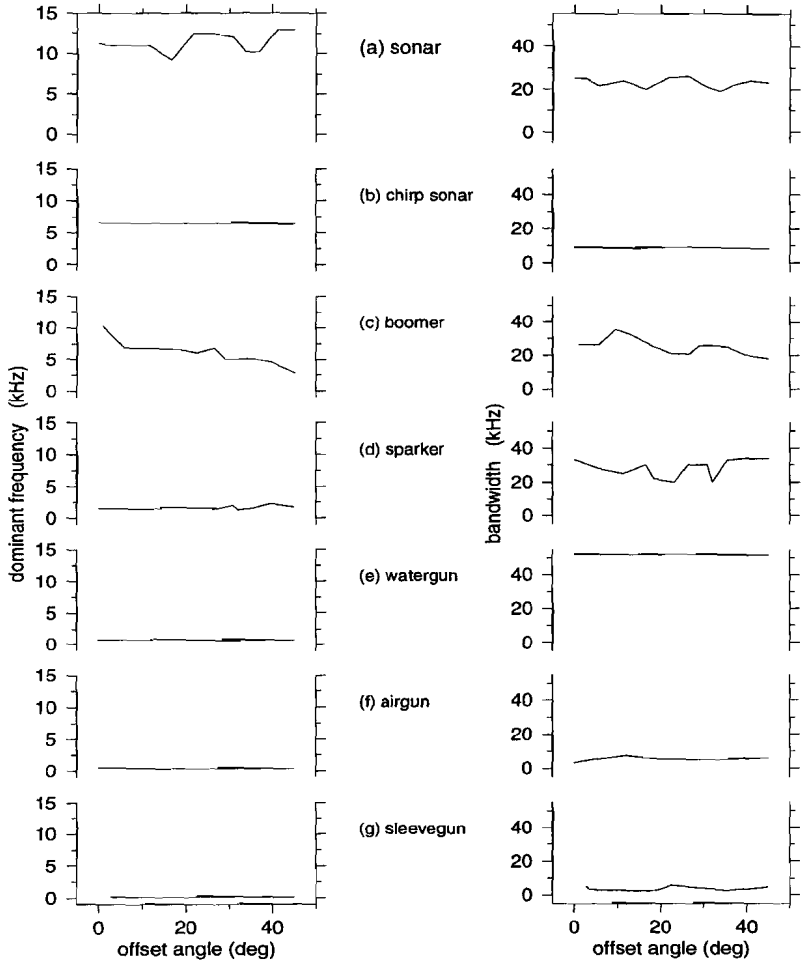

Figure 9. Directivity plots for the seven source types shown in figures 2 to 8. In each case the plot on the left is dominant frequency versus direction of propagation and the one on the right is -40 dB bandwidth versus direction of propagation. (a) 10 kHz conventional sonar transducer, (b) 5 ms sweep chirp sonar, (c) 175 J boomer, (d) 300 J sparker, (e) 15 in^3 watergun, (f) 10 in^3 airgun and (g) 6 in^3 sleevegun. The depth and 'energy levels' of the sources are the same as in figures 2 to 8.

2.7 *Conclusions*

The signatures of seven types of high-resolution marine seismic sources have been investigated. Measurements were made of dominant frequency, spectral bandwidth 40 dB below the dominant frequency and the bandwidth 6 dB above the noise level. In addition, the repeatability and the directivity of the sources were determined.

Apart from the high frequency conventional sonar, the boomer has the highest dominant frequency. The dominant frequencies of the electric-discharge sources are about an order of magnitude higher than those of the pneumatic sources. In most cases the dominant frequency and bandwidth decrease with increasing energy levels. The reverse is true for the sparker. The watergun and boomer have the broadest bandwidth. There is no simple relationship between dominant frequency and bandwidth that holds for all sources.

In some situations it can be difficult to determine the bandwidth of a source from its power spectrum. Therefore, a method based on the duration of a signal is introduced to calculate the minimum bandwidth. This method gives reasonable bandwidths.

The conventional sonar and the boomer are the most repeatable sources, followed by the chirp sonar. The other sources are 5 to 10 times less repeatable. The sparker and the sleevegun were the least repeatable sources. The repeatability of the sparker was observed to increase with increasing energy level. For the other sources, no clear relationship between repeatability and energy level was apparent.

The chirp, watergun, sleevegun and the airgun have weak directivity effects. The boomer exhibited the strongest directivity.

For high resolution marine seismic profiling the boomer looks most suitable. The boomer combines a high dominant frequency with a broad spectrum and a high repeatability. A disadvantage of the boomer is its directivity. In rough sea the 'direction' of the boomer changes constantly, changing the boomer into a source with low repeatability.

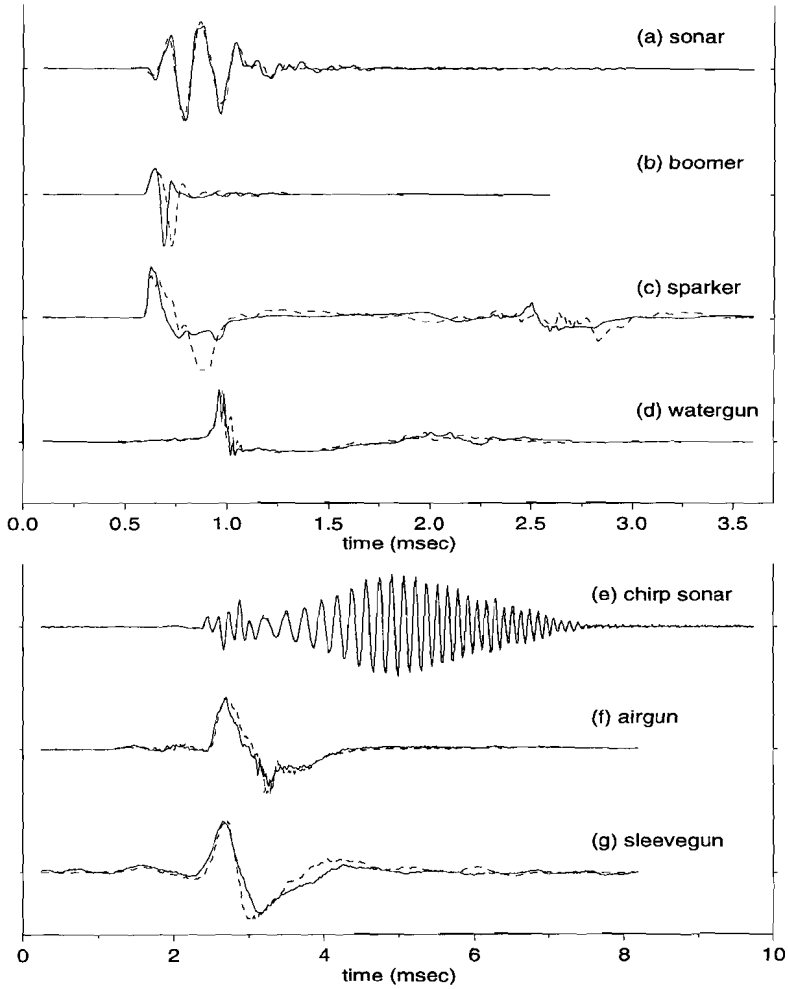

Figure 10. Comparison between signatures measured at 0^o (solid line) and at approximately 30^o (dashed line). (a) 10 kHz conventional sonar transducer, (b) 175 J boomer, (c) 300 J sparker, (d) 15 in^3 watergun, (e) 5 ms sweep chirp sonar, (f) 10 in^3 airgun and (g) 6 in^3 sleevegun. The depth and 'energy level' of the sources is the same as in all other figures.

source type	source depth (cm)	dominant freq. (kHz)	-40 dB bndwth (kHz)	+6 dB NBW bndwth (kHz)	CBW bndwth (kHz)	repeat-ability index	directivity
sonar transducer							
14 kHz	15	13.9	18.8	37.2	18.2	0.22	
10 kHz	15	11.2	25.3	40.4	17.9	0.28	
7 kHz	15	5.7	11.1	37.4	11.9	0.23	medium
5 kHz	15	4.7	7.2	35.2	10.5	0.22	
3.5 kHz	15	4.0	6.4	33.8	7.9	0.26	
chirp sonar							
5 ms	15	6.5	8.5	20.2	17.0	0.45	
10 ms	15	6.5	8.5	17.0	10.0	0.65	weak
20 ms	15	6.5	8.5	17.0	9.4	3.09	
boomer							
105 J	5	10.0	34.5	55.2	27.0	0.21	
175 J	5	8.0	40.0	58.8	24.0	0.23	strong
280 J	5	6.5	45.7	61.0	26.5	0.29	
350 J	5	5.7	41.4	58.0	27.6	0.27	
sparker							
100 J	20	0.9	7.4	??	5.4	2.25	
200 J	20	0.8	11.0	??	7.8	1.91	strong/medium
300 J	20	1.6	30.0	??	18.0	1.46	
watergun							
15 in^3 80 bar	60	0.7	53.2	56.6	28.6	2.02	
15 in^3 120 bar	60	0.7	52.8	55.7	31.9	1.01	
15 in^3 80 bar	30	0.7	53.0	55.3	24.5	1.04	weak
15 in^3 120 bar	30	0.7	53.2	56.3	28.1	1.06	
airgun							
10 in^3 80 bar	25	0.5	3.3	18.1	5.5	1.01	weak
10 in^3 120 bar	25	0.5	4.4	17.8	5.9	1.02	
sleevegun							
6 in^3 80 bar	30	0.5	4.0	??	3.7	1.36	
6 in^3 80 bar	130	0.3	2.6	??	2.4	1.84	
6 in^3 120 bar	30	0.8	5.5	??	4.7	1.66	
6 in^3 120 bar	130	0.3	3.0	??	2.3	1.75	weak
10 in^3 100 bar	200	0.2	3.2	??	4.8	0.89	
25 in^3 100 bar	200	0.2	3.1	??	5.4	1.16	
10+25 1430	200	0.2	3.1	??	5.2	1.32	

Table II. Overview of measured dominant frequency, -40 dB bandwidth, +6 dB NBW, calculated bandwidth (CBW), repeatability index (*RI*) and directivity for zero offset source signatures. A low *RI* means a good repeatable source.

source type	source depth (cm)	offset angle (deg)	dominant freq. (kHz)	-40 dB bndwth (kHz)	+6 dB bndwth (kHz)	CBW bndwth (kHz)
transducer						
14 kHz	15	26.5	13.5	23.4	33.0	12.4
10 kHz	15	26.5	12.6	28.3	34.2	16.9
7 kHz	15	26.5	5.5	12.3	34.2	10.1
5 kHz	15	26.5	4.4	15.0	32.0	9.0
3.5 kHz	15	26.5	4.1	6.7	28.6	6.8
chirp						
5 ms	15	26.5	6.5	8.5	16.0	10.2
10 ms	15	26.5	6.1	8.5	12.0	9.2
20 ms	15	26.5	6.3	8.8	12.9	7.8
boomer						
105 J	5	26.5	7.2	24.8	40.2	18.9
sparker						
100 J	15	16.7	1.0	12.1	??	10.8
watergun						
15 in^3 80 bar	30	21.8	0.9	36.7	54.3	28.9
airgun						
10 in^3 80 bar	25	26.5	0.5	5.5	9.4	7.0
10 in^3 120 bar	25	26.5	0.5	6.5	7.4	6.1
sleevegun						
6 in^3 80 bar	30	45.0	0.6	4.5	??	4.5
6 in^3 120 bar	30	45.0	0.6	5.3	??	5.1

Table III. Overview of source frequency characteristics for non-zero offset source signatures. Tabulated are the measured dominant frequency, -40 dB bandwidth, +6 dB NBW, and calculated bandwidth (CBW) for non-zero offset source signatures.

Chapter 3

Iterative Inversion of Seismic Data using Singular Value Decomposition[1]

Abstract

One of the objectives of processing seismic data is to increase the resolution. Inversion (deconvolution) of the seismic data traces is one of the methods to achieve this. In this chapter an iterative method is proposed for inversion. The convolutional forward model can be written in matrix notation. The inversion is performed using Singular Value Decomposition (SVD), which in addition gives insight into the stability of the inversion.

If inversion is carried out assuming a reflector at each sample point, small eigenvalues render the method unstable. To avoid this, three methods are suggested. The first two stabilize the inversion by treating small eigenvalues at the expense of resolution. The third approach involves a restriction on the number of unknowns. This restricts the number of reflectors allowed in the forward model, but is not always accurate since the initial reflector positions can be wrong.

Finally, an iterative inversion method is proposed to improve the reflector positions. In this approach stability (restricted number of reflectors) is achieved with increased resolution by varying the reflector positions. In each iteration step the reflectors can be moved to new positions. From these a new model is calculated, which improves the fit of the data and model significantly. The influence of noise, number of reflectors and wavelet shape on the inversion are discussed.

---

1 This chapter has been submitted for publication in Geophysical Prospecting

3.1 *Introduction*

In this chapter the inverse problem is formulated as: "Obtain information about the reflector depths (in time) and the reflection strength of these reflectors from single channel (marine) seismic signals". The inversion is based on a forward model description. It is assumed that the reflected seismic signal can be described as the convolution of a wavelet which represents the source, and a spike train (sparsely populated) which represents the impulse response of the earth, plus some additive noise. This can be expressed as:

$$s(t) = w(t) * r(t) + n(t) \qquad [3.1]$$

where $s(t)$ is the signal, $w(t)$ is a wavelet, $r(t)$ is the reflectivity function of the earth, $n(t)$ is the noise and * denotes convolution. If r is of length k, w of length m the trace s will be of length $n = m + k - 1$. In matrix notation equation [3.1] can be written as:

$$\vec{s} = \begin{pmatrix} s_1 \\ . \\ . \\ . \\ . \\ s_n \end{pmatrix} = \mathbf{W}\vec{r} + \vec{n} = \begin{pmatrix} w_1 & 0 & 0 & . & 0 \\ . & w_1 & 0 & . & . \\ w_m & . & w_1 & . & 0 \\ 0 & w_m & . & . & w_1 \\ . & 0 & w_m & . & . \\ 0 & 0 & 0 & . & w_m \end{pmatrix} \cdot \begin{pmatrix} r_1 \\ . \\ . \\ . \\ r_k \end{pmatrix} + \begin{pmatrix} n_1 \\ . \\ . \\ . \\ . \\ n_n \end{pmatrix} \qquad [3.2]$$

The columns of **W** represent a time shifted version of the wavelet. In each column of **W** the wavelet is shifted one sample and represents a reflected wavelet at that reflector position. The elements of vector $\vec{r}$ are the reflector amplitudes.

The goal of inversion is to find a model $\vec{r}$ that will minimize $|\mathbf{W}\vec{r} + \vec{n} - \vec{s}|^N$. Deconvolution techniques which use the L_1 norm ($N = 1$) are described by Claerbout and Muir (1973), Chapman and Barrodale (1983) and Barrodale et al. (1984). Chapman and Barrodale (1983) use an iterative method. At each step a single spike is extracted from the data. The amplitudes of previously extracted spikes are updated, while their positions are fixed. This method does not work well for closely spaced spikes (Barrodale et al., 1984). The optimization is done with methods that do not require derivatives of the objective function, such as the simplex method. The simplex method is described in several textbooks (e.g. Press et al., 1988).

In this chapter the L_2 norm ($N = 2$) is used, which leads to the well known least-squares minimization:

$$\text{minimize } (\mathbf{W}\vec{r} + \vec{n} - \vec{s})^2 \quad \text{with respect to } \vec{r} \qquad [3.3a]$$

This gives:

$$\mathbf{W}^T\mathbf{W}\vec{r} + \mathbf{W}^T\vec{n} - \mathbf{W}^T\vec{s} = 0 \qquad [3.3b]$$

The cross-correlation between the wavelet and the noise, $\mathbf{W}^T\vec{n}$, is assumed to be zero and equation [3.3b] can be rewritten as:

$$\mathbf{A}\vec{r} = \vec{b} \qquad [3.4]$$

where $\mathbf{A} = \mathbf{W}^T\mathbf{W}$ and $\vec{b} = \mathbf{W}^T\vec{s}$. $\mathbf{A}$ is the autocorrelation of the wavelet and $\vec{b}$ is the cross-correlation between the wavelet and the data. $\mathbf{A}$ is a square matrix and its number of rows and columns is equal to the number of columns in $\mathbf{W}$.

Several methods exist for the inversion of a seismic trace using the L_2 norm if the wavelet is known (e.g. Robinson and Treitel, 1980, Lines and Treitel, 1984). In the Gauss-Newton method equation [3.4] is rewritten as:

$$\vec{r} = (\mathbf{W}^T\mathbf{W})^{-1}\mathbf{W}^T\vec{s} \qquad [3.5a]$$

In solving equation [3.5a] one can take advantage of the symmetry in the autocorrelation matrix and use Toeplitz methods (Robinson and Treitel, 1980, Press et al., 1988). If the autocorrelation matrix is (nearly) singular the Toeplitz method will break down and other methods are necessary to solve equation [3.5a]. The Marquardt-Levenberg (ML) method avoids problems from (near) singularities by adding a constant β to the main diagonal of $\mathbf{W}^T\mathbf{W}$, that is adding a constant to the eigenvalues of $\mathbf{W}^T\mathbf{W}$ so that none of them can vanish. In the ML method equation [3.5a] is changed to:

$$\vec{r} = (\mathbf{W}^T\mathbf{W} + \beta\mathbf{I})^{-1}\mathbf{W}^T\vec{s} \qquad [3.5b]$$

For small β the ML method behaves like the Gauss-Newton method.

In this chapter Singular Value Decomposition (SVD) is used to recover the reflection response, because SVD gives more control and insight in the inversion (Sluis, v.d. and v.d. Vorst, 1987, Riel v. and Berkhout, 1985).

3.2 *SVD Inversion Method*

Any $m \times n$ matrix **A** can be rewritten as (Sluis, v.d. and v.d. Vorst, 1987):

$$\mathbf{A} = \mathbf{U}\Sigma\mathbf{V}^T \qquad [3.6]$$

where **U** is an orthogonal $m\ x\ m$ matrix, Σ is a $m\ x\ n$ diagonal matrix, with diagonal elements $\sigma_1 \geq \sigma_2 \geq .. \geq \sigma_n \geq 0$ and $\mathbf{V}^T$ is the transpose of orthogonal $n\ x\ n$ matrix **V**. The columns of **U**, $\vec{u}_i$, are the eigenvectors of $\mathbf{A}\mathbf{A}^T$ and the columns of **V**, $\vec{v}_i$, are the eigenvectors of $\mathbf{A}^T\mathbf{A}$. Thus

$$\mathbf{A}\mathbf{A}^T\ \vec{u}_i = \lambda_i^2\ \vec{u}_i \qquad i = 1, \ldots\ldots, m \qquad [3.7]$$

and

$$\mathbf{A}^T\mathbf{A}\ \vec{v}_i = \gamma_i^2\ \vec{v}_i \qquad i = 1, \ldots\ldots, n \qquad [3.8]$$

For $i = 1, \ldots, n$ it can be shown that the eigenvalues γ_i^2 and λ_i^2 are equal, $\gamma_i^2 = \lambda_i^2 = \sigma_i$ and the remaining eigenvalues in the larger set are zero (Sluis v.d. and v.d. Vorst (1987), Riel v. and Berkhout (1985)). The inverse of **A** can be written as :

$$\mathbf{A}^{-1} = \mathbf{V}\Sigma^+\mathbf{U}^T \qquad [3.9]$$

where Σ^+ is a $m\ x\ n$ diagonal matrix, with diagonal elements $1/\sigma_1 \leq 1/\sigma_2 \leq .. \leq 1/\sigma_n$. The solution of equation [3.4] is then:

$$\vec{r} = \mathbf{V}\Sigma^+\mathbf{U}^T \cdot \vec{b} \qquad [3.10]$$

After the decomposition of the matrix (equation [3.6] and [3.9]) the solution is obtained by back substitution of the data vector $\vec{b}$ (equation [3.10]). Equation [3.10] shows that in the back substitution the data are divided by the elements of diagonal matrix Σ, the eigenvalues.

Direct SVD inversion is unstable because small eigenvalues (σ_j) can dominate the result. One method to stabilize the inversion is to replace ($1\ /\ \sigma_j$) in equation [3.10] by ($1\ /\ (\sigma_j + \varepsilon)$), where ε is a small value. When σ_j becomes very small ε will assure that the solution will remain stable. When $\sigma_j \gg \varepsilon$ then ε has almost no influence on the solution. When σ_j and ε are of the same order a loss in resolution results.

Another method to stabilize the inversion is to exclude equations with σ_j smaller than a certain threshold (η). A disadvantage is that there are more

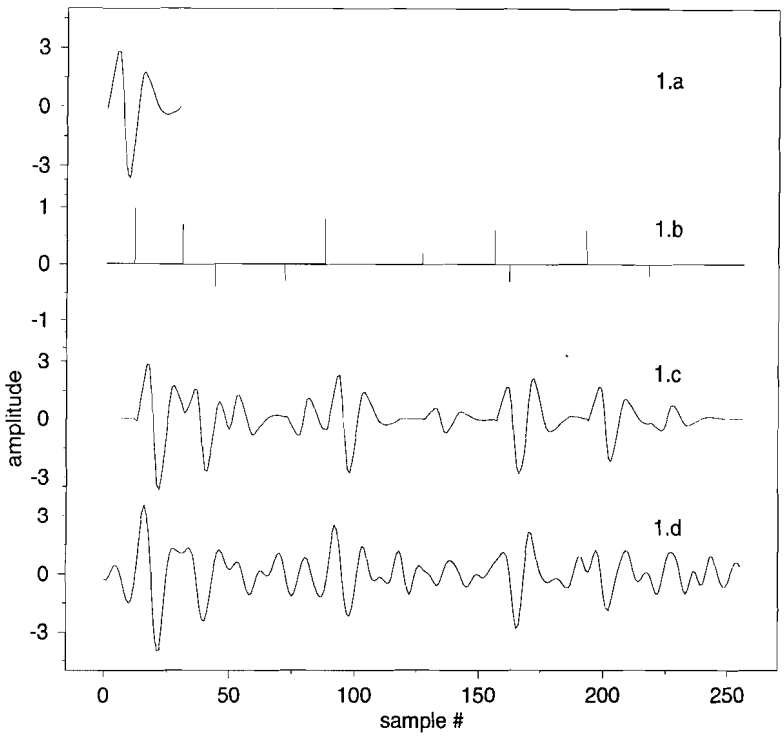

Figure 1. The forward convolutional model. (a) the measured boomer wavelet, (b) the input reflection model, (c) the result of the convolution between the wavelet and the model, (d) the noisy data trace, S/N = 4.

unknowns (reflectors) than equations, and as a result the solution will be 'smeared' over several samples.

3.3 *SVD Inversion, With and Without Stabilization*

First a synthetic data trace is constructed following the convolutional forward model. Figure 1.a shows a measured boomer wavelet (Verbeek and McGee, 1995) and figure 1.b shows a reflection response model. These are convolved to obtain the data trace plotted in figure 1.c. Random noise, in the same

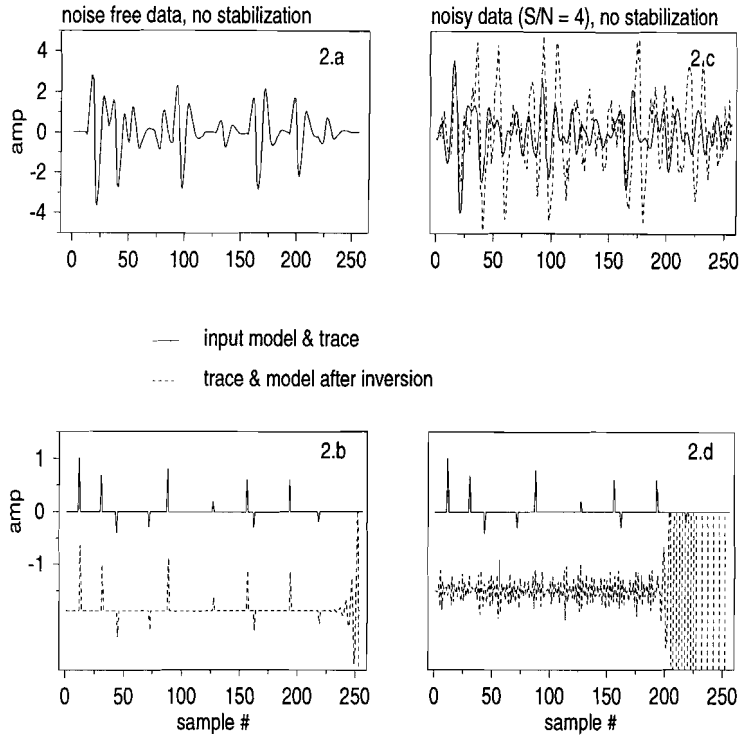

Figure 2. Results of inversion without stabilization, (a) the noise-free input trace (solid line) and output trace (dashed line), (b) the input model (solid line) and output model (dashed line) for noise-free data, (c) the noisy input trace (solid line) and output trace (dashed line), (d) the input model (solid line) and output model (dashed line) for noisy data.

frequency band as the data, is added to the trace resulting in a S/N ratio of four, the result is plotted in figure 1.d. Here the S/N ratio is defined as:

$$S/N = \frac{\max |signal|}{\max |noise|} \qquad [3.11]$$

Figures 2.a and 2.b show the results of SVD inversion of noise-free data and figure 2.c and 2.d show the results of inversion with noisy data (S/N = 4). In

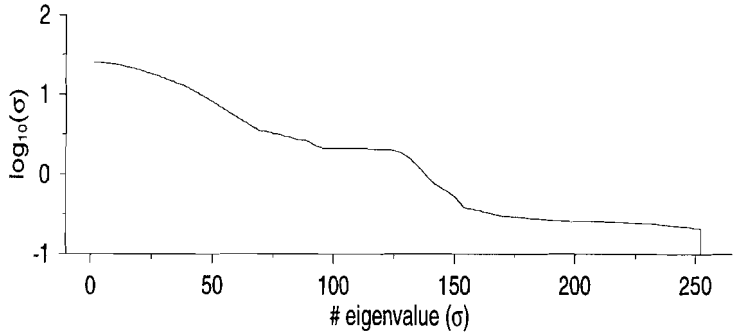

Figure 3. The $\log_{10}$ of the eigenvalues of equation [3.8] for the example trace and wavelet of figure 1.

figures 2.a and 2.c the input trace (solid line) and output trace (dashed line) are shown, where output trace means the trace constructed by convolution of the input wavelet with the model obtained from inversion (the output model). In figures 2.b and 2.d the input model (solid line) and output model (dashed line) are shown. The output trace for the noise-free data almost perfectly fits the input data. The output model is a good representation of the input model, except for the last part. The output model for the noisy data gives no information about the input model. Also, the data fit for the noisy data is not good. In figure 3 the eigenvalues are plotted. Most eigenvalues are between 0.2 and 25 ($\log_{10}$ between -0.7 and 1.4).

The data fit is defined as:

$$\text{data fit} = 1 - \frac{\sum_{i=0}^{i=N-1} |s_i - t_i|}{\sum_{i=0}^{i=N-1} |s_i|} \qquad [3.12]$$

where N is the number of samples in the trace, s_i is the input data and t_i is the output trace. Figure 4 shows the data fit as a function of the stabilization parameter ε for noise-free data (figure 4.a) and for noisy data (S/N = 4, figure 4.b). Figure 4 also shows the data fit as a function of the stabilization threshold η for noise-free data (figure 4.c) and for noisy data (S/N = 4, figure 4.d). For values of the stabilization parameters below 0.1 ($\log_{10}$ below -1) the effect of the smallest

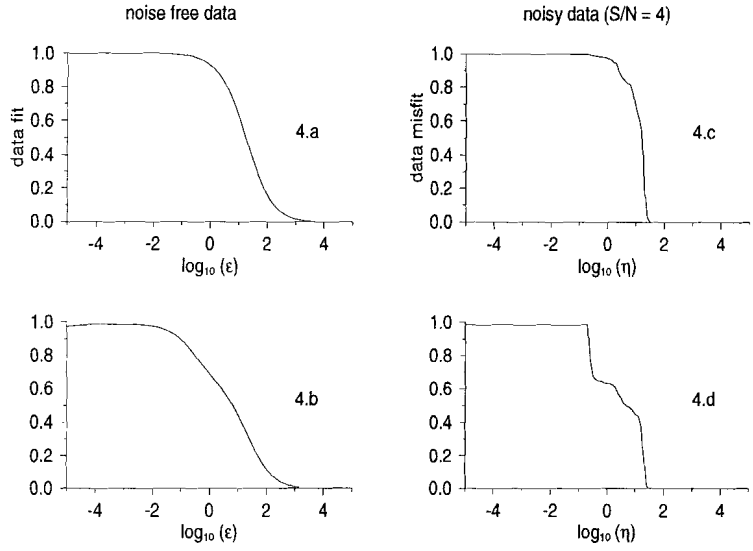

Figure 4. Data fit as function of stabilization parameters, (a) the results for the ε method for noise-free data, (b) the results for the ε method for noisy data (S/N = 4), (c) the results for the η method for noise-free data, (d) the results for the η method for noisy data (S/N = 4).

eigenvalues is 'stabilized' and a good data fit results from the inversion. The data fit equals 1 for the noisy free data and is 0.975 for the noisy data. Increasing ε decreases the data fit. When ε becomes too large it will dominate the inversion and finally a zero model is obtained from the inversion (total damping); the data fit becomes zero. For small values of η (below 0.2 or $\log_{10}$ below -0.7) only the equations with the smallest eigenvalues are excluded from the inversion and the data fit remains constant. By increasing η more and more equations are excluded and in the end no equations are used and the result then is a zero model, the data fit equals zero. Both stabilization methods give comparable results for the noise-free data and for the noisy data.

Figure 5 shows the results after stabilized SVD inversion, with $\eta = 0.001$ for the noise-free data and for the noisy data. Figures 5.a and 5.b show the results for inversion of noise-free data and figure 5.c and 5.d show the results for inversion with noisy data (S/N = 4). In figures 5.a and 5.c the input trace (solid line) and

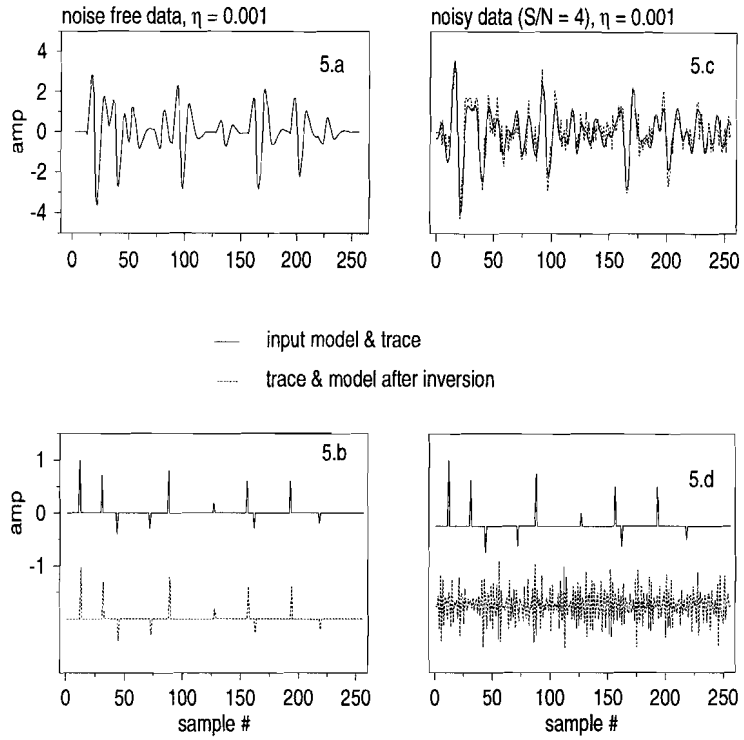

Figure 5. Results from inversion with $\eta = 0.001$ for noise-free data and for the noisy data, (a) the noise-free input trace (solid line) and output trace (dashed line), (b) the input model (solid line) and output model (dashed line) for noise-free data, (c) the noisy input trace (solid line) and output trace (dashed line), (d) the input model (solid line) and output model (dashed line) for noisy data.

output trace (dashed line) are shown, figures 5.b and 5.d show the input model (solid line) and output model (dashed line). For the noise-free data the output model is a good representation of the input model and the data fit is perfect. The data fit of the noisy data is good (0.975) but the output model is a poor representation of the input model. The high data fit is also a result of the good fit of the noise. The data fit between the noise-free and the noisy data is about 0.51.

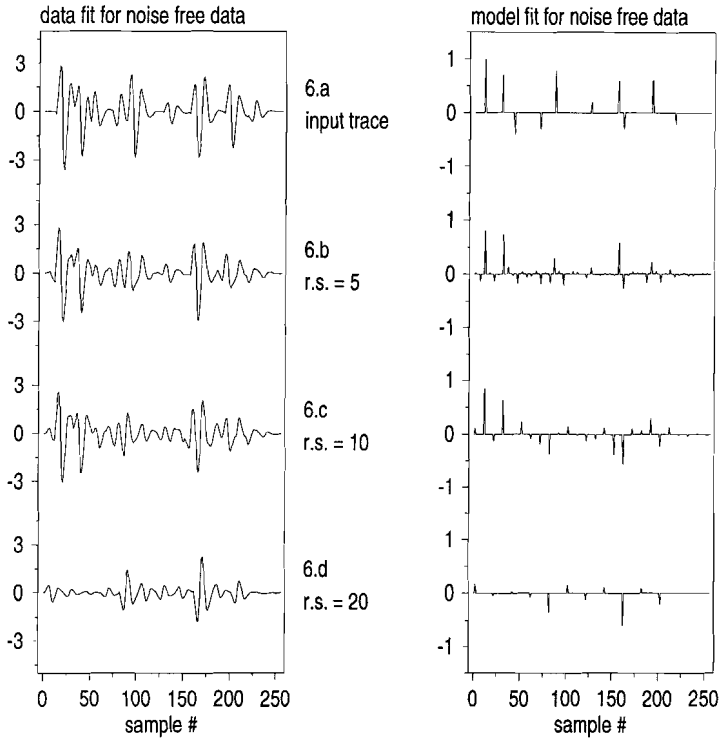

Figure 6. Results from inversion with noise-free data and the number of reflectors restricted and placed at equidistant positions. The left side of the figure shows the data traces and the right side the models. (a) the input data and model, (b) the results after inversion with a reflector separation (r.s.) of 5 samples, (c) the results after inversion with r.s. is 10 samples, (d) the results after inversion with r.s. is 20 samples.

3.4 *Fixed Number and Positions of Reflectors*

The performance of the previous described methods is poor for noisy data. When η is used for stabilizing there are more unknowns (reflectors) than equations and therefore the solution is 'smeared' over several samples, resulting in a somewhat decreased resolution. To increase the resolution more equations than

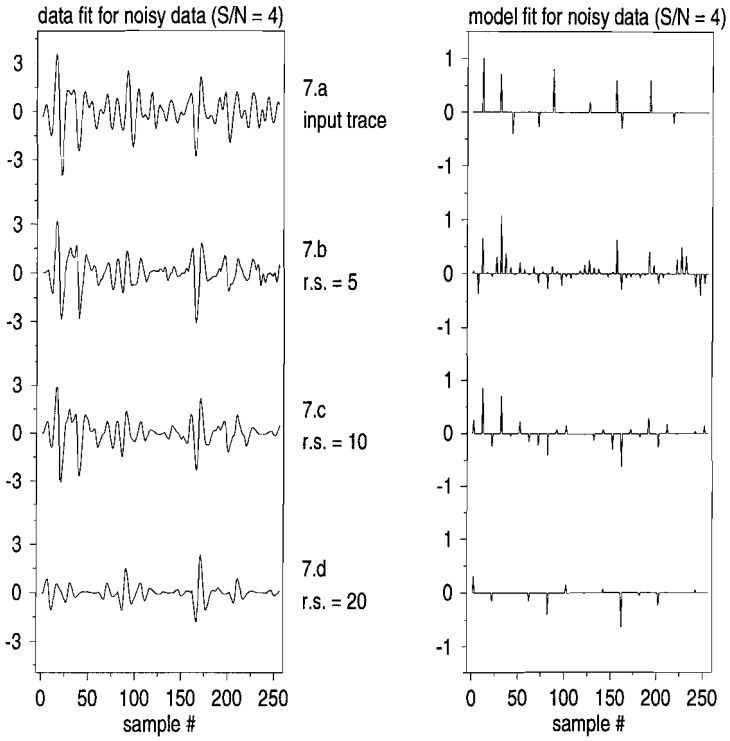

Figure 7. Results from inversion with noisy data (S/N = 4) and the number of reflectors restricted and placed at equidistant positions. The left side of the figure shows the data traces and the right side the models. (a) the input data and model, (b) the results after inversion with a reflector separation (r.s.) of 5 samples, (c) the results after inversion with r.s. is 10 samples, (d) the results after inversion with r.s. is 20 samples.

unknowns are needed. This can be accomplished by restricting the number of reflectors involved in the forward model (Riel v. and Berkhout, 1985). Matrix **W** (equation [3.2]) is a square matrix with the wavelet in its columns, every column shifted by one sample. Restricting the number of reflectors means that **W** consists only of columns with the time shifts of the wavelet equal to the expected reflector times. The number of columns and unknowns (reflector amplitudes) is largely

reduced. Another advantage is that the computing time required will be less since the size of the squared matrix $\mathbf{W}^T\mathbf{W}$ (equation [3.4]) is proportional to the number of reflectors.

The correct positions and number of reflectors are normally not known. If there is no a priori information, the reflectors can be placed at equidistant time intervals. The results of inversion with reflector separations of 5, 10 and 20 samples are shown in figures 6 and 7. Figure 6 shows the results for noise-free data and figure 7 shows the results for noisy data (S/N = 4). For smaller reflector separations the noise becomes dominant and the solution is less stable. Increasing the time interval between the reflectors makes the solution more stable. A disadvantage of restricting the number of reflectors and fixing the positions of the reflectors is that only at the positions where the reflectors are placed amplitude information is obtained. If these are not the correct positions, wrong amplitudes for the reflectors result. The data fit for noise-free data and inversion with a reflector separation of 20 samples is 0.07 and the data fit for noisy data is 0.08. For reflector separations of 10 and 5 samples the data fits are respectively 0.39 and 0.50 (noise-free data) and 0.18 and 0.23 (noisy data).

For both the noisy and the noise-free data, restricting the number of reflectors does not give better results than stabilizing the inversion by using η in the inversion.

3.5 *Iterative Inversion with Moving Reflector Positions*

Inversion with SVD and a restricted number of reflectors at fixed positions gives stable though not always very accurate solutions. To improve the solution in order to get more information about the area between the initial reflector positions, I propose an iterative inversion method. In this iterative method the resolution of the inversion with a restricted number of reflectors is increased by varying the reflector positions.

The first step in this iterative method is the SVD inversion with the reflectors at fixed initial positions. After this first step the reflector with the smallest amplitude is removed. Then, the positions of all remaining reflectors are updated. The amplitudes of the reflectors remain constant during the position update.

The new position of the first reflector is found by fitting it between the first sample of the trace and the position of the second reflector. The new position is the position that gives the best fit between the input data and the output data. In the

search for this reflector position all other reflector positions are fixed. When the first reflector is placed at its new position, the new position of the second reflector is determined. This new position must be between the new position of the first reflector and the position of the third reflector. Again, during the search for this new reflector position all other reflector positions are fixed. After the new position of the second reflector is found, the search for the new position of the third reflector starts and for the fourth and so on. Starting the search for the new positions at the first reflector and ending at the last reflector can give slightly different results than starting the search at the last reflector and ending at the first reflector.

After the reflector positions are updated a new reflector is placed. The new reflector is placed in such a way that the solution in the area around the sample with the lowest fit will improve. First the sample (position) with the lowest fit is determined. Then the position of the nearest reflector before that 'lowest fit sample' is found. The position of the new reflector is halfway between these two positions (samples). The position of this new reflector is located before the 'lowest fit sample' since a causal wavelet is used in the forward model.

With the reflectors placed at the new positions the next iteration step is again SVD inversion with fixed (new) positions for the reflectors. Then, with the new amplitudes, new reflector positions are searched for and then a new SVD inversion is done, etc. The iteration steps are repeated until a stop criterion is reached. This can be the data fit, number of iteration steps, difference with model in last iteration steps, difference with data fit in last iteration steps, etc. Removing the reflector with the smallest amplitude is necessary to give the other reflectors freedom to move to their new positions. Placing the new reflector helps to solve the area with the lowest data fit and keeps the number of reflectors constant and the method remains stable.

Figure 8 shows the first three steps of this iterative inversion scheme for noise-free data. The result after four iterations (inversion and new positions) is also shown. Figure 8.a shows the input data and model. The first step is SVD inversion with the reflectors at fixed positions. Figure 8.b shows the result after inversion with reflectors fixed with a separation of 20 samples. Next, the reflector with the smallest amplitude, marked by an arrow, is removed. The effect of the next step in the iterative method, the shifting of the reflector positions, is shown in figure 8.c. Reflector 1 is moved from sample 1 to sample 11, the reflectors around samples 60, 80, 100 and 120 are moved between sample 70 and 90 and the reflector at sample 200 is moved to sample 218. This shifting increases the data fit four times, from 0.07 to 0.32. In the next inversion step the data fit is further increased to 0.72. The

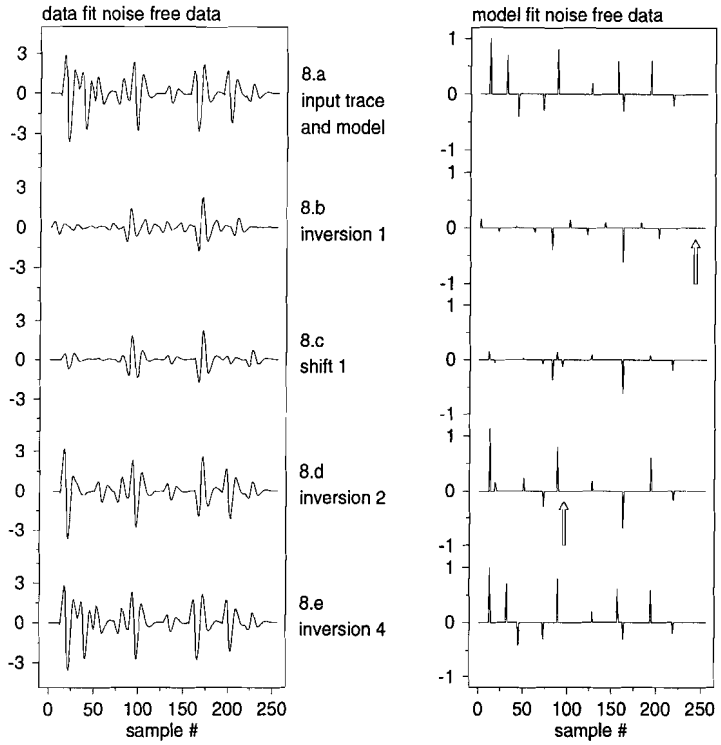

Figure 8. Results of the iterative inversion with moving reflectors for noise-free data, (a) the input data trace and model, (b) the result after inversion with fixed reflectors with a reflector separation of 20 samples, the reflector with the smallest amplitude is marked by an arrow, (c) the results after moving the reflectors to their new positions, (d) the results after the new amplitudes are found on the new positions, (e) the results after 4 iterations.

new model is shown in figure 8.d. After 4 iterations a perfect data fit (1.0) and model fit is reached. Figure 8.e shows the results after 4 iterations.

The results for the first three steps of iterative inversion of noisy data are shown in figures 9.b, 9.c and 9.d. The iterative SVD inversion with moving reflectors gives good results: After 4 iterations, figure 9.e, the data fit is improved

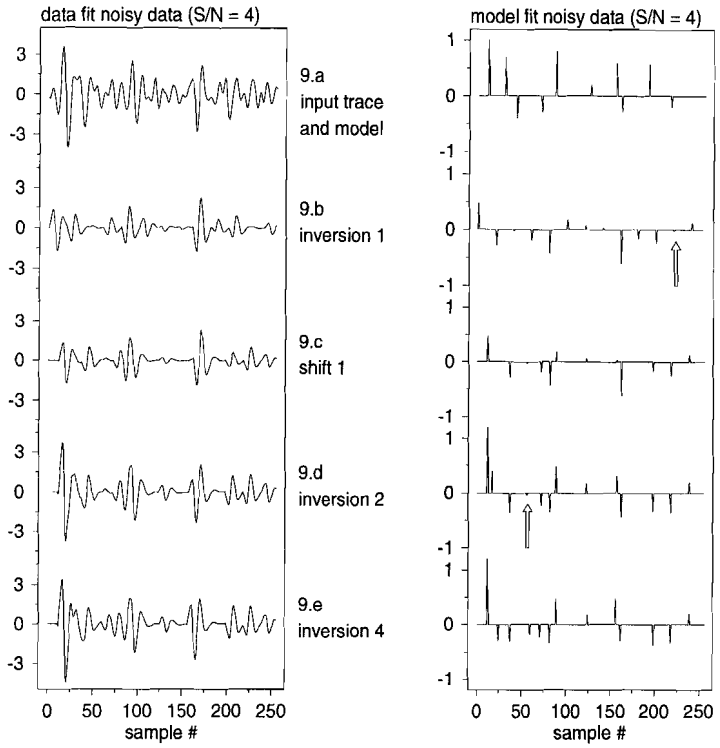

Figure 9. Results of the iterative inversion with moving reflectors for noisy data (S/N = 4), (a) the input data trace and model, (b) the result after inversion with fixed reflectors at 20 samples separation, the reflector with the smallest amplitude is marked by an arrow, (c) the results after moving the reflectors to their new positions, (d) the results after the new amplitudes are found on the new positions, (e) the results after 4 iterations.

from 0.08 to 0.54 and the reflector model is closer to the input model than the model obtained using fixed positions in the inversion (figure 9.b). The data fit after 4 iteration steps with moving reflectors is about half of the the data fit after stabilized SVD inversion with η or ε as stabilization parameter (0.54 vs. 0.975). A comparison between figure 9.e and figure 5.d shows that the model obtained with the iterative method is better than the model obtained with stabilized SVD

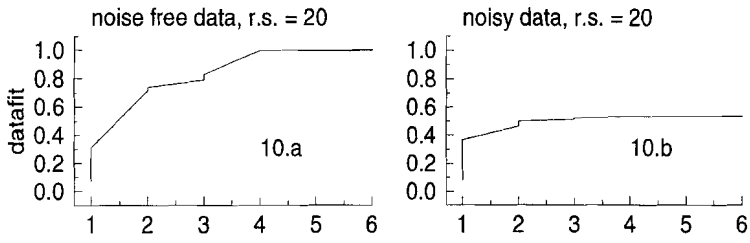

Figure 10. Data fit vs. the number of iterations, (a) the data fit with an initial reflector separation of 20 samples and noise-free data, (b) the data fit with an initial reflector separation of 20 samples and noisy data (S/N = 4),

inversion. This contradiction, a better model fit and a lower data fit, is because the moving reflector method does not fit the noise in the data as well as the stabilized SVD inversion does. The data fit of the solution with the moving reflectors after 4 iterations is seven times larger than the data fit with the reflectors at fixed positions (with a separation of 20 samples) for the noisy data, 0.54 versus 0.08.

Figure 10 shows the data fit versus the number of iterations for the model with an initial reflector separation of 20 samples for the noise-free data (figure 10.a) and the noisy data (figure 10.b). Compared to the data fit with fixed reflectors (iteration step 1) a significant improvement of the data fit is obtained for both the noise free and the noisy data trace. The data fit improves a factor seven with moving reflectors in the presence of noise compared to the fixed reflector method. In the absence of noise the fit can become perfect. Most of the improvement is reached within a few iterations for the noise-free data as well as for the noisy data. Figure 10 shows that the first move of the reflectors already gives a large improvement in the data fit: The reflectors are much closer to their correct positions. The data fit remains constant after four iteration steps.

For the inversion of one trace the iterative method is faster than inverting the "full" matrix. The inversion of the "full" matrix, where each sample represents a reflector position, is about N^2 times slower than inversion of a matrix with a reflector separation of N samples. Shifting the reflectors takes a few percent of the time it takes to invert the "full" matrix. However, if the wavelet remains constant from trace to trace, the "full" matrix has to be inverted only once and can be used

for all traces in a section. A disadvantage of the iterative method is that the matrices have to be inverted for each trace separately. At the moment, iterative inversion of one trace (as shown in this chapter) takes about 4 seconds cpu time on a SUN-SPARC20-514 system with Solaris 2.3 as operating system. With faster computers and optimal coding of the program the time will become less than a second, so 'on-line' iterative inversion can be done in the field.

3.6 *Wavelet Shape*

Inversion of synthetic data using the minimum phase equivalent of the boomer wavelet leads to similar results compared to the inversion with the boomer wavelet. Hence, the phase of the wavelet has a minor influence on the results of iterative inversion with moving reflectors. However, in the previous sections the same wavelet was used to construct the data traces and to perform the inversion (building the matrix $\mathbf{W}$ in equation [3.2]). Normally, the 'true' wavelet is not known and the inversion is performed using an approximation of the wavelet. This is simulated by constructing the data with the boomer wavelet and constructing the inversion matrix from the minimum phase equivalent of the boomer wavelet. Figure 11.a shows two wavelets, one which was used to make the data trace (left) and one (right) which was used for the inversion (matrix construction). The right wavelet is the minimum phase equivalent of the left wavelet. Figure 11.b shows the noise-free data trace and the input model. The result of inversion using stabilization ($\eta = 0.001$) is shown in figure 11.c, the results of inversion with the reflectors fixed at equidistant position with a separation of 20 samples is shown in figure 11.d and the results after four iterations with moving reflectors (starting with an initial reflector separation of 20 samples) are shown in figure 11.e. The data fit of the stabilized inversion is the best (figure 11.c). Iterative inversion with moving reflectors gives better results than the fixed reflector method. Figure 12 shows the results of inversion of noisy data (S/N = 4) with the 'wrong' wavelet. Inversion with SVD and stabilization ($\eta = 0.001$) gives the best data fit but a poor model fit. The fixed reflector method also gives a poor model fit. The best model fit is obtained with the iterative inversion with moving reflectors, but even this method gives incorrect results. For reliable results a good knowledge of the wavelet shape is necessary.

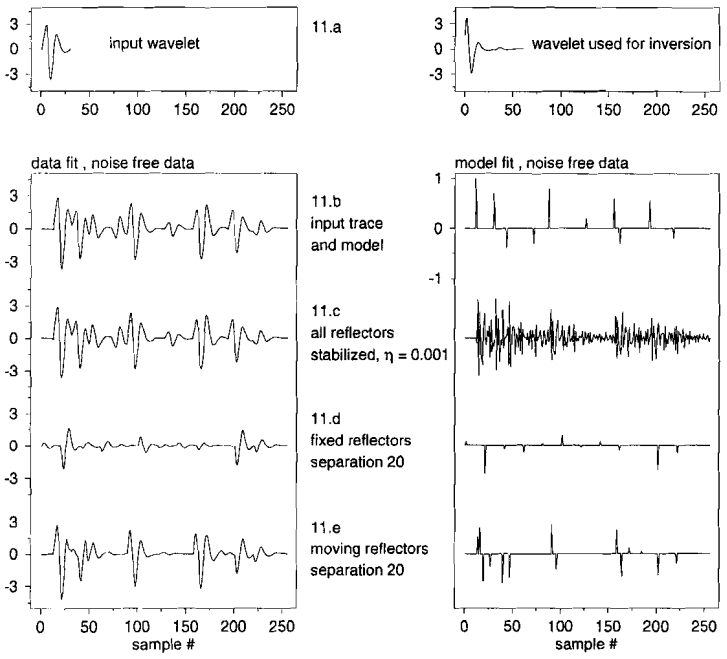

Figure 11. Results using different wavelets to construct the noise-free data trace and to invert the data. The data are shown on the left and the models on the right. (a) the left wavelet is used to construct the data trace and the right wavelet is used for the inversion, (b) the input data and model, (c) the results for stabilized inversion ($\eta = 0.001$) with a reflector separation of 1 sample, (d) the results for a fixed reflector separation of 20 samples, (e) the results after 4 iterations for the iterative inversion method with an initial reflector separation of 20 samples.

3.7 *Conclusions*

In this chapter several inversion techniques based on the convolutional forward model and undamped SVD inversion were discussed. Small eigenvalues render the SVD inversion method unstable.

The method can be stabilized by using a stabilization parameter which suppresses the influence of small eigenvalues. For noise-free data this leads to very

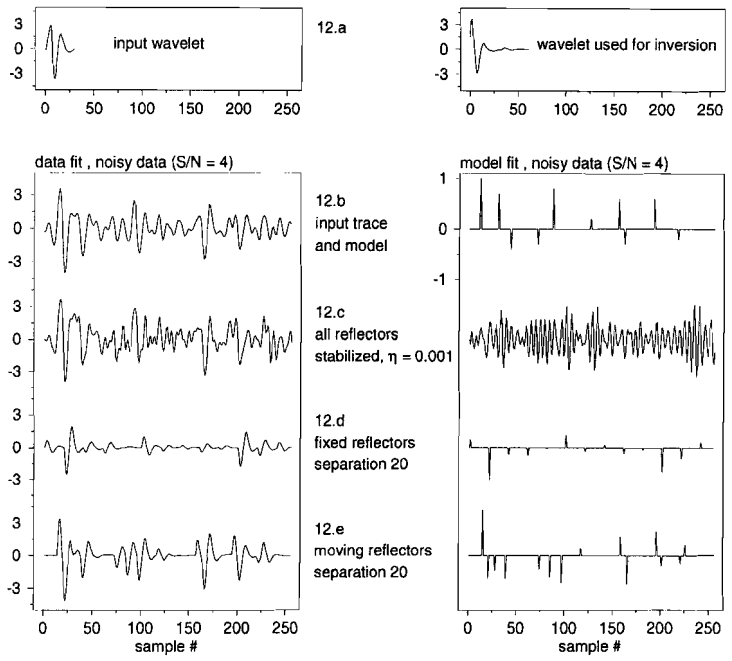

Figure 12. Results using different wavelets to construct the noisy data trace (S/N = 4) and to invert the data. The data are shown on the left and the models on the right, (a) the left wavelet is used to construct the data trace and the right wavelet is used for the inversion, (b) the input data and model, (c) the results for stabilized inversion ($\eta = 0.001$) with a reflector separation of 1 sample, (d) the results for a fixed reflector separation of 20 samples, (e) the results after 4 iterations for the iterative inversion method with an initial reflector separation 20.

good results, a good data fit and a good model fit. Noisy data, however, do not give stable results; they give a good data fit but a poor model fit. Using a stabilization parameter stabilizes the inversion but decreases the resolution.

Another method of stabilizing the inversion is restricting the number of reflectors involved in the inversion. The positions and the number of reflectors are normally unknown. Placing the reflectors at equidistant positions and performing the inversion gives stable results. If the reflector separation is small, the noise

becomes dominant, but if the reflector separation is large no information about the space between the reflectors is obtained. Restricting the number of reflectors stabilizes the solution but gives erroneous amplitudes.

An iterative SVD inversion method was proposed to improve the reflector positions. In this method a stable method (restricted number of reflectors) is combined with more resolution by varying the reflector positions. In each iteration step the reflectors can be moved to a new position. Compared to the stabilized SVD inversion and SVD inversion with fixed reflector positions, this iterative method gives better results for data with and without noise.

Knowledge of the wavelet shape is very important to obtain good inversion results (models). When wrong wavelets are used for stablized SVD inversion the solution can have a good data fit, but the model fit will be poor. This is valid for both noise-free and for noisy data. The iterative method gives data fits comparable to the data fits for stabilized inversion, but models which are most of the time better.

In general the iterative SVD inversion method with moving reflectors gives stable and more accurate results than stabilized SVD inversion and SVD inversion with fixed reflector positions.

Chapter 4

Genetic Algorithms for Inversion of Seismic Data[1]

4.1 Introduction

Most inversions involve some kind of optimization. Local optimization methods are described by several authors (e.g. Press et al., 1988, Lines and Treitel, 1984, and many others). These methods search for a local optimum of the objective function. If this local optimum is not the same as the global optimum, a non-optimal solution to the inverse problem is found. The local methods are so-called 'down-hill' methods; they search only in a direction towards better models. To find the true model, the starting model must be close enough to the true model in the sense that there is a 'down-hill' path from the starting model towards the true model. Down-hill means that in each step of the inversion the fitness of the new model is better than the fitness of the old model and the error between measured data and modeled data decreases in each step. For local methods a good a priori estimate of the model is necessary. The method presented in Chapter 3 is an iterative local method.

Another group of techniques are the so-called global search algorithms. In the global methods a random component is added to the search in the model space so that the 'down-hill' restriction does not apply to these methods. The global methods do not make use of gradients or derivatives of the objective or fitness function. This means that for global methods a broader range of fitness functions can be used. Another advantage of global methods is that only the forward model is calculated and therefore they are not sensitive to instabilities in the inversion.

Monte Carlo (MC) and Simulated Annealing (SA) are two well-known global search methods. MC methods are based on a random sampling of the model space. SA can be seen as a controlled random search with a random starting model. This model is randomly changed and the fitness of the new model is

---

1 This Chapter is submitted for publication in Geophysical Prospecting.

calculated. With a certain algorithm (e.g. Metropolis algorithm, Press et al., 1988, Sen and Stoffa, 1992) it is decided if the new model will replace the old model. A new model with a higher fitness than the old model is always accepted, a new model with a lower fitness is sometimes accepted. The difficulty with SA is finding a good algorithm (cooling schedule) to decide whether or not to accept the new model (Sen and Stoffa, 1992).

Genetic Algorithms (GA) also belong to the group of global search algorithms. Some authors (e.g. Gallagher et al., 1991, Sambridge and Drijkoningen, 1992) show that GA solves global optimization problems more efficiently than MC. The difference in performance between GA and SA is less clear and depends on the particular problem (Sambridge and Drijkoningen, 1992). The advantage of GA is that it uses the information of previously tested models in the search algorithm.

This chapter begins with a discussion of various aspects of GA inversion. First the fitness function and model parametrization are discussed. Next, the basic steps of the GA, parent selection, crossover, mutation and generation selection are explained. Then, their application in the inversion of seismic data is discussed. It is shown that the results (models) from the GA inversion are biased by the settings of the control parameters of the GA. Therefore, it is proposed to do several GA runs with various settings of the control parameters and combine the models from these GA runs. Combining the results makes the GA inversion relatively insensitive to noise. Combining the models also gives insight into which parts of the model are resolved well and which parts are not.

4.2 *Theory of Genetic Algorithms*

4.2.1 *Fitness Function*

In this chapter two commonly used fitness functions are tested, the normalized correlation coefficient (*NCC*) and the squared error fitness (*SQE*). Following Stoffa and Sen (1991) the *NCC* can be written as:

$$NCC(m) = \frac{\sum_{i=0}^{i=N-1} d_i s_i(m)}{(\sum_{i=0}^{i=N-1} d_i d_i)^{1/2} (\sum_{i=0}^{i=N-1} s_i(m) s_i(m))^{1/2}} \qquad [4.1]$$

where m is the model to construct the modeled data $s_i(m)$, d_i are the measured data, i denotes the sample number and N is the total number of samples. If the modeled data correlate perfectly with the measured data (i.e. they are equal) the $NCC = 1$. If the correlation is very poor then NCC will be near zero.

The SQE is defined as:

$$SQE(m) = \frac{1}{\sum_{i=0}^{i=N-1} (d_i - s_i(m))^2} \qquad [4.2]$$

The squared error is inverted so that a good fit (small error) will correspond to a high value, and a poor fit (large error) will result in a low SQE. Both fitness functions must be maximized to correspond to a good fit between measured and modeled data.

Some authors (Stoffa and Sen, 1991, Sen and Stoffa, 1992 and Nolte and Frazer, 1994) suggest the use of a 'stretching' of the fitness function. Their argument is that it is undesirable that a good (highly fit) model in the original population dominates the future populations and the convergence of the algorithm early in the inversion. Later in the inversion, they argue, it is necessary to exaggerate the differences between almost equally fit models to be able to discriminate between these models.

The first part of their argument is correct. If the best models (models with the highest fit) in the starting population dominate the whole GA inversion, and these models are not near the true model, it is likely that a local optimum of the fitness function will be found. The second part of their argument does not hold. If two models are almost equally fit, one must admit that the fitness function used is not capable to discriminate between them and that it is better to use other criteria to make a choice between the models. Stretching the fitness function means that, in the later generation, one allows the GA search to be dominated by models that are slightly better, under the assumption that these slightly better models (in terms of fitness) are a better representation of the true model. It is more likely that these small differences in fitness are due to a better fitting of the noise. Another problem is how to define a proper stretching factor. This problem is comparable to defining a proper cooling strategy in simulated annealing (Sen and Stoffa, 1992).

Lomax and Snieder (1994) argue that it is always undesirable for individual models to dominate the GA search, in the beginning as well as towards the end of the GA inversion. They use a 'water level'; when the fitness of a model is better than this level the fitness of that model is reset to that level. Their GA

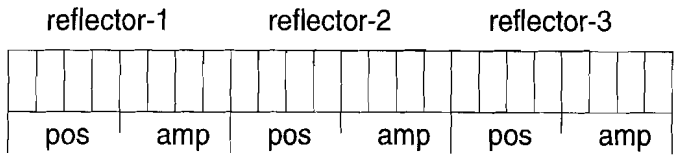

Figure 1. Model representation for three reflectors. Each reflector has 4 bits for position information and 4 bits for amplitude information.

gives a set of possible models and other criteria should be used to select a 'best' model, if desired. Their interest is to find the regions in the model space where the fitness is better than a certain 'water level'.

The suppression or the stressing of slightly better models can also be achieved by means other than redefining the fitness function. The parent selection and the generation selection parts of the genetic algorithm (sections 4.2.3 and 4.2.6) can also be used for this.

4.2.2 *Forward Model and Model Representation*

The forward model used in this chapter is the convolution model. The modeled data, $s(t)$, are described by :

$$s(t) = w(t) * r(t) \qquad [4.3]$$

where $w(t)$ is the wavelet, $r(t)$ is the reflectivity trace and * denotes the convolution. The reflectivity trace is the model which is to be found with help of GA. The model parameters in this chapter are reflector times (in samples) and the reflector amplitudes. The model vector looks like $(p_1, a_1, p_2, a_2, \cdots, p_n, a_n)$, where p_i is the position of the $i-th$ reflector and a_i is the amplitude of the $i-th$ reflector. Each model is represented by a single bit string code. The bit string representation for a model consisting of three reflectors is shown in figure 1. A binary code was used to represent the model parameters. In this example 4 bits are used for position information and 4 bits for amplitude information. If all bits are 'off' (zero), the parameter has its lowest value. If all bits are 'on' (one), the maximum value is assigned to the parameter. The number of bits per parameter is the same for each reflector. The total bit string length is the number of bits per reflector times the number of reflectors. When 3 reflectors are used, 4 bits for

position and 4 bits for amplitude, the bit string consists of 24 bits, giving about $1.7 \cdot 10^7$ possible models.

If the search space for the reflector position is between sample 1 and sample 16, 4 bits for position information gives a resolution of 1 sample. When the reflector position is assumed to be between sample 1 and sample 64, 4 bits for position information gives a resolution of 4 samples. Only every fourth sample can be checked as a possible reflector position.

4.2.3 *Parent Selection*

The step of parent selection returns in every GA iteration. The parent selection step in the GA inversion controls which models (parents) are chosen to create new models. The new models are created by crossover and mutation. In this chapter two parent selection methods are compared, the so-called roulette wheel (RW) method and a pair-wise selection method. The RW method is a commonly used method (e.g. Davis, 1991). In the RW method the chance that a model is selected is proportional to its fitness. The chance that model m is selected, ($P(m)$), can be written as:

$$P(m) = \frac{\phi(m)}{\sum_{i=0}^{i=N-1} \phi(i)} \qquad [4.4]$$

where $\phi(m)$ is the fitness of model m. An extended form of this selection criterion is (Davis, 1991, Gallagher et al., 1991, Sambridge and Drijkoningen, 1992):

$$P(m) = \frac{C(m)}{\sum_{i=0}^{i=N-1} C(i)} \qquad [4.5]$$

where $C(m) = a - b\phi(m)$ or $C(m) = A\exp[-B\phi(m)]$, which in fact changes the fitness function.

Wilson and Vasudevan (1991) use a pair-wise selection method. All models are ordered according to their fitness, after which models 1 and 2 are selected to create two new models. Then models 3 and 4 are selected and so on, until a whole new generation is created. In the next iteration models 2 and 3 are selected, models 4 and 5 are selected and so on.

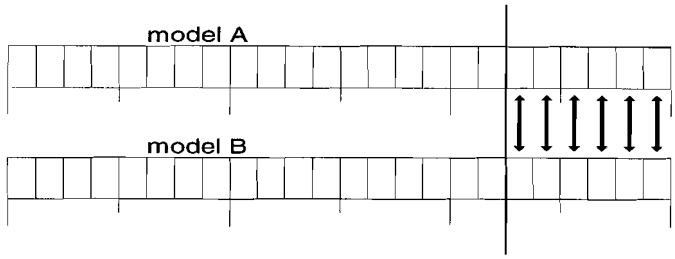

Figure 2 crossover; a crossover position (vertical bar) is selected at random. The bits to the right of this position are exchanged between the two models, the bits to the left of the crossover point are unchanged.

In this chapter a pair-wise parent selection method is also used, in which the best model is selected together with the worst model (model 1 with model N), then the second best with the second worst (model 2 with model $N-1$), etc. This pairing parent selection method is called the First-Last (FL) method. With this selection method it is possible that a relatively small but good part of a relatively poor model is combined, by crossover, with a good part of a good model and that this new combination gives a model with a higher fitness than the original models.

With the pair-wise parent selection method the chance that a good individual will dominate the GA inversion is avoided, since all models in the population are selected once to create new models.

4.2.4 *crossover*

In the crossover step, information is exchanged between members of the model population. In single-point crossover a crossover position is randomly selected. The bits to the right of this position are exchanged between the two models, the bits to the left of the crossover point are unchanged (see figure 2). Single-point crossover for the whole model is used by Gallagher et al. (1991) and Nolte and Frazer (1994). Stoffa and Sen (1991) and Sen and Stoffa (1992) use multi-point crossover, which means single-point crossover for each individual parameter in the model. Wilson and Vasudevan (1991) use uniform crossover; parameter values are exchanged between models.

In section 4.3 two crossover methods are tested. The first method is the multi-point crossover as described by Stoffa and Sen (1991) and Sen and Stoffa (1992), where for each parameter in the model one crossover point is selected. The chance that a parameter is crossed-over with a parameter from the other model is set to a value P_c. In the multi-point crossover it is possible that some parameters of the model are crossed-over and some other parameters are not.

The other crossover method is single-point crossover for the whole model with the restriction that the crossover point is at the boundary of a pair of parameters (reflector boundary). This means that the parameters of a reflector form a pair that cannot be separated by crossover. The new models are formed by a new combination of existing parameter values of the old models. The models are changed, but the values of the parameters are not changed by crossover.

4.2.5 *Mutation*

The mutation step of the GA is the controlling factor for random sampling of the model space. In the mutation step one or more bits are randomly selected and reversed in polarity from zero to one or vice versa. In this way new models are created randomly. Mutation is performed in two ways, single and multi-point mutation. Single-point mutation means that only one bit in the whole model (or string) is reversed. Multi-point mutation means that for each parameter in the model a mutation bit is selected and reversed. The mutation of a bit takes place with the probability P_m.

The mutation cannot be 'decoupled' from the crossover. If single-point crossover is used only the combination of parameters in the models are changed, not the parameter values themselves. Changing the parameter values is needed to 'randomly' sample large parts of the model space. Therefore, in a GA with single-point crossover, mutation is necessary and a higher P_m is needed. When multi-point crossover is used, parameter values can be changed by crossover and a lower mutation rate (P_m) can be used.

In the single-point mutation a P_m between 0.1 and 1.0 was used. $P_m = 1$ means that in each string one random bit is changed. If this is an insignificant bit, mutation will have almost no effect on the fitness of the model. When a significant bit is changed the fitness can be changed significantly by mutation. $P_m = 0.5$ means that on average in 50% of the models one bit is changed.

Sambridge and Drijkoningen (1992) describe the mutation step as: "A mutation probability denoted by P_m is used to control the likelihood of an

individual bit in the model being altered in polarity". Stoffa and Sen (1991) and Sen and Stoffa (1992) use mutation as the random change of one bit in the model parameter code with probability P_m. Wilson and Vasudevan (1991) use mutation for each parameter in the model.

The mutation probability (P_m) is often set to a small value, $1/N$ or smaller, where N represents the number of bits in the model (string). As Gallagher et al. (1992) remarks, $P_m = 1/N$ indicates that on average one bit per string (or model) is changed. It must be kept in mind that P_m and P_c only represent the probability values for crossover and mutation. The actual percentages for crossover and mutation can differ from these probabilities, especially for small populations and a small number of generations in the GA.

4.2.6 *Generation Selection*

In the generation selection stage it is decided which models, from the parent and the child models, will form the next generation. Most authors do not mention this step but say they use an update parameter to decide which models go to the new generation. The generation selection procedure also partially controls the convergence in the GA. Two of these procedures are tested here.

The first procedure selects the best models from the parent and child population. After a child population is created we have $2N$ models, N parent models and N child models. These $2N$ models are sorted according to their fitness, then the first N models are selected to form the new generation. The better models will dominate the GA, but not one individual model since each model is only copied once into the new generation. This method is called the Best of All (BOA) method.

The second method allows more diversity in the population. In this method the parent and the child models are sorted according to their fitness separately. The fittest parent model is compared to the fittest child model and the fitter of the two goes to the new generation. Then the second fittest parent and child models are compared, and so forth. This method guarantees that the fittest model will always enter the new generation and that the poorest model (in terms of fitness) will never enter the new generation. This second method, called Best of Two (BO2), gives more diversity in the population of a generation at the cost of a slower convergence.

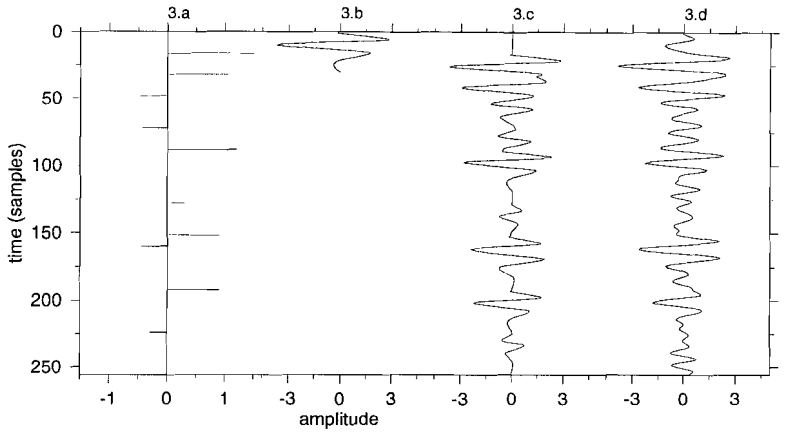

Figure 3. Forward model; Reflectivity trace (input model) (3.a), the input wavelet (3.b), the noise-free input data (3.c) and the noisy input data (3.d).

4.3 *Inversion of Synthetic Data*

The model used to construct the synthetic data is shown in figure 3.a. It consists of ten reflectors with reflector positions (sample number) and reflection amplitude as model parameters. The reflectivity trace, shown in figure 3.a, is convolved with the wavelet shown in figure 3.b to produce the noise-free data trace shown in figure 3.c. The signal to noise ratio is defined as

$$S/N = \frac{\max|signal|}{\max|noise|} \qquad [4.6]$$

Random noise, in the same frequency band as the data, was added to the data which resulted in the noisy ($S/N = 4$) data trace shown in figure 3.d. The initial population used for the GA inversion consists of 40 models. The models contain 10 reflectors with 5 bits for position and 7 bits for amplitude information. The trace is 256 samples long so the position resolution is 8 samples which is a quarter of the wavelength of the wavelet. The amplitude varies between -1.28 and $+1.28$. With 7 bits for amplitude information this results in a resolution of 0.02. In total the bit string of the model is $10 \cdot (5+7) = 120$ bits long, resulting in $2^{120} \approx 1.3 \cdot 10^{36}$ possible models.

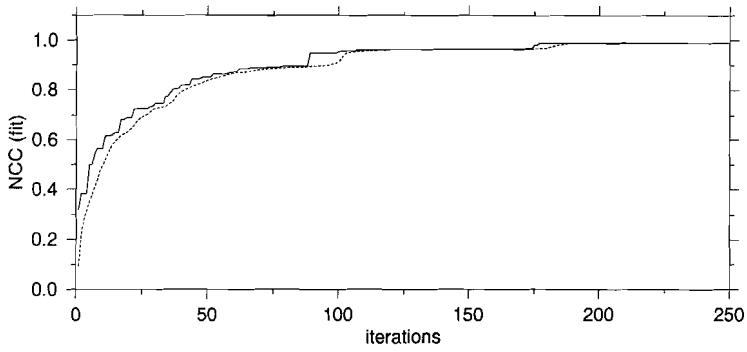

Figure 4. The fitness (NCC) as a function of the number of iterations. The solid line represents the highest fitness in the population, the dashed line indicates the average fitness of all models in the population. The inversion was done with a starting population of 40 models, $P_m = 0.5$, $P_c = 0.5$, RW parent selection, BOA generation selection, single-point crossover and mutation, 5 bits for position information and 7 bits for amplitude information.

4.3.1 *noise-free Data*

Figure 4 shows the fitness (NCC) of the best model in the population (solid line) and the average fitness of all models in the population (dashed line) versus the number of iterations. The model with the highest fitness, 0.972, after 100 iterations is plotted in figure 5.b and the input model in figure 5.a. Figure 5.c shows the input data (solid line) and the modeled data (dashed line). In this example single-point crossover and mutation were used with $P_c = 0.5$ and $P_m = 0.5$. The *NCC* was used as fitness function together with the roulette wheel parent selection method and the 'best of all' generation selection method.

Figure 5 shows that the reflectors at samples 128 and 224 are not resolved well. In the data (figure 5.c) this can be seen between samples 125 to 150 and between samples 225 and 250. On other parts of the data the amplitude is slightly wrong, especially for the reflector at sample 88.

The *SQE* fitness function gives results comparable (in terms of data fit and model fit) to the results of the *NCC* fitness function. In this chapter plots for the *NCC* fitness function are shown.

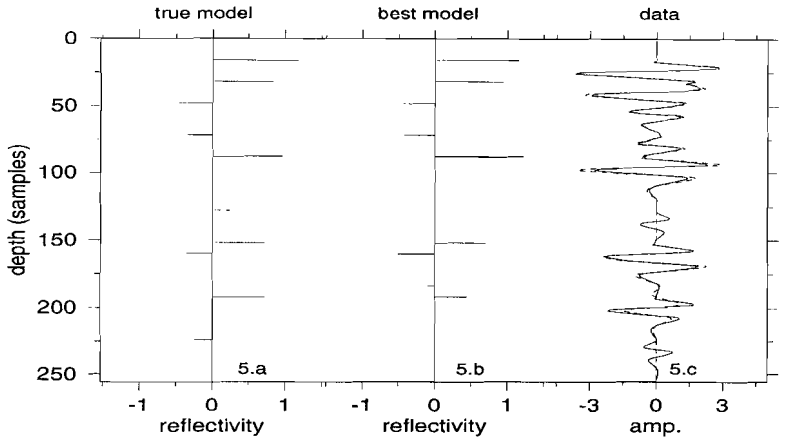

Figure 5. Result for GA inversion of noise-free data. (5.a) the true model, (5.b) the best model (fitness 0.972) after 100 iterations and (5.c) the input data (solid line) and the modeled data (dashed line). The inversion was done with a starting population of 40 models, $P_m = 0.5$, $P_c = 0.5$, RW parent selection, BOA generation selection, single-point crossover and mutation, 5 bits for position information and 7 bits for amplitude information.

Before applying the GA inversion it is difficult to say which values are appropriate values for the control parameters (e.g. Sambridge and Drijkoningen, 1992, Nolte and Frazer, 1994). Figure 6 shows the fitness (*NCC*) of the best model in the population as function of the values of P_c and P_m after 100 iterations with 40 starting models. A dark color means a high fitness and a light color means a low fitness. The values for the fitness were calculated for single-point crossover, single-point mutation, with BOA generation selection and RW parent selection. It is shown in figure 6 that the fitness depends on the choice for P_c and P_m, the best fitness (*NCC*) value is obtained for $P_c = 0.5$ and $P_m = 0.5$.

The fitness (*NCC*) of the best model after 100 iterations with 40 starting models for other combinations of parent selection and generation selection is shown in figure 7. Again the fitness (*NCC*) depends on the values for P_c and P_m.

Figure 8 shows the fitness (*NCC*) after 100 iterations with 40 models for single-point and multi-point crossover and mutation with the BOA generation selection and the RW parent selection. The plots for single-point and multi-point

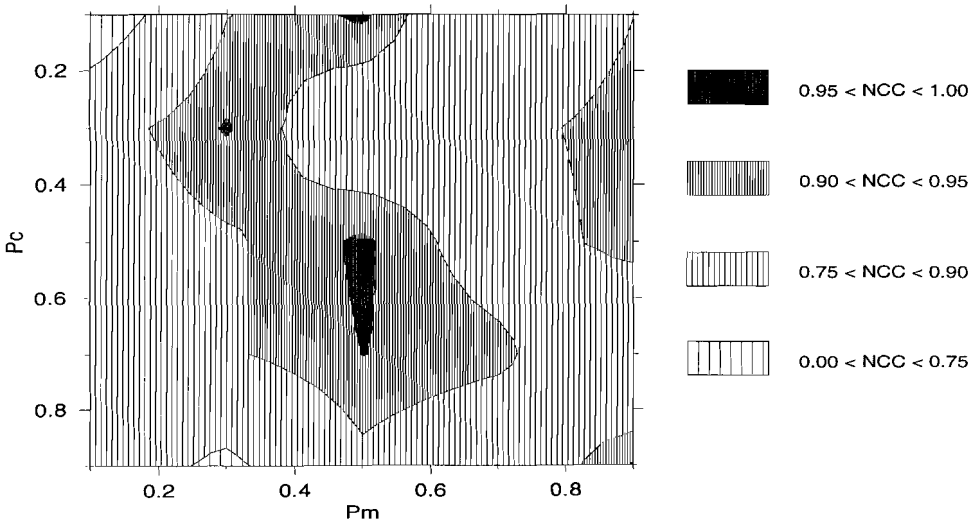

Figure 6. The fitness (NCC) for noise free data as a function of P_m and P_c after 100 iteration. The inversion was done with a starting population of 40 models, RW parent selection, BOA generation selection, 5 bits for position information and 7 bits for amplitude information.

crossover and mutation for other combinations of parent and generation selection are very similar. In general the combination of single-point crossover and single point mutation gives the best results. The best result are obtained for $P_m > 0.5$. For P_c we cannot make such a general statement.

Figures 6, 7 and 8 show that the values for P_c and P_m, for which the highest fitness values are obtained, depend on the other input parameters like the parent and generation selection method, single or multi-point crossover and mutation. The number of iterations, the number of starting models, the number of reflectors, the number of bits per parameter and the fitness function also influence the best values for P_c and P_m.

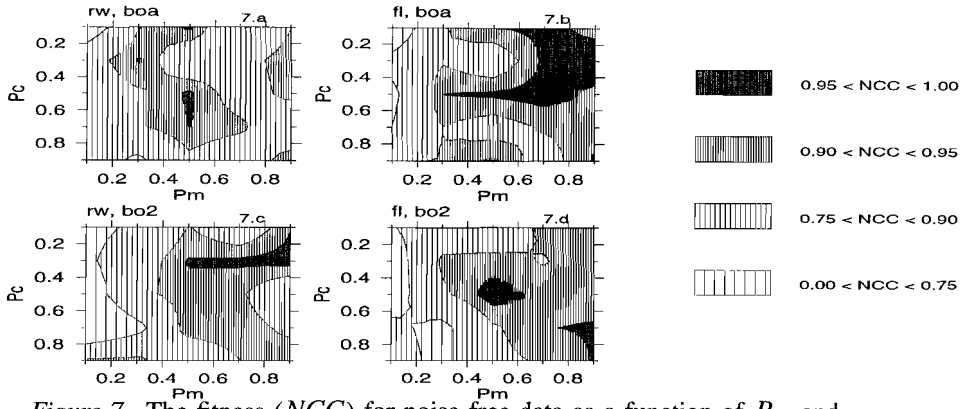

Figure 7. The fitness (NCC) for noise free data as a function of P_m and P_c for several combinations of parent selection and generation selection. (7.a) RW and BOA combined, (7.b) FL and BOA combined, (7.c) RW and BO2 combined, (7.d) FL and BO2 combined. 100 iterations were done with a starting population of 40 models, single-point crossover and mutation, 5 bits for position information and 7 bits for amplitude information.

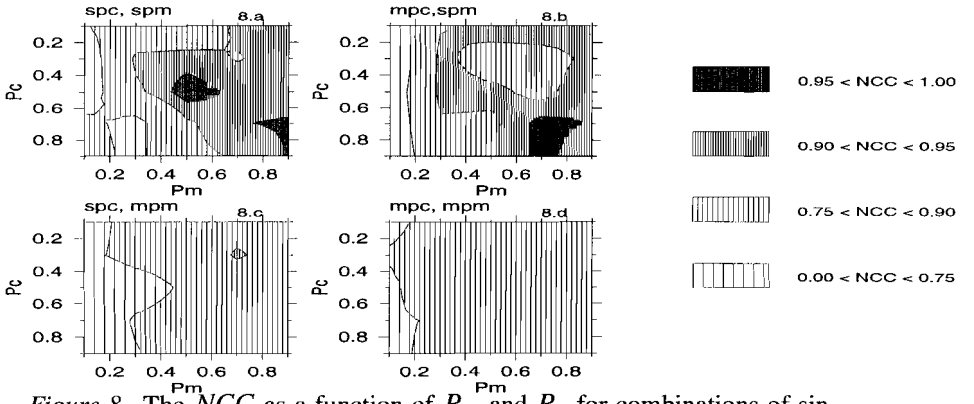

Figure 8. The NCC as a function of P_m and P_c for combinations of single and multi-point crossover (spc and mpc) and single and multi-point mutation (spm and mpm). (8.a) spc and spm combined, (8.b) mpc and spm combined, (8.c) spc and mpm combined, (8.d) mpc and mpm combined, RW parent selection and BOA generation selection were used. Other inversion parameters were as in figure 7.

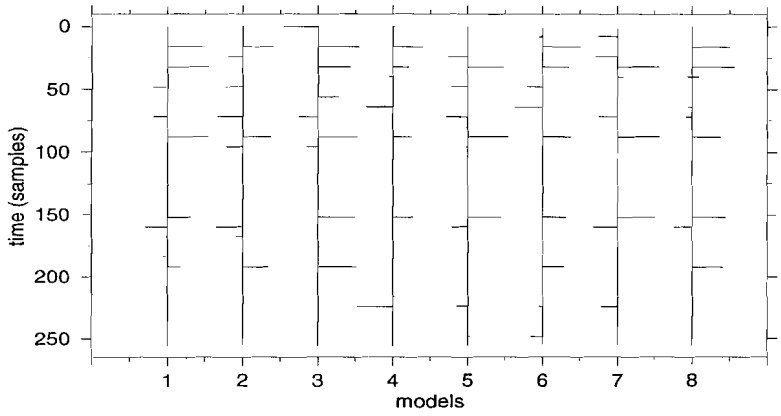

Figure 9. The results (best models) after inversion of noise-free data (4000 models tested) for eight different combinations of control parameters during the inversion.

4.3.2 *Combining Models*

Figure 9 shows the best models from eight GA inversions with various settings for the control parameters and 4000 models tested. A large diversity in 'best models' exists. It is clear from this figure that the final solution of the GA inversion is biased by the setting of the control parameters and not simply the 'best model' can be used. It is proposed to combine the 'best models' from several GA runs to one combined model. This is done by giving each position (sample number) a score and the R samples with the highest score are assumed to represent a reflector, where R is the (chosen) number of reflectors in the final model. The score (SC) for a sample is defined as:

$$SC_i = \sum_{m=0}^{m=N-1} |a_{im} \cdot f_m| \qquad [4.7]$$

where i is the sample number, N is the number of models, a_{im} the amplitude of sample i of model m and f_m is the fitness of model m. When a reflector position is mentioned in many models the score will become higher for this position. Models with a poor fit will contribute less to the score of the reflector at this position. The score gives an indication of how well resolved a certain part of the model is.

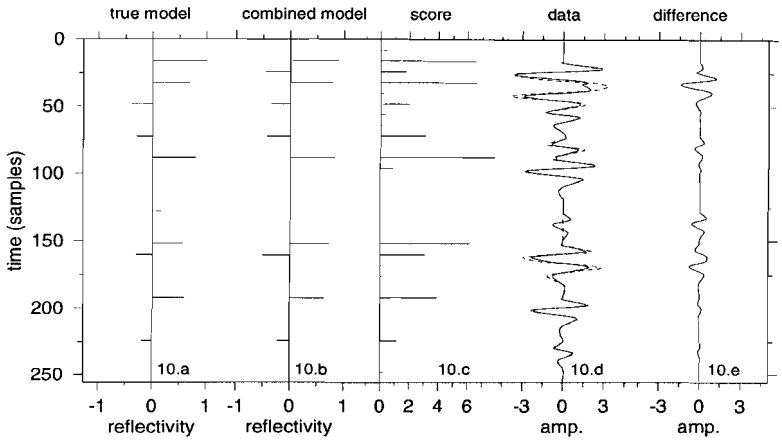

Figure 10. The results for noise-free data after combing the 8 models shown in figure 9. (10.a) The true input model, (10.b) the combined model, (10.c) the score of the samples in the combined model, (10.d) the input data (solid line) and the modeled data (dashed line) and (10.e) the difference between input data and modeled data.

The amplitudes of the 'chosen' reflectors are a weighted average of all amplitudes for that position;

$$A_i = \frac{\sum_{m=0}^{m=N-1} |a_{im} \cdot f_m|}{\sum_{m=0}^{m=N-1} f_{m_i}} \qquad [4.8]$$

where A_i is the amplitude in the combined model and f_{m_i} is the fitness of model m if position i is mentioned as a reflector position, otherwise it is zero. The input (true) model and the combined model are plotted in figure 10.a and 10.b. The score for all possible reflector positions is shown in figure 10.c. The input data and the modeled data from the combined model are shown in figure 10.d. Figure 10.e shows the difference between the input data and the modeled data. The largest difference occurs around sample 35 due to a reflector at sample 24 in the combined model, where there is no reflector in the 'true' model. The fitness in the combined

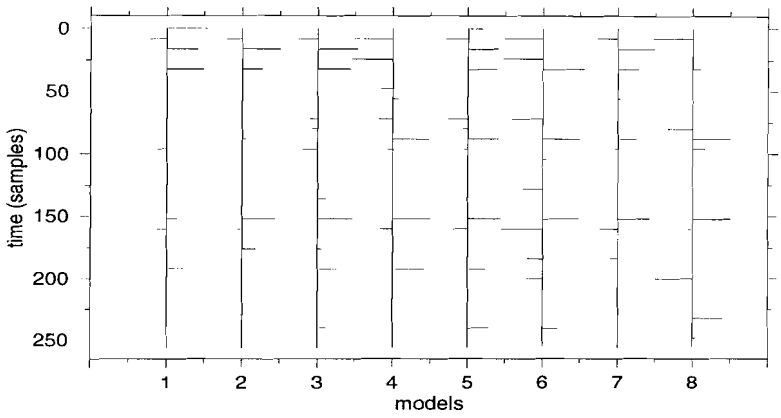

Figure 11. The results (best models) after inversion of noisy data (4000 models tested) for eight different combinations of control parameters during the inversion.

model is 0.962, about equal to the fitness of the best model shown in figure 5. In the combined model the reflector at sample 224 is found (which was not present in figure 5.b). Also a new reflector at sample 24 is introduced. Combining models reduces the bias due to parameter settings.

4.3.3 *Noisy Data*

Figure 12.d shows the noisy input trace as a solid line. The result of inverting the noisy data also depends on the settings of the control parameters. Therefore, eight runs with different settings for the control parameters were done and the models from these inversions were combined as described in section 4.3.2. Figure 11 shows the best models from the eight inversions. In figure 12.a the true model and in figure 12.b the combined model is plotted. The scores for all samples of the combined model are plotted in figure 12.c. The inverted data (dashed line) and the input data (solid line) are plotted in figure 12.d. The difference between the input data and the modeled data is plotted in figure 12.e. The fitness for the 'true' input model is 0.856, higher fitness values will be due to the fitting of noise. The fitness of the combined model is 0.849.

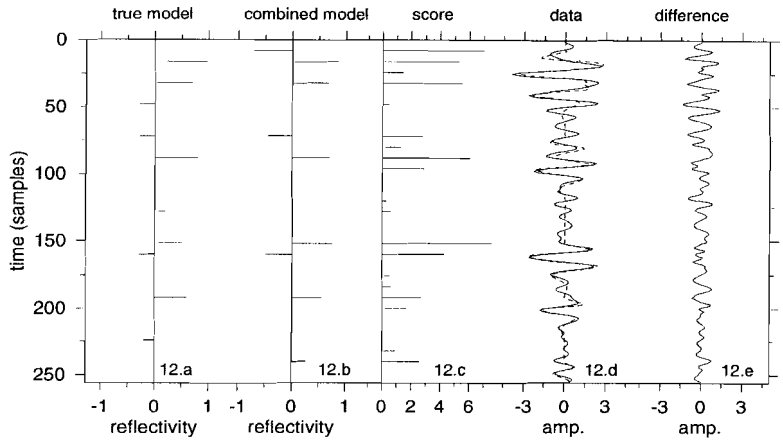

Figure 12. The results for noisy data after combing the 8 models shown in figure 11. (12.a) The true input model, (12.b) the combined model, (12.c) the score of the samples in the combined model, (12.d) the input data (solid line) and the modeled data (dashed line) and (12.e) the difference between input data and modeled data.

The small amplitude signals (from reflector 128 and 224) are lost in the noise and the GA inversion does not find the corresponding reflectors. Due to the noise some reflectors are placed at the wrong position (e.g. sample 8 and 240). In figure 11 model 6, the reflector at sample 192 is modeled by two negative amplitudes at samples 184 and 200. As a result of combining the models in figure 11 the combined model shows this reflector as a positive amplitude at the correct position.

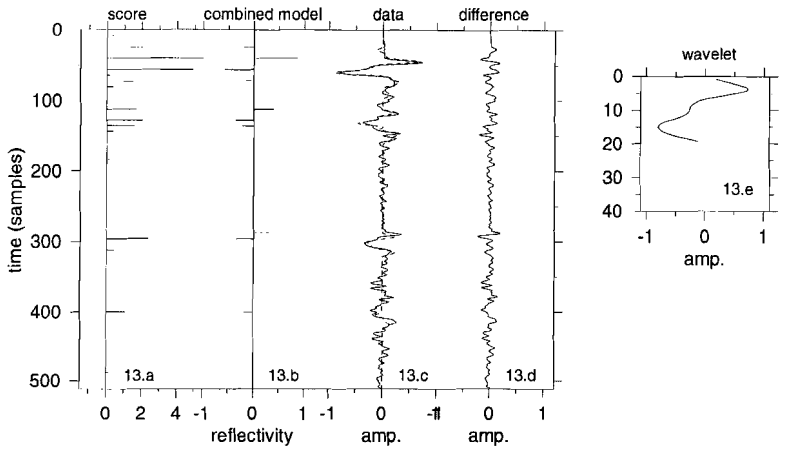

Figure 13. Results of inversion of real data. (13.a) The score of the samples in the combined model, (13.b) the combined model, (13.c) the input data (solid line) and the modeled data, (13.d) the difference between the real data and the modeled data and (13.e) the wavelet used for inversion.

4.4 *Inversion of Real Data*

Figure 13 shows the result of inversion of a real trace. The score for each sample is plotted in figure 13.a. The combined model consists of the 10 reflectors with the highest score and is shown in figure 13.b. The difference between the modeled data (figure 13.c, dashed line) and the real data (figure 13.c, solid line) is shown in figure 13.d. The wavelet used for the inversion is shown in figure 13.e. This wavelet is taken from the real data trace and corresponds to samples 43 to 67. The misfit around samples 50 and 300 is partly due to the resolution used for the position of the reflectors (the reflectors were placed at multiples of 8 samples). When the 'true' reflector falls in between two possible modeled reflector positions, the difference in amplitude between the input data and the modeled data can be large. The reflector at sample 24 must be wrong because no signal arrives at this time. The one reflector at sample 400 is not enough to fit the data around this sample.

4.5 *Conclusions*

The result of the GA inversion has been shown to depend on the settings of the control parameters. It is suggested to run the inversion several times with different settings for the control parameters and combine the resulting models to one so-called 'combined model'. The models are combined in such a way that better (fitter) models and reflectors with a high amplitude contribute more to the 'combined model' than poor models and low amplitude reflectors. Comparison between the noisy and noise-free data shows that the GA inversion with combining models is robust and relatively insensitive to noise in the data. In the work presented here it was assumed that the wavelet was known. The next step to implement in the GA inversion is the simultaneous extraction of the wavelet. This can be done by adding extra parameters to the model which describe the wavelet.

Chapter 5

Case study 1 : The North Sea[1]

5.1 *Introduction*

In this chapter a North Sea case study is described. The objective of this study was to acquire high resolution seismic data in order to provide insight into the evolution and establishment of the Holocene transgressive sequence along the Dutch barrier island chain. The relationship between this sequence and correlative counterparts in the North Sea will be studied.

This chapter is divided into three parts; acquisition, processing and interpretation. The first part describes the acquisition methods and field conditions during the measurement periods. In the second part the processing steps and corrections which were applied to the data are explained. The last part gives a brief overview of the geologic history of the survey area and presents an interpretation of the processed seismic data.

5.2 *Acquisition*

In 1989, 1990, 1991 and 1992 seismic data were collected in the survey area. All recorded lines are shown in figure 1. The tracks ranged from 10 m water depth to about 35 m water depth, targeting most of the transgressive Holocene sequence (see section 5.4.1). In total, about 1200 km of seismic profiles were recorded.

---

1 Parts of section 5.4 are based on: Kosters, E.C., Van Mierlo, B.J.E.M., Verbeek, N.H., Posthumus, B.J., McGee, T.M. and Brouwer, J., Late Quarternary Stratigraphic Signature, Offshore from the Dutch Barrier Shoreline. Sedimentary Geology, 80, 199-212, 1992.

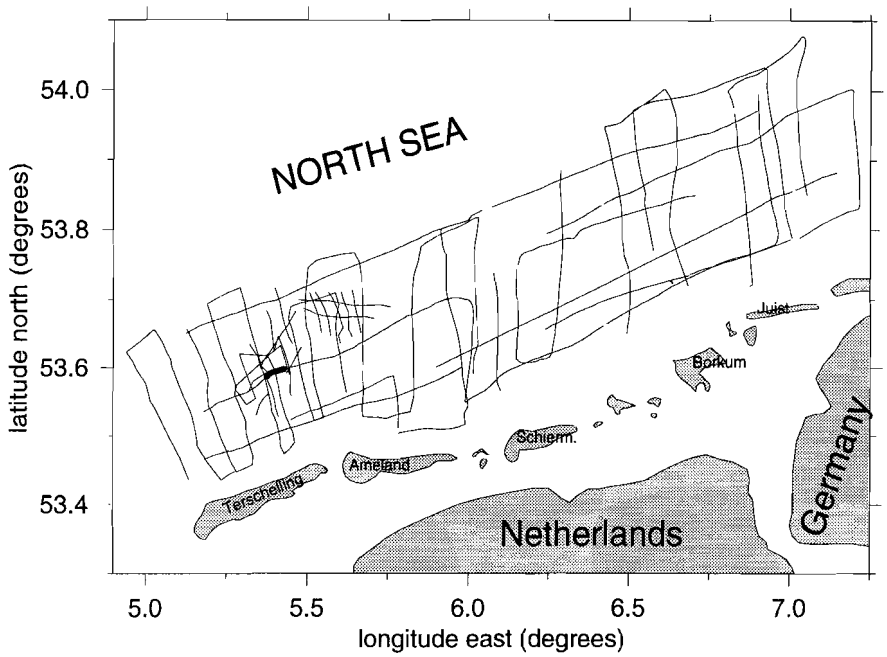

Figure 1. Map of the survey area. The track lines are shown. The thick line is the line used as example in the processing section.

For this survey the available ship-time was limited to a few weeks in the autumn and had to be planned more than a year in advance. The weather conditions during this survey were not good, so the data are quite noisy.

To obtain detailed information about the sediment structure, boxcores and vibracores were taken in 1989. About 50 boxcores were collected which led to details of sediment dynamics across the sand ridges (sections 5.4.4). Vibracoring parts of the sequence has failed. Fluidization took place during the coring, probably due to the uniform grain size of the sediment.

5.2.1 *Research Vessels*

The research vessel (RV) used in 1989 and 1990 was the "Aurelia" of the Netherlands Institute for Sea Research (NIOZ). The RV Aurelia is about 30 m long and 8 m wide. In 1991 the RV Aurelia was replaced by the RV Pelagia which was used in 1991 and 1992. The RV Pelagia is about 65 m long and 11 m wide. The draft of the RV Pelagia is about 6 m. For reasons of safety the ship did not enter waters shallower than 10 m. During the acquisition the average speed of the vessels was about 3 to 4 knots (1.5 to 2 m/s) for all surveys.

5.2.2 *Seismic Sources*

It was planned to do the entire survey of the North Sea area with a boomer type seismic source because it gives high resolution results. In chapter 2 it is shown that the high resolution potential is due to the high dominant frequency and large bandwidth of the boomer. The boomer was mounted in a small catamaran and towed close to the water surface, about 25 m behind the ship. The shot rate was about 1 shot per second. In 1989 and 1992 an EG&G boomer was used, in 1990 and 1991 an ORE-Tech boomer. They were operated at energy levels of 300 and 350 Joule, respectively. At these energy levels the dominant frequencies are about 6 kHz, giving a wavelength of about 0.25 m (1500 m/s / 6000 Hz). Due to the poor weather conditions during the surveys (strong wind, large wave action) only a small amount of the data was shot with the boomer. In 1992 there were also some technical problems with the boomer which made it impossible use the boomer during the periods with better weather.

Most of the time the airgun was used as seismic source because of the large wave motion. The airgun has a spherical directivity (see chapter 2) and the waveform is not much influenced by changes in the "direction" of the gun due to wave action. However, as a result of the wave motion, the gun was not always at the same depth below the water surface which decreased the repeatability of the signal. Part of the time the airgun was towed in a frame built of two surfboards, with the gun at about 20 cm below the surface. At other times the airgun was towed attached to a buoy with the gun about 35 cm below the water surface. Towing the airgun close to the surface has the effect that most of the bubble pulse is suppressed (see section 1.2.2.1). The data from the surfboard construction showed less bubble pulses than the data from the buoy construction. The airguns were

"Bolt" airguns with volumes of 5, 10 and 25 in^3. The pressure was about 100 bar. Sometimes it was difficult to keep the pressure on the airgun constant. This also influenced the waveform of the emitted signal. Most of the data were recorded with the 10 in^3 airgun which has a dominant frequency of 500 Hz, i.e., the wavelength of the signal is around 3 m (1500 m/s / 500 Hz), more than 10 times larger than the wavelength of the boomer. The shot rate of the airgun was one shot every 5 seconds, corresponding to a shot interval between 7.5 m and 10 m.

5.2.3 *Receivers*

The data were received by a streamer with a total active length of 2 m comprising 30 hydrophones with a hydrophone spacing of 7 cm. This streamer is divided into three groups of 120, 20, and 50 cm length with 18, 4 and 8 hydrophones respectively. Within each group the hydrophones are connected in parallel. The groups can be recorded separately or be summed. This allows the active length to be varied with water depth (see also section 1.4). The deeper the water, the longer the active length used. The streamer was towed about 25 m behind the ship parallel to the source. The source/receiver offset was about 2.5 m.

5.2.4 *Recording Equipment*

In 1989 the data were recorded in analogue format on an electro-static plotter (EPC recorder). In the other years data were recorded in both digital and analogue format. The MDAS system (section 1.5 and Posthumus, 1991) was used for the digital recording of the data. With each shot also the date and the time were recorded. The boomer data were digitized at 50 kHz after a bandpass filter of 250 Hz to 10 kHz with 18 dB per octave slope. The airgun data were partly digitized at 20 kHz and partly at 12 kHz after a bandpass filter of 100 Hz to 5 kHz and 100 Hz to 3 kHz respectively, both filters with 18 dB per octave slope. Recording time was 150 ms for all data. In general, almost no penetration deeper than 25 ms below the sea bottom was obtained. Given a maximum sea depth of 30 m in the survey area, the penetration was about 48 m below NAP (assuming a sound speed of 1500 m/s).

5.2.5 *Positioning*

In 1989 and 1990 the position was determined with help of a DECCA Navigator MK21 system. This system has an accuracy of about 50 m. Every ten minutes a position was taken from the DECCA system and logged with the shot number, time and date. For the intermediate shots the positions were obtained by linear interpolation. In 1991 the MDAS acquisition system was updated with a Differential Global Positioning System (DGPS). This navigation system gives a resolution between 2 m and 20 m. At each shot the position was obtained from the DGPS and digitally stored together with the data. In 1991 the resolution of the DGPS was better than 5 m because the US army used civil GPS systems during the Gulf War. They switched off the scrambling code to obtain highest possible resolution with the civil GPS systems. In 1992 the resolution was again between 2 m and 20 m.

5.2.6 *Noise*

The acquired data are of poor quality due to high noise levels. The noise was caused by several factors:

1) The streamer and source bounced against each other due to wind and wave action; this saturated the amplifier.
2) Wind and wave action combined with the short towing distance caused the streamer to rise partly above the water.
3) Some frequency filters produced electrical noise.
4) The approximately 20 m of cable remaining on the deck of the ship picked up inductive noise.
5) The noise from the propulsion of the ship was kept low by going slowly. Increasing the ship's speed increased the noise.
6) Wind direction. The quality of the data was better with the wind on the beam rather than from behind or from the front.

5.3 *Processing*

Analogue data were not fully processed, but only time corrected. The reflectors were marked on the EPC records and the reflection times were digitized. The reflection times were corrected for delay time of the airgun, the source/receiver offset and the tide.

The digitally recorded data were processed further before interpretation. In this section the processing sequence applied to the data is described using one example. The example line is part of line 91-44-1 (shots 1500 to 2000), the position of which is shown in figure 1 and figure 6. The first step in the processing was DC-offset removal, after which the data were band-pass filtered. After the filtering the arrival times of the direct wave, bottom reflection and first multiple of the bottom reflection were measured and the bottom was flattened. The next step was trace mixing (stacking of several shots) after which the reflector times were picked. The picked reflector times are relative to the time of the flattened bottom. Before a geological interpretation can be made, the reflectors that have been picked have to be placed at their "true" depths (times). The picked reflector times must be corrected for the mechanical delay time of the airgun, the source/receiver offset and the tide. After these corrections the reflectors are at the correct depth and a geological interpretation can be made.

5.3.1 *DC-offset removal*

The acquisition system added a small DC-offset to the data. This offset can obscure the data, depending on the display type. The offset was about -0.1 V, where the amplitude of the data ranges from -5 V to +5 V. The DC-offset is removed by calculating the average (mean) amplitude of the data trace. Subsequently, this value is subtracted from all data samples in that trace. Figure 2.a shows the data of the example line after DC-offset removal.

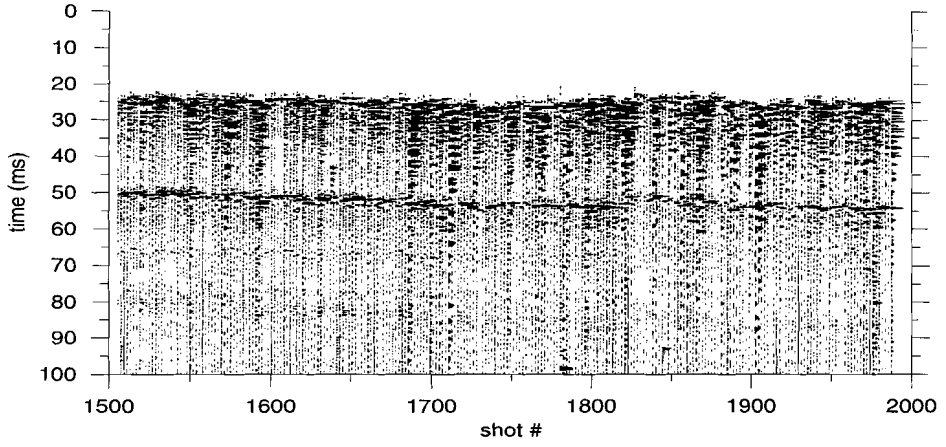

Figure 2.a. Data after DC-offset removal. Part of line 91-44-1 (shots 1500 to 2000) as indicated on figures 1 and 6.

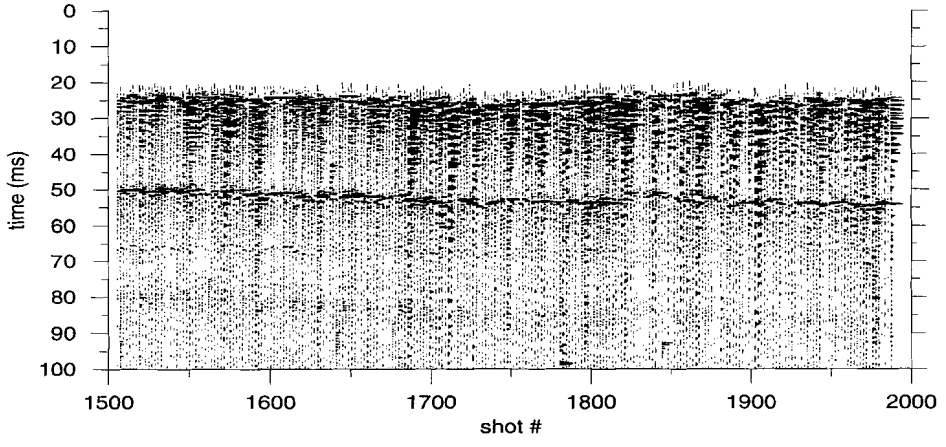

Figure 2.b. Data after frequency filtering. Shots 1500 to 20000 of line 91-44-1.

5.3.2 *Frequency Filtering*

From source signature measurements (Chapter 2) the frequency content of the airgun and boomer source wavelets is approximately known. The airguns have a dominant frequency around 500 Hz and the bandwidth (30 dB below peak power) is about 3,500 Hz. The boomer has a dominant frequency around 6,000 Hz and a bandwidth (30 dB below peak power) of about 20,000 Hz. Analyzing the data in the frequency domain indicated noise bands for some shots, which may be related to the towing mechanism of the sources. Other types of noise are described in section 1.7 and section 5.2.6. Based on these analyses zero-phase bandpass filters were selected. For the airgun data the filter was: 150-300 / 2,500-3,000 Hz and for the boomer data it was: 1,500-2,000 / 7,500-10,000 Hz. The data after frequency filtering are plotted in figure 2.b.

5.3.3 *Bottom Flattening*

The bottom seems very rough on the example line (and also on other lines). This was caused by the strong wave action during the acquisition. The same wave action also caused the reflectors not to line up nicely. In this processing step the arrival time of the bottom reflection is picked first, after which the bottom is flattened to a specific level (44 ms). This means that each trace is time shifted such that the bottom reflection for all traces arrives at the same time. The deeper reflections become more visible because the scattering in arrival times of the reflected waves, due to wave action, is decreased. Also, differences in arrival time due to other sources (e.g. offset and delay time variations) are decreased. In the bottom flattening procedure the direct wave is muted. Figure 2.c shows the flattened data.

5.3.4 *Trace Mixing*

The next processing step applied to the data was trace mixing, or horizontal stacking, of several shots. The stack was a weighed stack over five traces with weights 0.1, 0.2, 0.4, 0.2, 0.1, where the middle trace is the position of the stack. The traces were horizontally stacked which means that no time shift was allowed between the traces during the stack. In this way horizontal and slightly dipping reflectors are enhanced. Dipping reflectors add destructively and become less clear.

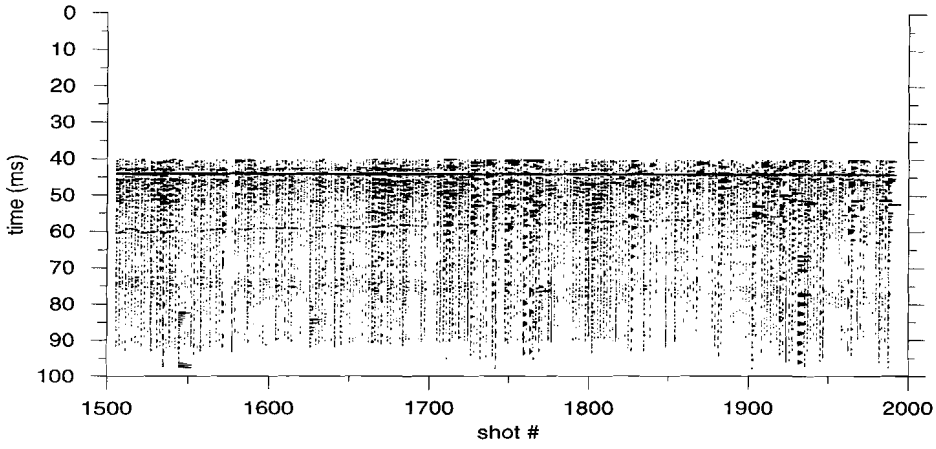

Figure 2.c. Data after bottom flattening. Shots 1500 to 2000 of line 91-44-1.

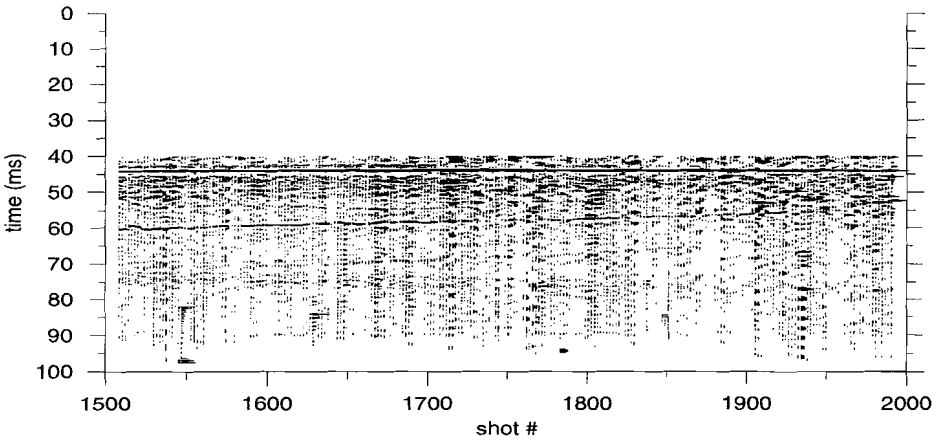

Figure 2.d. Data after trace mixing. Shots 1500 to 2000 of line 91-44-1.

Signals add constructively when they are not more than a quarter wavelength out of phase. Assuming a wavelength of 0.25 m (dominant frequency 6000 Hz) for the boomer source and a shot interval of 2 m, the steepest dip at which a reflector will add constructively is about 1°. Given that the data are flattened, this dip is relative to the bottom dip. For the airgun data, with a wavelength of 3 m and a shot interval of 10 m, the corresponding dip is about 2°. Reflectors at an angle to the bottom larger than these values are out of phase and add destructively, they will be suppressed in the trace mixing procedure. Noise in different shots is also suppressed. Figure 2.d shows the stacked data.

5.3.5 *Time corrections*

At this stage in the processing the signal-to-noise ratio is improved, using frequency filtering and trace mixing. Differences in depth due to wave height, different delay times of the gun, tidal variations in water depth, etc. have been removed from the data by bottom flattening. This results in reflectors 'tying' well at line intersections. From the processed data the reflector times are picked.

The bottom was flattened to a time level of 44 ms. The reflector times picked have to be corrected to place the reflectors at their 'true' arrival time (zero-offset two-way-travel-time). The 'true' arrival time of the bottom reflection is the measured arrival time of the bottom reflection corrected for the trigger delay time, the offset, tidal variations and wave height. When the recording system is triggered at the moment the gun fires, e.g. by placing a hydrophone on the gun and using its signal as a trigger, there is no trigger delay time. In this study one trigger was used to trigger both the gun and the recording system at the same time, so there was a trigger delay time. The 'true' arrival times for each shot are calculated as described below. Next, all the arrival times of the reflectors of that shot are shifted by the time difference between the 'true' arrival time of the bottom and the flattened arrival time of the bottom (here 44 ms).

The recording system and the source were triggered by the same trigger pulse. For the boomer sources this presented no problem. For the airgun, on the other hand, there was a mechanical delay time between the trigger and the actual firing of the gun. The delay time was not measured and must be calculated. This can be done with the help of the arrival times of the direct wave (*dw*), the bottom reflection (*br*) and the arrival time of the first water-bottom multiple (*mp*). These arrival times are given by :

$$dw = ot + dt \qquad [5.1.a]$$

$$br = \sqrt{ot^2 + 4wt^2} + dt \qquad [5.1.b]$$

$$mp = \sqrt{ot^2 + 16wt^2} + dt \qquad [5.1.c]$$

This can be rewritten as :

$$dt = \frac{4br^2 - mp^2 - 3dw^2}{8br - 2mp - 6dw} \qquad [5.2.a]$$

$$ot = dw - dt \qquad [5.2.b]$$

$$wt = 0.5\sqrt{(br - dt)^2 - ot^2} \qquad [5.2.c]$$

where *ot* is the offset time, *wt* is the 'water time' and *dt* is the delay time of the gun. The offset time (*ot*) is given by the offset between source and receiver divided by the sound speed in water. The 'water time' (*wt*) is the 'zero offset' two-way-travel-time of the bottom reflection.

The data are first corrected for the delay time (*dt*). The delay time is calculated for every shot and then averaged over all shots in that line. The delay time changes as the gun pressure changes. When the gun pressure changed, a running average over several shots was used. The amplitude of the first water-bottom multiple is of the same order as the amplitude of the noise in most of the airgun data. Incorrect picks for the water-bottom multiple arrival times can cause false values for the calculated delay times, offsets and depths (e.g. negative values for one of these). To calculate the average delay time only "normal" values are used. Normal values exist if the delay time, offset and water depth are within certain intervals. The boundaries of the intervals are 12 ms and 24 ms for the delay time, 0 m and 10 m for the offset and 5 m and 50 m for the water depth.

When the delay time is known, the 'true' depth can be calculated from the arrival times of the direct wave and the first reflection from the bottom. Their signals are normally very clear and the arrival times can be picked without problems. From these arrival times the 'zero offset' two-way-travel-time for the bottom reflection is calculated. The time difference between the calculated and the measured arrival time of the bottom reflection is used as offset correction. The offset-correction is only correct for the arrival time of the bottom; deeper reflections are somewhat over-corrected.

The next time-correction is a kind of swell filter, which corrects for differences in water depth due to wave action. The arrival times of the bottom reflections were computed as the average arrival time over 5 shots, where the middle shot was the shot for which the arrival time of the bottom reflection was calculated. In this way the rapid variations in arrival times between shots, due to wave height, are suppressed.

Before the geological interpretation can be made the reflector times must also be corrected for variations in water depth as a result of the tide. In the survey area the tidal variations are between plus and minus 1.7 m. Tidal measurements are made every ten minutes along the Dutch coast by Rijkswaterstaat. For each shot the time and position were measured or calculated. For each shot the tidal measurements and the time and position data are combined to estimate a correction for tidal variations in water depth. After this correction is made all data should be relative to NAP.

To check the validity of the sum of all the corrections applied to the data, the misfits at line intersections were computed. The general misfit on the intersection points is about 1.1 ms. The largest misfit is about 3 ms (about 2.25 m) which is still large but less than half of the misfit before corrections (6.5 ms).

5.4 *Interpretation*

In this part an overview of the (post) Saalian regional geologic history based on the literature is given[2]. After this overview the results of the seismic surveys will be discussed. The interpretation based on the seismic data will be compared with published interpretations. Parts of this section are based on Kosters et al. (1992).

5.4.1 *Regional Geologic History*

This overview starts with the Saale glaciation as this is the oldest geologic period that can be recognized in the data set. Four major periods can be

---

2 For a more detailed description of the geologic history of the survey area see, amongst others, Jelgersma 1979, Jelgersma, Oele and Wiggers 1979, Oele and Schüttenhelm 1979, Jansen et al. 1979, Eisma et al. 1981, Fitzgerald and Penland 1987, Franken 1987, Long et al. 1988, Streif 1989, VanAlphen and Damoiseaux 1989, Zagwijn 1989. Joon et al. 1990, Niessen 1990, Sha 1990, VanMierlo 1991, Kosters et al. 1992 and VanderSpek 1992,

distinguished; the Saalian glaciation, the Eemian interglacial, the Weichselian glaciation and the Holocene interglacial. The time scales of these periods are shown in figure 3.

During the maximum extent of the Saalian glaciation (180,000 - 150,000 years Before Present (BP)) the Scandinavian ice sheet covered large parts of the Netherlands. In this period ice-pushed hills, tongue shaped basins and lodgement tills occurred in the northern part of the Netherlands. The ice sheets generated the ice-pushed ridges near Nijmegen and Arnhem. Deep (up to 100 m below present sea level) glacial basins were formed in the Haarlem-Amsterdam area (see also Chapter 7). The thickness of the Saalian deposits varies considerably due to glaciotectonic processes and erosion during the following interglacial and glacial periods.

Phases of warming climate and marine transgression characterize the Eemian (150,000 - 115,000 BP). The Saalian depressions were filled with sediment during the Eemian. The top of the Eem deposits is found at about 13 m below NAP in the north-eastern part of the Netherlands. The thickness of the Eemian sediments, near the Dutch coast, varies from 2.5 m to 13 m. During the following glacial period the top of the Eemian sediments was extensively incised.

At the maximum of the Weichselian (115,000 - 10,000 BP) glacial period the sea level was 110 m lower than it is at present. There was no connection between the British and the Scandinavian ice sheet and the Dutch sector of the North Sea was not covered by ice. Weichselian deposits are present in extensive areas of the North Sea. The Holocene transgression reworked most of the Weichselian sediments, so that Weichselian facies are poorly preserved offshore. Rivers discharged in the central North Sea during the Weichselian period. Late Weichselian and early Holocene drainage systems did supply sediment to the German Bight.

The Holocene interglacial started 10,000 BP. In general the sea level rose rapidly from 110 m to 5 m below present sea level from 10,000 BP to 5,000 BP. Since 5,000 BP, the relative sea-level rise is thought to be caused mostly by subsidence of the North Sea basin. A climate change caused a rapid sea level rise during the first 2,000 years of the transgression. No connection between the Atlantic ocean and the North Sea through the Straits of Dover existed in the Weichselian. With the establishment of this connection (8,000 BP) a different tidal circulation pattern may have appeared in the North Sea. An increasing tidal range, in combination with a change in nature and volume of sediment supply, implies that preserved early- and mid-Holocene facies sequences should be different from

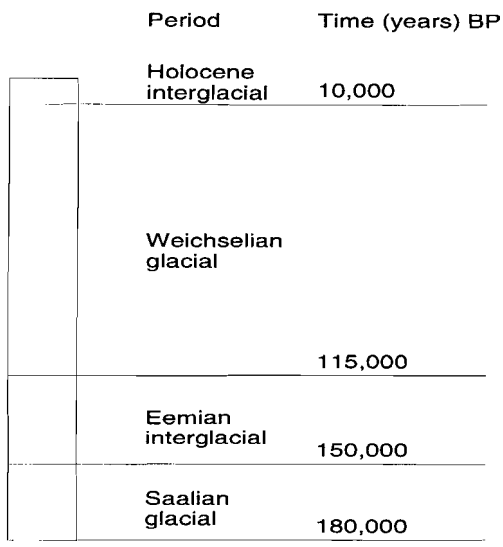

Figure 3. The geologic periods and time scale mentioned in the text.

those found presently. Around 7,500 BP the shoreline almost reached its present position. It is assumed that during this period the shelf ridges in front of the Dutch coast were formed. The formation of present day barrier islands started 8,000 years BP. Thick sequences of intertidal and subtidal deposits occur in the seaward part of the tidal flats. Offshore, the Holocene sediment wedge of the German Bight is characterized by a sand sheet, the thickness of which ranges from 0 to 30 m. The sea-floor is either relatively smooth (incorporating sand-waves) or contains sand ridges with a length of some tens of km, a width of several km and a height of a few meters.

The overall transgressive Holocene sequence is caused by a combination of eustatic sea-level rise, isostatic rebound with the retreat of the Weichselian ice sheet and subsidence of the North Sea.

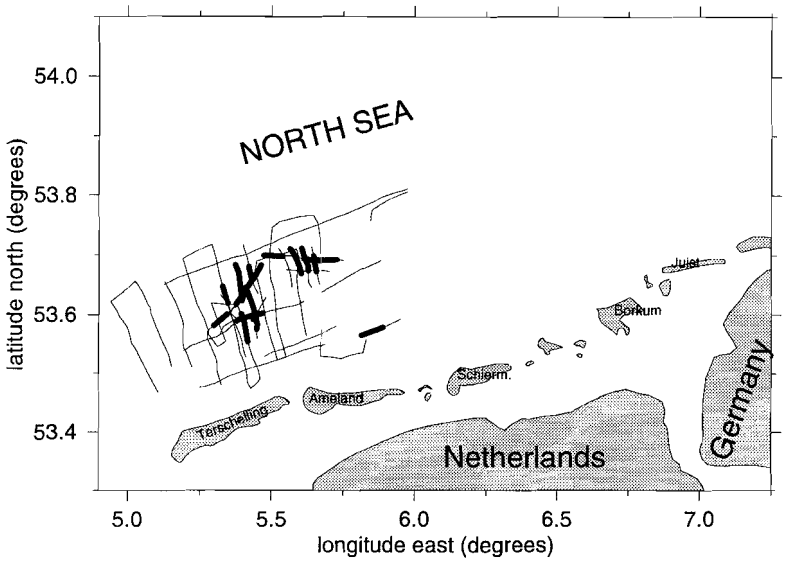

Figure 4. Location of the observed Saalian (thick lines) and Eemian reflectors (thin lines).

5.4.2 *Saalian Reflectors*

The lowermost event in the seismic data appears as a reflector with a pronounced relief on some lines. In figure 4 the locations where this reflector is observed are indicated by the thick lines. The relief of this reflector is shown in figures 7.b and 7.c and marked by arrow 1. The relief is probably caused by glacial deformation, which indicates a pre-Eemian age. Below Terschelling, Saalian glacial till is present below the Eemian marine deposits (Sha, 1990). Therefore, this reflector is interpreted as the top of a compact and dense Saalian till (Drenthe Formation). Its position (5.45° E, 53.60° N) is shown in figure 6 as a black square (e). The top of the Saalian till is about 28 m below NAP (42 ms two-way-travel-time, sound speed 1500 m/s). From the seismic lines collected in several directions the till appears to have a dome shape. The Saalian reflectors are only observed in the western part of the survey area (thick lines in figure 4), predominantly north of the till (see figure 6).

5.4.3 *Top Eemian Reflector*

A clear reflector is observed in the western part of the survey area. The depth of this reflector is between 35 to 55 ms, about 27 to 42 m below present sea level. Based on seismic and borehole data Niessen (1990) found a depth of 25 to 30 m for the Top Eemian deposits near the Dutch barrier islands. Sha (1990) found a depth of 28 to 32 m for the Top Eemian deposits, north of Terschelling between the 10 and 20 m water depth contours (see figure 5). The clear reflector is onlapping on the Saalian till, the onlap indicates a transgressive system. This reflector is interpreted as the top of the Eemian deposits. The relative flatness of this reflector can be caused by the flat deposition of marine sediments, leveling most of the Saalian relief. Subsequent subaerial erosion could have leveled the Top Eemian reflector. In some places this reflector shows incisions which indicate that there were drainage channels in the Weichselian glacial period. Figure 4 shows the extension of the Top Eemian reflector (thin lines). In the seismic data a sharp end to the (clear) Top Eemian reflector is observed at 5.9° E, between the barrier islands Ameland and Schiermonnikoog. Maybe part of the sediment is reworked during the Holocene and little structure is left.

5.4.4 *Sand Ridges*

Figure 5 shows a bathymetric map of the survey area, based on the maps of the Hydrographic Institute in The Hague, last updated in 1991. The data show an increasing depth from land to sea. Also, the pattern of the sand ridges is visible. In the survey area the water depth is between 10 and 30 m. The linear sand ridges, as described by Eisma (1968) and VanAlphen and Damoiseaux (1989), are clearly visible on the seismic data (figure 7.a). The western limitation of these ridges appears to be about 5.6° E. The sand ridges are several tens of km long, a few km wide and some meters high. The spacing at the crest is about 5 km. Their strike is in west to north-west direction (285°) and they make an angle of about 25° with the coast. Their crest becomes about 5 m shallower in landward direction over a distance of about 30 km. The sand ridges have, in general, an asymmetric form, their steeper side directed towards the south-west.

Most sand ridges have a reflector at their base, as shown in figure 7.a. This means that the sand ridges are relatively young features, which are not affected by early (Saalian) relief. The depth of these reflectors varies between 25 and 32 m below present sea level. The shallower reflectors are found towards the south-

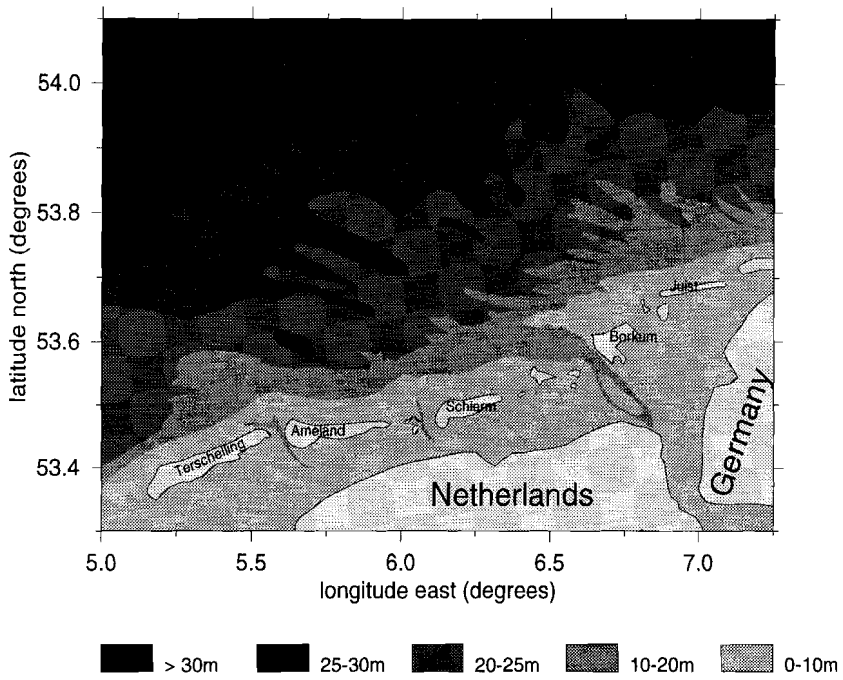

Figure 5. Bathymetric map of the survey area.

eastern part of the survey area. Some sand ridges show some internal seismic structure, but most of them do not. The base reflectors might be a ravinement surface as found in similar sand ridges along the New Jersey (U.S.A.) coast (Snedden et al. 1994). The base reflectors can also be a transition between marine sands as observed by v.d. Meene (1994) along the west coast of The Netherlands. A third possibility is that some of the base reflectors represent the top of the Eemian deposits.

About 50 boxcores were collected, both on the crest and in the troughs of the sand ridges. The sediments on the crest are well sorted, they consists of very fine sand, locally burrowed and anoxic at a depth of less than 2 cm. The sediments

in the troughs are coarser grained, poorly sorted and generally oxic, with evidence of storm reworking. The sand ridges in the survey area originated by reworking of the earlier deposited transgressive sand sheet (Kosters et al. 1992). This process of reworking may have begun after 5000 years BP, when sediment supply decreased because of progradation and sediment trapping of the western Netherlands strandplain (e.g. Roep et al. 1991, Beets et al. 1992). Based on the sediment characteristics it is concluded that the sand ridges are inactive under the present dynamic regime and their troughs possibly used as conduits for the tidal currents (Kosters et al., 1992).

The seismic records show no evidence that the ridges in the survey developed around a core of glacial till. D'Ollier (1981) suggested this as an explanation for comparable sand ridges in the Thames estuary which do not migrate.

Sand ridges of similar size (height, width and length) are found along the west coast of The Netherlands near IJmuiden (v.d. Meene 1994). The sediments show no variation in grainsize related to the topography. The sand ridges in this area migrate between 0.5 and 1 m per year in seaward direction. The sediment characteristics of these ridges are different from the sediment characteristics of the ridges in the survey area.

The sand ridges in the Southern Bight are an order of magnitude larger (Cameron et al., 1989) than the sand ridges in the study area. The tidal sand ridges in the Southern Bight are commonly interpreted as moribund having originated during the early Holocene, when strong tidal currents began to sweep through the newly inundated North Sea, while accommodation space was created by rapid sea level rise.

5.4.5 *Other Interesting Features*

Two clear channels were found and marked on the location map (figure 6) as circles (a) and (b). One channel (a) is about 30 km offshore the Terschelling-Ameland inlet (5.48° E, 53.69° N) and is probably an ancient glacial drainage system of the Borndiep (Kosters et al. 1992) which incised the Top Eemian reflector to a depth of about 45 m (60 ms) below NAP. The other channel (b) which incises the Top Eemian reflector (to a depth of 43 m (57 ms) below NAP) is found about 12 km offshore Terschelling (5.22° E, 53.55° N) and cannot directly be related to a present day tidal inlet or outlet. This is probably also part of the drainage system of the Borndiep because it is located approximately at the same

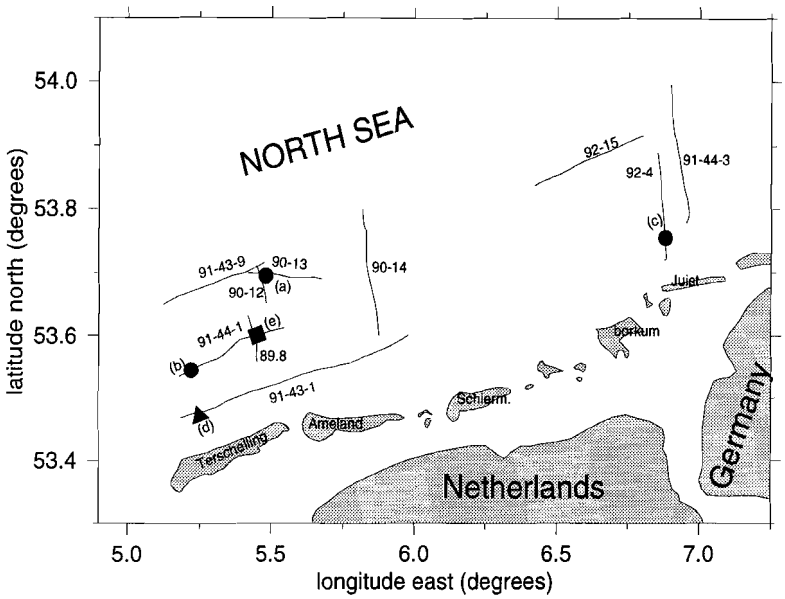

Figure 6. Location of special objects. The square (e) locates the Saalian till, the triangle (d) locates the ebb-tidal delta and the circles (a, b and c) locate the drainage channels.

depth. A third channel (c) is observed at 6.87° E, 53.75° N. This channel cannot directly be related to the other two channels; no clear Eemian reflectors are found here and the base of the channel is about 35 m (46 ms) below NAP. It might be part of an old drainage channel of the Ems river.

Line 91-43-1 shows a unit (figure 6, triangle (d)) with some internal structure around position 5.25° E, 53.47° N, about 7 km north of the barrier island Terschelling. The dip of the internal structure is about 0.07° in NE direction. In this same area other seismic lines also showed some dipping structures (VanMierlo, 1991 and Kosters et al., 1992). The dip found by Van Mierlo (1991) is 0.17° in northern direction. This structure is interpreted as an ebb-tidal delta, with its strike in east-west direction.

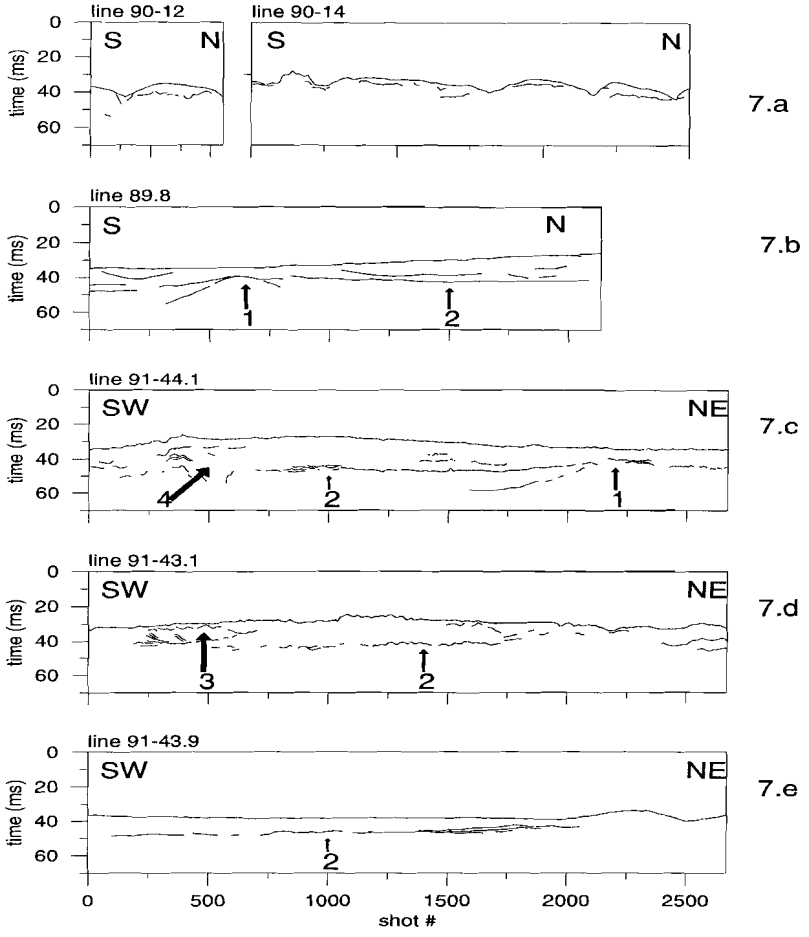

Figure 7. Line drawings of some lines with interesting features. Figure 7.a shows the sand ridges on lines 90-12 and 90-14. Other interesting features are marked, in figures 7.b to 7.e, by arrows and numbers where : 1= Saalian till, 2= top Eemian reflector, 3= ebb tidal delta and 4= old drainage channel.

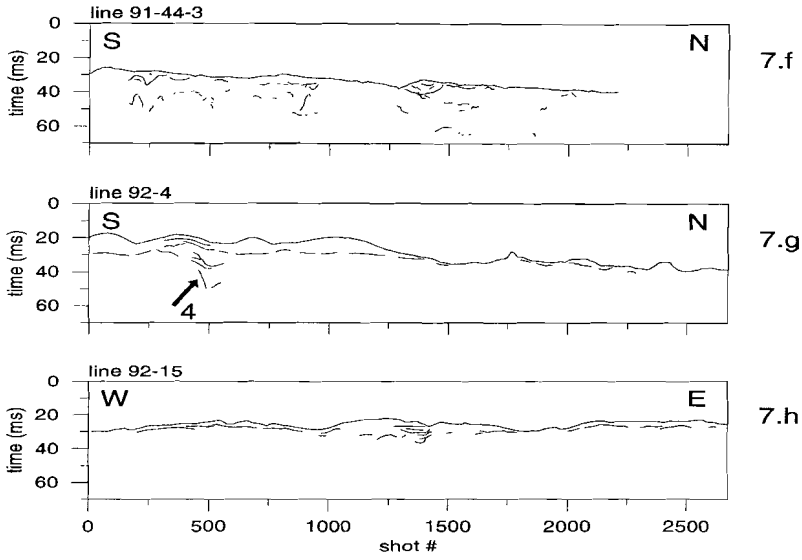

Figure 7 Continued. Line drawings of lines 91-44-3 (7.f), 92-4 (7.g) and 92-15 (7.h). Figure 7.f shows sand ridges in the eastern part of the survey area. The arrow (4) in figure 7.g indicates an old drainage channel.

Lines 92-4 and 92-15 (figures 7.g and 7.h) show some clear reflectors. The reflectors may be parts of channels of the old drainage system of the river Ems. The reflectors on line 92-4 are deeper (about 40 to 50 ms below sea-level) than the reflectors on line 92-15 (about 30 to 40 ms below sea-level). Many reflections, up to 50 ms below sea level, are visible in some parts of line 91-44-3 (figure 7.f). Perhaps these reflections come from relicts of old drainage channels, or parts of these reflections indicate the Saale reflector. Figure 7.h also shows some of the sand ridges.

5.5 *Conclusions*

The seismic data show a ice-pushed ridge of Saalian age with connected reflectors. The Saalian till in the western part of the survey area had its influence on sedimentation into the Holocene time. Onlapping to this ridge are Eemian sediments of which the top is a clear reflector which was observed mainly in the western part of the research area. The depth of this reflector varies between 27 m (35 ms) near the coast to 42 m (55 ms) in the north-eastern part of the survey area. The thickness of the post Eemian sediments varies between 4 m and 19 m. Incised in the Eemian sediments are several channels, which are probably old drainage channels of Weichselian ages from the Borndiep. In the eastern part of the survey area we see some evidence for a drainage channel from the river Ems. North of the barrier island Terschelling an ebb-tidal delta of Holocene age is observed. The reflector at the base of most sand ridges indicates that they are relatively young features. This base reflector of the sand ridges in the eastern part of the survey area indicates that these are not influenced by former topography.

Chapter 6

Case Study 2 : The Zeeland Bridge

6.1 *Introduction*

For the construction of the Zeeland Bridge, in the southwest of the Netherlands, 25 m to 50 m deep boreholes were made by the RGD (Dutch Geological Survey) at the positions of the bridge pillars. Based on these boreholes a geologic profile was constructed (RGD, project 380i, 1965); The top 50 m consists mainly of four layers; the top layer is the Holocene Duinkerke formation.

In September 1990 high-resolution seismic data were acquired along the Zeeland Bridge. The objective of the acquisition was to construct a line drawing (seismic interpretation) based on high-resolution seismic data and compare this interpretation with the geologic profile based on the boreholes. Enough resolution was needed to find internal structures in the Holocene deposits and sufficient penetration was aimed for to map all four layers.

6.2 *Acquisition*

Figure 1 shows a map of the survey area. The location of the Zeeland Bridge is shown as a line between N.Beveland and Schouwen Duiveland. The seismic line along the bridge was recorded from the small motor catamaran of the Marine Geophysics Group of Utrecht University. The speed of the catamaran during the profiling was about 1.2 m/s. The weather conditions during the measurements were good, the average wave height was about 25 cm. There was a strong tidal current perpendicular to the vessel. The current in combination with the low speed of the ship made it difficult to stay on course and acquire straight seismic lines.

A boomer was used as seismic source. The boomer was operated at an energy level of 300 J and was fired about every second. At this energy level the dominant frequency of the boomer is around 6 kHz. The data were received by a

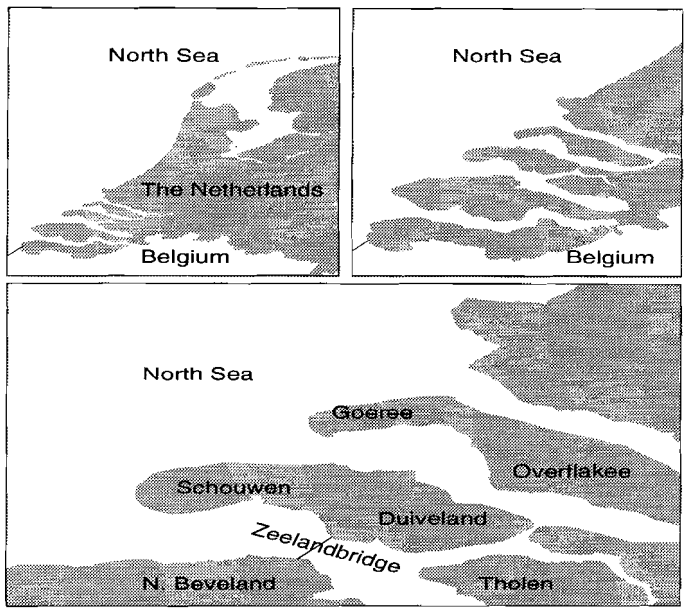

Figure 1. Map of the survey area. The location of the Zeeland Bridge is shown as a line between N. Beveland and Schouwen-Duiveland.

single-channel streamer which comprises eight hydrophones over 50 cm (section 1.4).

The source and receiver were towed about 20 m behind the ship; the offset between source and receiver was 1 to 2 m. The data were recorded digitally with the MDAS system (see section 1.5). Part of the data was digitized at a sample rate of 100 kHz and the other part at 50 kHz. Positioning was done by noting the shot number and the pillar number when a bridge pillar was passed.

Figure 2 shows the raw data between pillar 44 and 49. The reflection from the water bottom arrives around 20 ms. The position of the pillars can be recognized by the deeper parts in the water bottom reflection. Between pillars 47 and 49, shots 700 to 900, some reflectors are visible above 25 ms.

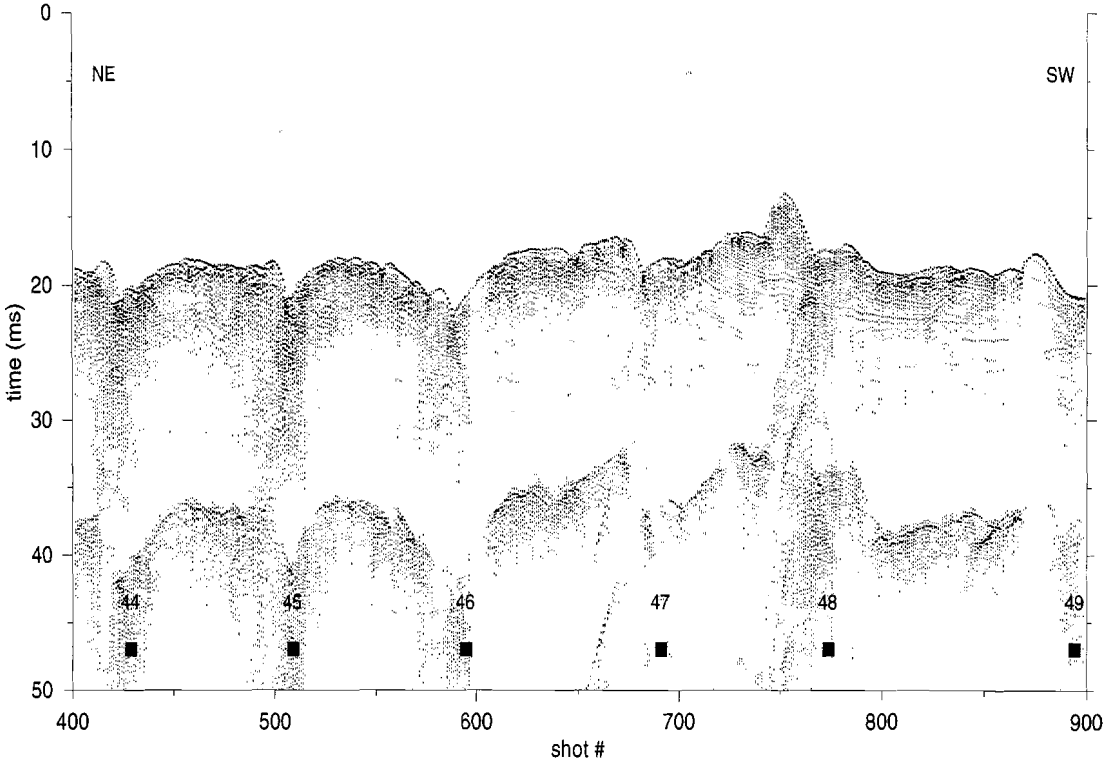

Figure 2. Example of raw data between pillars 44 and 49 of the Zeeland Bridge.

Pillar positions are marked by black squares.

6.3 *Processing*

To increase the signal-to-noise ratio and the resolution of the data the following processing steps were applied:

- DC-offset removal
- direct wave muting
- frequency filtering
- wavelet estimation
- wavelet shaping / wiener filtering
- match filtering
- trace mixing

The data had a small positive DC-offset. This DC-offset was removed by calculating the average amplitude of a trace, from sample 1000 to 5000 (from 10 ms to 50 ms), and subtracting the average amplitude from the trace. This was done for each shot.

The power cable to the boomer and the signal cable from the streamer were relatively close together. The electric current sent through the power cable to the boomer caused an 'induction' signal in the signal cable which was recorded by the system. By muting the first 1000 samples (10 ms) the effect of this electric induction was reduced. Another effect of this muting was that most of the direct wave was removed from the data.

The boomer had some low frequency ringing around 500 Hz. This ringing was removed by applying a zero-phase low-cut filter that suppressed frequencies below 750 Hz.

From the filtered data an average wavelet was estimated. This was done by transforming all traces to the frequency domain. The average frequency spectrum was calculated and resampled. Subsequently, a back transformation to the time domain was performed to obtain the average wavelet in the time domain.

The (mixed phase) average wavelet was used to design a wavelet shaping filter (Wiener filter). Wiener filtering can be used to transform a mixed phase wavelet into a spike. To obtain a 'good' spike the spike is delayed from the origin of the wavelet (Yilmaz, 1987). A time shift, equal to the delay, must be applied to the data after wiener filtering to move the spike back to the onset of the original wavelet.

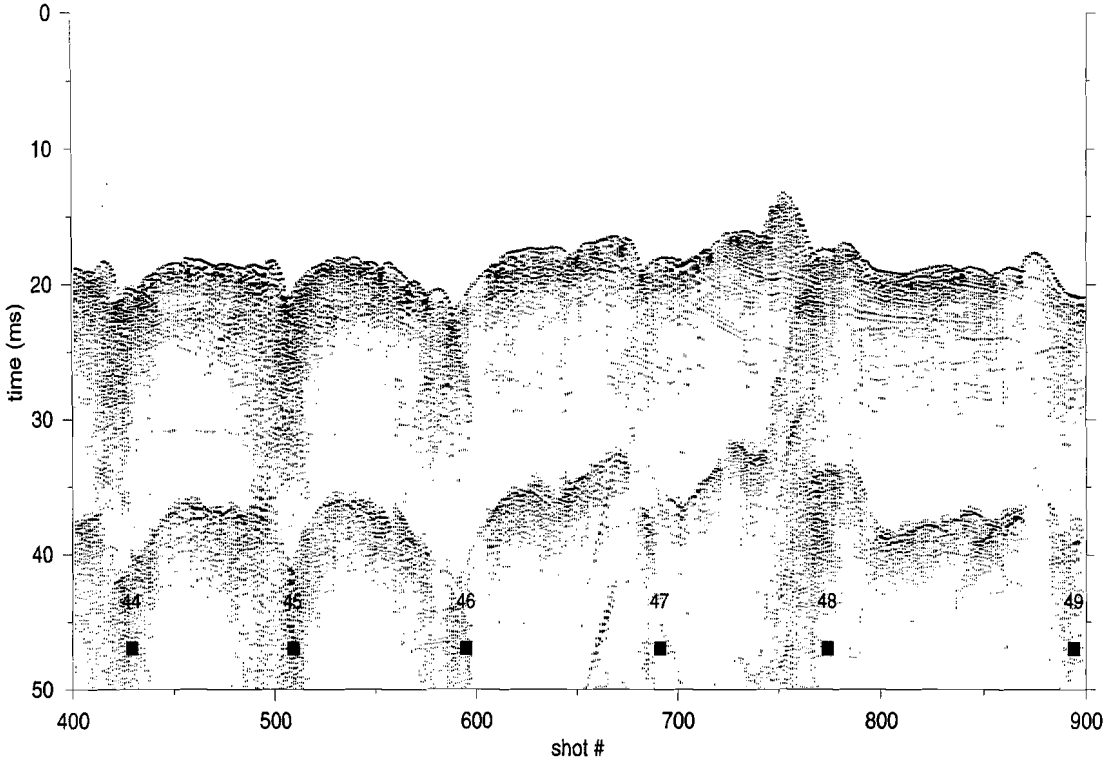

Figure 3. Example of processed data between pillars 44 and 49 of the Zeeland Bridge.

Pillar positions are marked by black squares.

To increase the signal-to-noise ratio match filtering was applied to the data after frequency filtering. The average wavelet was cross-correlated with the data. This will generate relatively high amplitudes when the data and the wavelet match and relatively low amplitudes when the wavelet is correlated with noise.

Wavelet shaping (Wiener filtering) and match filtering did not give satisfactory results because part of the data was clipped.

The last step in the processing was trace mixing (or lateral stacking). Here a three point stack with weights 0.2, 0.6 and 0.2 was applied to the data, where the middle trace is the position of the stack. The trace mixing improved the data quality and made the interpretation easier. A disadvantage of trace mixing is that the reflections from dipping reflectors can be suppressed. The boomer used in this study had a dominant frequency of 6000 Hz, giving a wavelength of about 25 cm. The shot interval was about 90 cm. This means that the dip of a reflector must be less than 2° to add constructively in three shots. Steeper dipping reflectors will be suppressed.

Figure 3 shows the data between pillars 44 and 49 after processing. Processing made the reflector around 32 ms between pillars 44 and 45 clearer.

6.4 *Interpretation*

First, the geological interpretation from pillar 39 to pillar 53 based on the boreholes at the pillar positions will be discussed. This interpretation is shown in figure 4. Then the interpretation of the seismic data will be given (line drawing, figure 6).

The interpretation based on the boreholes was made by the Dutch Geological Survey. Four formations are distinguished: The Duinkerke formation, the Twente formation, the Schouwen formation and the Tegelen formation. The formations consist predominantly of sand deposits with some thin slib and peat layers (Holzwilder, Grondmechanika Delft, 1991, personal communication).

Figure 4 shows that the thickness of the Holocene Duinkerke formation varies between 5 m and 20 m. In general the thickness increases from pillar 39 to 53. The Twente (Weichselian) formation varies in thickness between 0 m and 15 m. Between pillar 39 and 40 this formation is eroded by tidal channels in the Holocene.

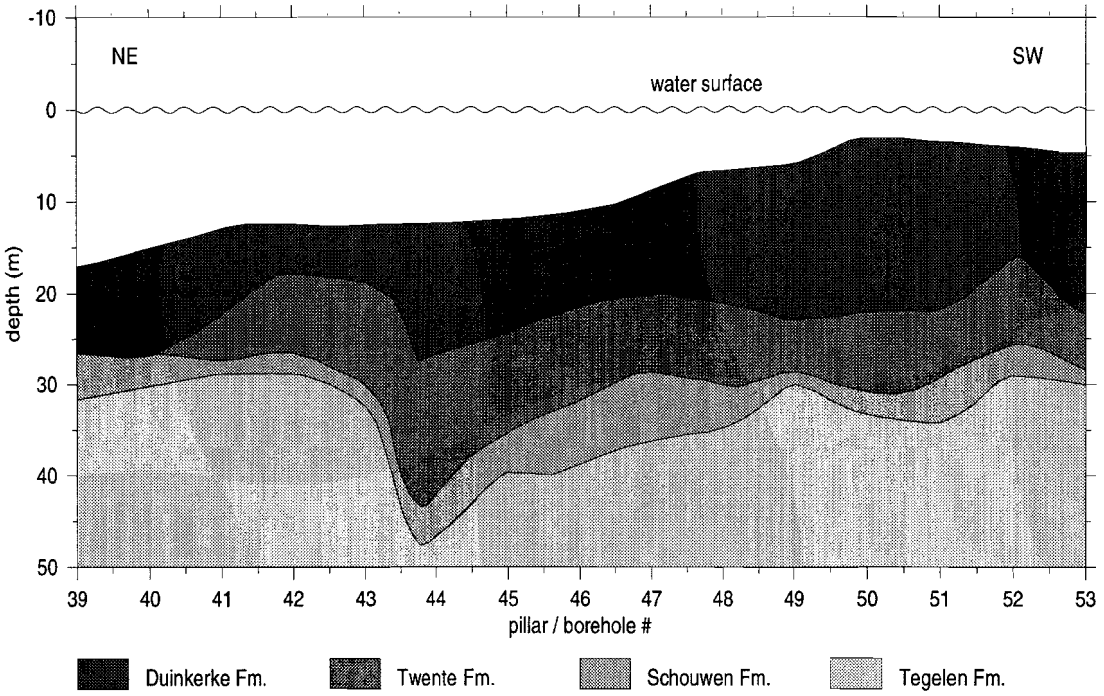

Figure 4. Geologic profile based on the boreholes at the pillar positions.

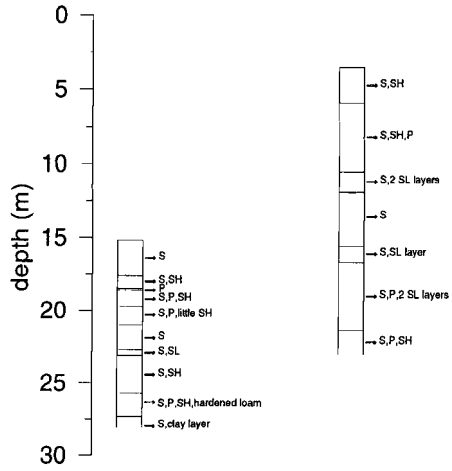

Figure 5. Boreholes at pillar 39 (left) and pillar 49 (right). S = sand, SH = shells, P = peat, SL = slib

The Twente formation has a high between pillars 42 and 43 and around pillar 52. A deeper part exists close to pillar 44. The Schouwen (Eemian) and the Tegelen formation also have a deeper part at this location. The Schouwen formation is between 2 and 10 m thick and is located between 25 and 45 m deep. It follows the top of the Tegelen formation.

Figure 5 shows a description of the boreholes at the positions of pillars 39 and 49. These boreholes are not deep and mainly cover the Duinkerke formation. The Duinkerke formation consists of several sand layers with some smaller peat and slib layers.

The line drawing (seismic interpretation) of the data between pillars 39 and 53 of the Zeeland Bridge is shown in figure 6. The water bottom is clearly visible on all recordings. At most pillar position the reflection from the water bottom arrives a few milliseconds later. From pillar 39 to 43 a reflector around 35 ms is visible. This reflector corresponds to the top of the Schouwen formation. Between pillars 43 to 44 a NE dipping reflector is visible which becomes horizontal from pillar 44 to pillar 45 at about 30 ms.

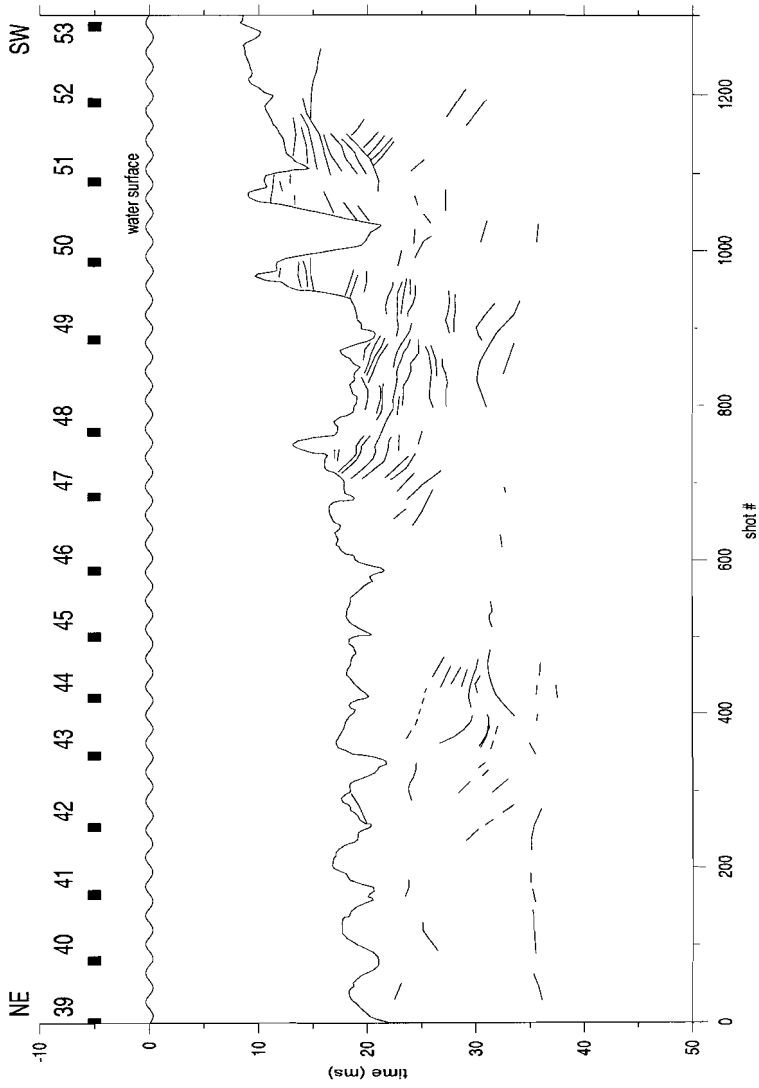

Figure 6. Line drawing (seismic interpretation) of the data. Pillar positions are marked as black squares and their numbers are marked.

Around pillar 49 we see a SW dipping reflector at about 30 ms. Above these reflectors we see many smaller reflectors. They all dip towards the SW. The dip is maximal about three degrees (between pillars 47 and 48) and becomes smaller between pillars 48 and 49. Close to the end of the bridge (from pillar 50 to 53) we see that the SW dipping reflectors are truncated by reflectors dipping to the NE between 15 and 20 ms. We do not see this further along the bridge, probably because the water bottom is too deep (about 15 m). The dipping reflectors correspond to the internal layering of the Duinkerke formation which is also visible in the boreholes (figure 5).

6.5 *Conclusions*

Only some of the objectives were achieved in this survey. The resolution was high enough to map the internal structure of the Holocene deposits. However, the penetration was not deep enough to map the deeper Schouwen and Tegelen formations.

There are two reasons for this lack of penetration. The first reason is that the bottom has a high reflection coefficient, and therefore little energy is transmitted through the water bottom. The other reason is that a boomer is not a very 'strong' source and has little low frequency content. The higher frequencies were attenuated rather quickly by the sediments along the Zeeland Bridge.

To map the deeper layers in this area a stronger source, such as a pneumatic source, is needed.

Chapter 7

Case Study 3 : The North Sea Canal[1]

7.1 *Introduction*

In the summer of 1993 single channel seismic profiling was carried out on the North Sea canal in The Netherlands. This canal connects Amsterdam with the North Sea and is busy with large container ships and international ferries as well as small local ferries, local freight ships and a host of sailing and motor boats. All this traffic makes the profiling complicated.

Boreholes near the canal show that the geology consists of a series of glacial basins up to about 100 m deep (RGD, Dutch Geological Survey, project 10841, 1990). The basins are filled predominantly with clay. The top of the clay is situated between 25 and 50 m below Nieuw Amsterdams Peil (NAP, zero level). Above this clay, Pleistocene sand formations are present. The top of the sand deposits varies between 15 and 25 m below NAP. Above these Pleistocene deposits, sand, clay and peat beds are present (De Gans, 1991).

Four seismic sources were tested to see which source had (1) enough penetration to observe the glacial basins and (2) enough resolution to observe the top level of the Pleistocene deposits and the structure of the Holocene deposits.

Figure 1 shows a map of the research area. The boreholes (black dots) as well as the start and end of the seismic line are indicated on this map.

---

1 Part of this chapter has been published as : Canal Seismics in The Netherlands, Verbeek N.H., OldeMonnikhof C., Koktas M., McGee T.M., DeGans W. and Zwaan H., Second European Conference on Underwater Acoustics, L. Bjørnø (ed.), 937-941, Elsevier applied science series, 1994.

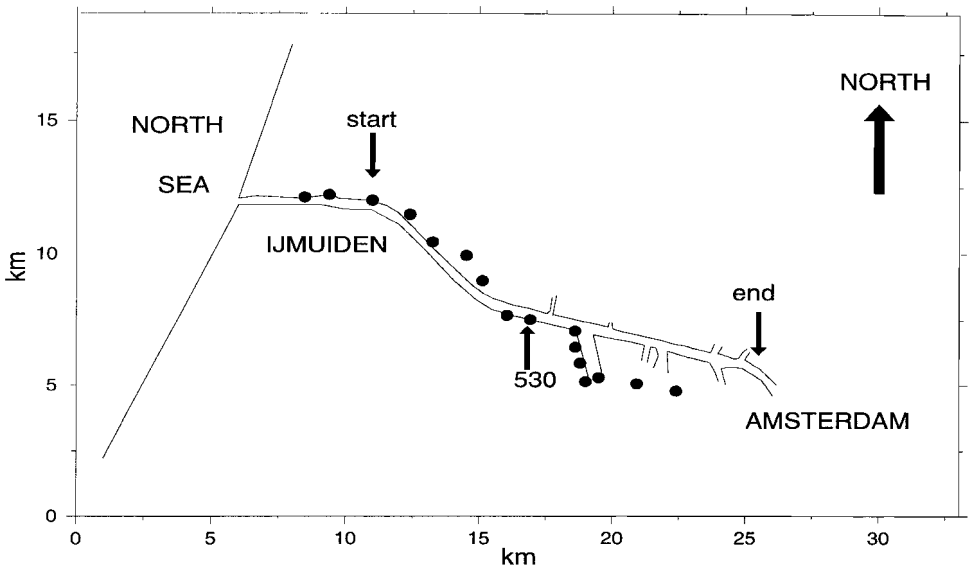

Figure 1. Map of the research area. The canal, the boreholes (black dots) and the start and the end of the seismic line are shown. Borehole 530 is also indicated.

7.2 *Acquisition*

The data acquisition was done with four different seismic sources: two pneumatic type sources (an airgun and a watergun) and two electric discharge sources (a boomer and a multitip sparker). The background and the characteristics of these sources are discussed in detail in Chapter 1 and Chapter 2. The data were received with a single-channel streamer comprising eight hydrophones over an active length of 50 cm. The source and the streamer were towed about 25 m behind the ship. The source/receiver offset was intended to be 2 m. All sources were operated close to the surface to reduce the 'ghost time' and, for the airgun, to suppress the bubble pulses (see section 1.3). The pressure of operation was around 100 bar for both the airgun and the watergun. The shot rate of both guns was about one shot every five seconds, which resulted in an average shot interval of about 10

m. The shot rate of the boomer and the sparker was about one shot every 2 seconds, corresponding to an average shot interval of about 4 m. The boomer and sparker were operated at 300 Joules. The data acquired with the airgun, watergun and sparker were digitized at 20 kHz, the boomer data were digitized at 50 kHz.

The position was obtained with differential GPS. The relative accuracy of the positioning was 1 to 2 m. For each shot the position was stored in the shot header. Along the canal signs are placed at every kilometer. When such a sign was passed the shot number was noted in a logbook and the recorded data were marked.

A small portion of the raw data for each source, close to borehole 530 (see figure 1), is shown in figures 2.a through 2.d. The location of the sparker, boomer and watergun profiles were within a couple of meters the same. Around shot 50 (see figure 2.b) the location of the boomer line was 15 m more towards the middle, deeper part, of the canal. The airgun profile was in general about 10 m more towards the middle of the canal. The sparker and the boomer lines (figures 2.a and 2.b) are about 800 m long. In these data sets a horizontal reflector is visible around 17 ms. In the sparker data (figure 2.a), a reflector around 50 ms is also visible. The airgun and the watergun lines (figures 2.c and 2.d) are about 2 km long. In the airgun data (figure 2.c) a horizontal reflector is visible around 35 ms. Also visible is some bubble related signal between 60 and 70 ms.

7.3 *Processing*

For all four sources, 200 traces were selected near borehole 530 (see figure 1). On these four data sets, shown in figures 2.a through 2.d, processing methods were tested. There were two reasons for doing this. Firstly, to decide which processing methods should be used to process the whole line from IJmuiden to Amsterdam. Secondly, to find which source, after processing the data, had enough penetration to observe the glacial basins and thereby the highest resolution. The data acquired with the sparker gave the best combination of resolution and penetration, before and after processing. This section describes the processing applied to the sparker data close to borehole 530. The following processing methods were applied :

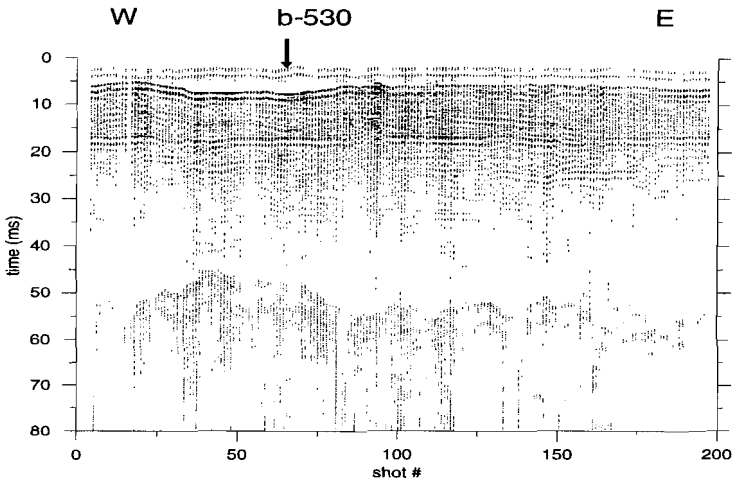

Figure 2.a. Raw sparker data near borehole 530.

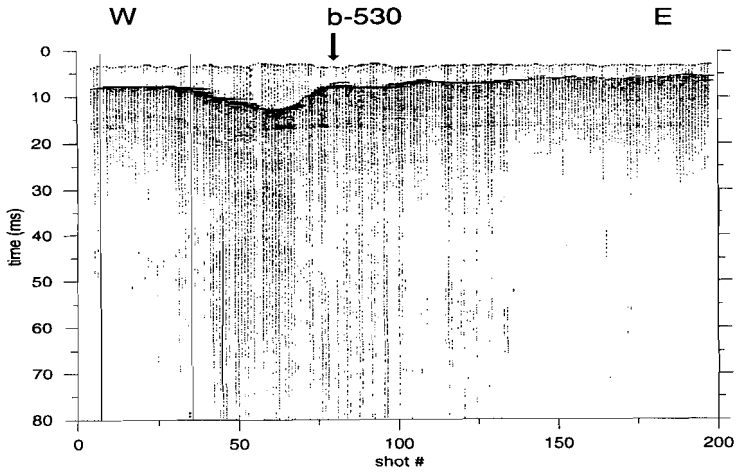

Figure 2.b. Raw boomer data near borehole 530.

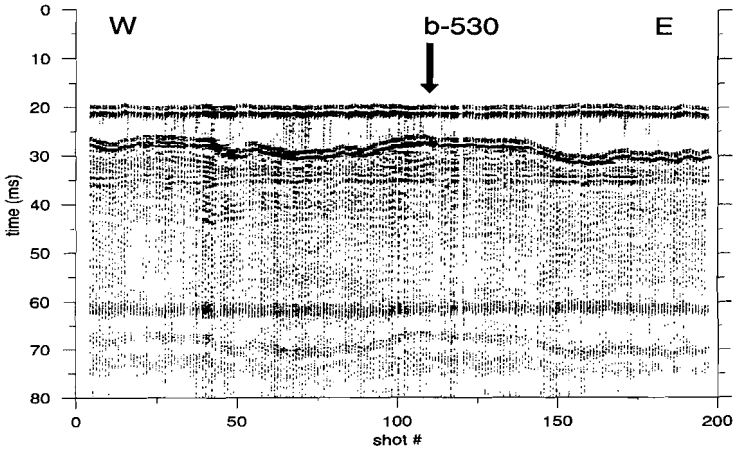

Figure 2.c. Raw airgun data near borehole 530.

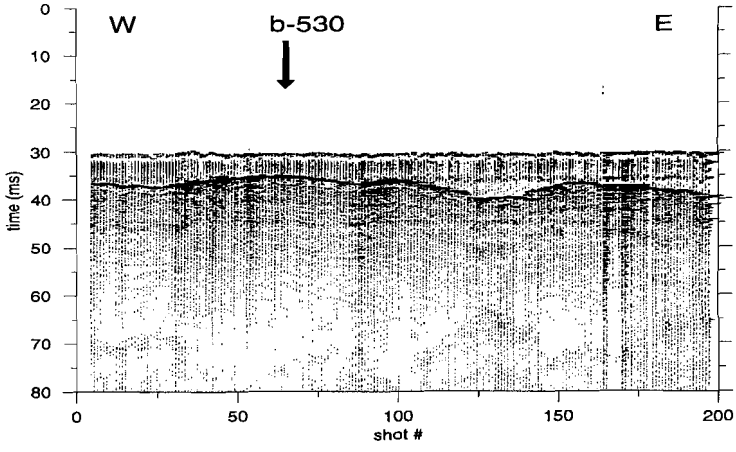

Figure 2.d. Raw watergun data near borehole 530.

- mute direct wave
- remove DC-offset
- band-pass frequency filtering
- wavelet estimation
- match filtering
- wavelet shaping
- trace mixing
- GA deconvolution
- SVD deconvolution
- geometrical spreading correction

The arrival time of the direct wave is between 1 and 2 ms, indicating that the offset between sparker and streamer was 1.5 to 3 m. The bottom reflection always arrives after more than 4.5 ms. The first step in the processing involved muting of the direct wave, which meant muting the first 4.5 ms of the records. Most, though not all, of the direct wave is suppressed, because on some shots the tail of the direct wave coincides with the bottom reflection.

After muting the direct wave the data were made 'zero mean' by calculating the average amplitude of each data trace and subtracting the average amplitude from each data trace.

A zero phase band-pass frequency filter was applied to the data to increase the signal-to-noise ratio. Several band-pass filters were tested. The filter 125-375 / 4000-6000 Hz gave the best results. This means that all amplitudes below 125 Hz and above 6000 Hz are set to zero. The amplitudes between 375 and 4000 Hz are unaltered. Between 125 and 375 and 4000 and 6000 Hz a cosine taper was applied to the data.

After frequency filtering a wavelet was estimated from the data. The wavelet was estimated by averaging in the frequency-domain. A certain number of shots (whole traces) is transferred to the frequency domain. In the frequency domain the amplitudes are averaged. Then, the average frequency spectrum is resampled with the number of points required to describe the wavelet. The average wavelet is shown in figure 3. For further processing the average wavelet was used.

To increase the resolution, wavelet shaping was applied. The shaping filter transformed the average wavelet into a delayed spike (Yilmaz, 1987). The shaping filter was applied in the time domain. The results of the shaping filter are shown in figure 4.a. The bottom reflection and the horizontal reflector around 17 ms are clearly visible. Between shot 100 and 180 a reflector just below the water bottom

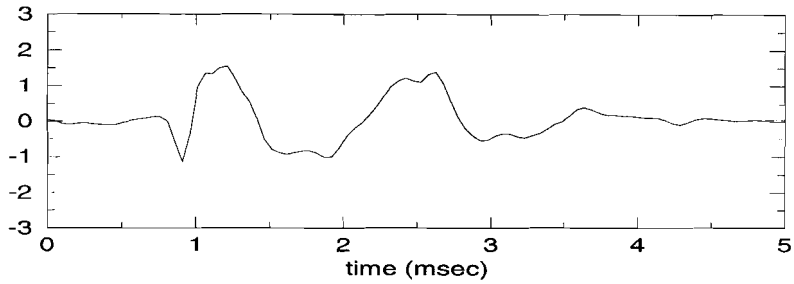

Figure 3. Estimated source wavelet.

is visible. Another reflector, between shot 120 and 150 and dipping from west to east, is less clear. Around shot 150 a reflector is visible around 25 ms. The reflector between 50 and 60 ms is visible, although not clearer than in the band-pass filtered data.

To increase the signal-to-noise ratio match filtering was applied to the data. Match filtering is a cross-correlation between the data and the estimated wavelet. Figure 4.b shows the results of match filtering. The match filter decreases the resolution in such a way that it becomes more difficult to pick the arrival times of the reflectors. The dipping reflector between shot 120 and 150 is now more outstanding than in the shaped data. This reflector is bounded by the clear reflector around 15 ms and another horizontal reflector around 8 ms. The deep reflector, between 50 and 60 ms, is less clear.

Another method to improve the signal-to-noise ratio is trace mixing. In this study three-point weighed trace mixing is applied. This means that shot i after trace mixing is formed by a summation of shots $i-1$, i and $i+1$ with weights of respectively 0.2, 0.6 and 0.2. Best results were obtained when trace mixing was applied after match filtering. In combination with wavelet shaping trace mixing had minor effects.

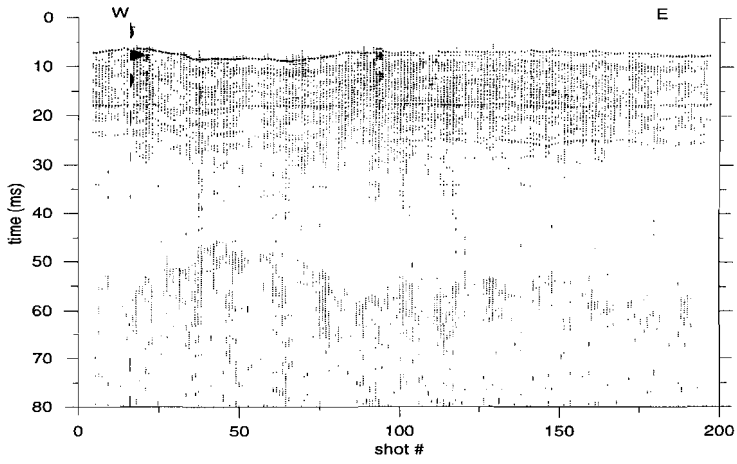

Figure 4.a. Sparker data after wavelet shaping.

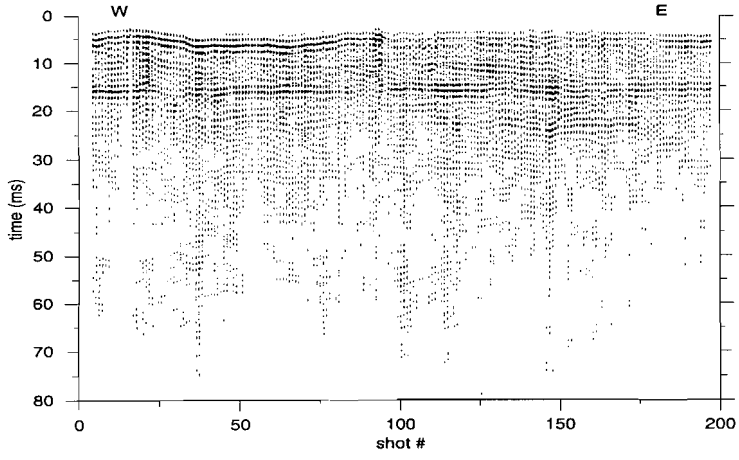

Figure 4.b. Sparker data after match filtering.

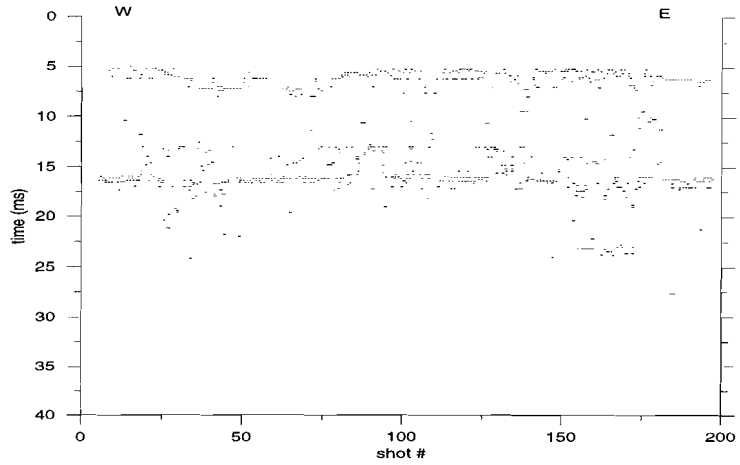

Figure 5.a The model after GA deconvolution. On each trace only the 5 reflectors with the highest score are shown.

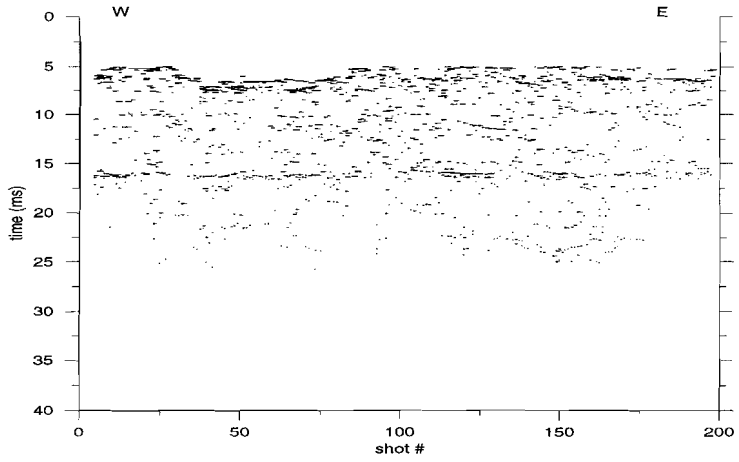

Figure 5.b The model after iterative SVD deconvolution.

In Chapter 5 the use of genetic algorithms (GA) for deconvolution of seismic data is described. This method was applied to the data. The GA had to search for 5 reflectors with 4 samples resolution for position and a resolution of 0.02 for amplitude. In total 10 separate GA runs, with different starting models and control parameters, were performed. The results of these runs were combined to a score model. The models formed by the 5 samples with the highest score are shown in figure 5.a. The bottom reflection is clearly visible. Between shots 90 and 180 a second reflector just below the bottom reflection is visible. This reflector is also visible between shots 10 and 20 and corresponds to the reflector visible just below the bottom reflection in the data after wavelet shaping. The horizontal reflector around 17 ms is very clear, although it is less clear between shots 120 and 180. Around 13 ms some reflectors are present which do not correspond to the data after other processing steps. With the GA deconvolution the main features in the seismic data are found.

The results for iterative SVD deconvolution (see Chapter 4) are shown in figure 5.b. The iteration was started with a reflector separation of 2.5 ms. The bottom is the strongest reflector found. The results of this inversion indicate a reflector between shots 90 and 170 about 1.5 ms below the bottom. The horizontal reflector around 17 ms is clear. The reflector around shot 150 at 24 ms deep is also found. The shaping filter appears to give the more information about the reflectors than the GA and the iterative SVD deconvolution.

The last processing step was a correction for the geometrical spreading of the propagating wavefront. In this case a spherical correction (linear in time) was used as a first approximation of the directivity of the sparker source.

7.4 *Interpretation*

Different processing steps highlight different features in the seismic data and therefore the interpretation is based on four sets of processed data; the set after muting the direct wave, DC-offset removal and frequency filtering, the set after wavelet shaping, the set after match filtering and trace mixing and the set after iterative SVD deconvolution. Figure 6 shows the interpretation of previously discussed data (close to borehole 530), together with borehole 530.

The first reflector, around 7 ms, is the water bottom reflection. The reflector around 50 ms corresponds to the boundary between the glacial basins, which are partially filled with clay, and the Pleistocene sands above it. The reflector around 17 ms represents the boundary between the alternating sand, clay

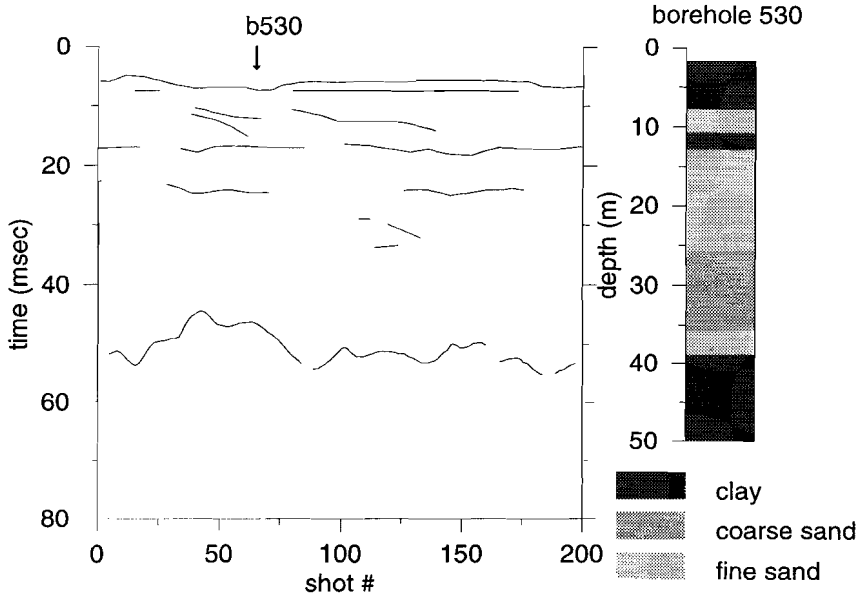

Figure 6. Seismic interpretation based on data shown in figure 4 and description of borehole 530.

and peat layers from the Holocene and the sand deposits from the Pleistocene. The depth of this reflector is in good agreement with depth soundings. The depth soundings show a layer with a strong penetration resistance at 12.7 m depth, at the location of borehole 530. The reflections between 17 and 50 ms probably correspond to boundaries between fine and course sands in the Pleistocene deposits. Reflections above 17 ms correspond to the alternating sand, clay and peat layers of the Holocene deposits. Information from borehole 530 and a depth sounding at that location are in close agreement with the information from the seismic data.

The geologic interpretation based on borehole information is shown in figure 7.a together with the results from depth soundings. The final seismic

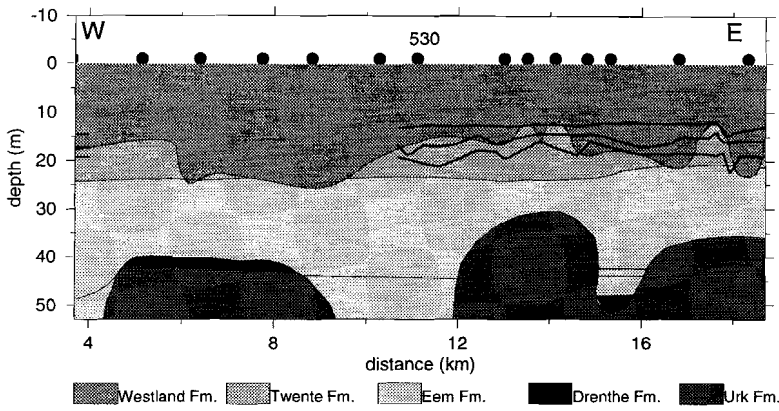

Figure 7.a. Geological profile based on the boreholes shown in figure 1 (Made by the RGD, project 10841, 1990). The results of depth soundings, also made by the RGD, are shown as thick solid lines (De Gans, personal communication, 1994).

interpretation (line drawing) is shown in figure 7.b. In this area 5 layers can be recognized, based on the borehole information. The top layer is the Holocene Westland Formation, which consists of alternating sand, peat and clay layers. The second layer is the late Weichselian, early Holocene Twente Formation, which consists of fine sands. Below these two layers is the Eem Formation. The upper parts of the glacial basins, near km 4, 12 and 16, are filled with the Eem Formation and the lower parts are filled with the Drenthe Formation. The upper part of the Eem Formation mainly consists of sand and the lower part of clay. The Drenthe Formation consists mainly of clay. The lowest formation is the Urk Formation, which predominantly contains sand.

Figure 7.a also shows the results of depth soundings made by the RGD along the canal. Three boundaries were found. These three boundaries are only observed east of km 10.5, except for a small area around km 3.7. The upper boundary, about 12.5 m deep, marks the top of a layer with high penetration resistance which is interpreted as the top of the Pleistocene deposits by the RGD. The second boundary marks the bottom of this layer. The third boundary marks the

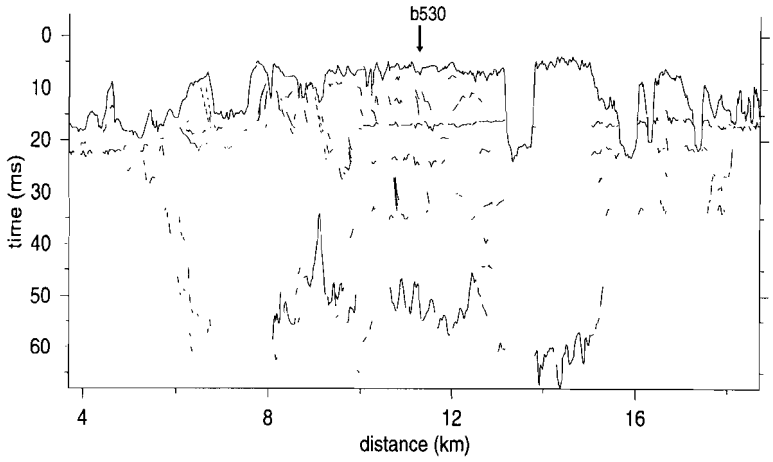

Figure 7.b. Line drawing (Seismic interpretation) based on the processed sparker data.

top of a second layer with high penetration resistance. Differences between the borehole and depth sounding information is partly due to the fact that some boreholes are about 2 km away from the canal and that all depth soundings were made are directly along the canal.

The seismic data show a deep reflector (around 40-60 ms, 30-45 m) which is the top of the clay-filled glacial basins. The strong reflector around 17 ms corresponds to a layer of high penetration resistance, which marks the top of the Pleistocene sands. This layer is deeper and less clear in the western part of the canal. This information has been confirmed by depth soundings along the canal. In the eastern part of the canal, shots 2000 to 5000, a second reflector around 25 ms appears, which is also confirmed by the depth soundings. The strong reflector near 17 to 20 ms cannot be related directly to borehole information. The seismic data indicate that this is an almost flat boundary, between shots 2000 and 3000, which is not clear from the borehole data. This is partly because some boreholes are about 2 km away from the seismic line. However, the depth soundings confirm the flatness of this boundary. The fit between the seismic data and the borehole information

varies along the profile. Around borehole 530 the fit is good (see fig. 6), in some other parts of the profile the fit is not good. The correlation between the depth soundings and the upper 30 ms of the seismic data is good.

7.5 *Conclusions*

From the previous sections it is concluded that single-channel marine seismic profiling in busy canals gives useful information. A comparison between the profiles acquired with different sources, before and after processing, shows that the multitip sparker gives the most useful information in terms of penetration and resolution.

The seismic data around borehole 530 closely match the borehole and depth sounding information. The seismic information and the borehole interpretation differ strongly in some other parts of the line. The seismic data indicate that the Pleistocene Holocene boundary in this area is very flat, which is not clear from the borehole information. Depth soundings, however, confirm that this is indeed an almost horizontal boundary. The seismic data give additional information about the top of the glacial basins.

References

Alonso, M. and Finn, E.J., Fundamentele Natuurkunde, deel 1, Mechanica, Delta Press B.V., Oudewater, 1983.

Barrodale I., Zala C.A. and Chapman N.R., Comparison of the l_1 and l_2 norms applied to one-at-a-time spike extraction from seismic data, Geophysics, **49**, 11, 2048-2052, 1984.

Beets, D.J., VanderValk, L. and Stive, M.J.F., Holocene evolution of the coast of Holland. Mar. Geol., **87**, 1, 3-24, 1992.

Berkhout, A.J., Seismic Resolution; resolving power of acoustical echo techniques. Volume 12 of Handbook of Geophysical Exploration, Section I, Seismic Exploration, Geophysical Press, London, 1984.

Burdic, W.S., Underwater Acoustic System Analysis, Prentice-Hall Inc., Englewood Cliffs, New Jersey, 1984.

Cameron, T.D.J., Schüttenhelm, R.T.E. and Laban, C., Middle and Upper Pleistocene and Holocene stratigraphy in the Southern Bight of the North Sea. In : J.P. Henriët and G. DeMoor, (Editors), The Quaternary and Tertiary Geology of the Southern Bight, North Sea. State University of Gent, Reinar Centre of Marine Geology, pp. 119-137, 1989.

Chapman N.R. and Barrodale I., Deconvolution of marine seismic data using the l_1 norm, Geophysical Journal of the Royal Astronomical Society, **72**, 93-100, 1983.

Claerbout, J.F., Earth soundings analysis. Blackwell Scientific Publications, 1992.

Claerbout J.F. and Muir F., Robust modeling with erratic data, Geophysics, **38**, 826-844, 1973.

Davis, L., Handbook of Genetic Algorithms, Van Nostrand Reinhold, New York, 1991.

Dobrin, M.B. and Savit, C.H., Introduction to Geophysical Prospecting, McGraw-Hill Book company, Singapore, 1988.

D'Olier, B., Sedimentary events during Flandrian sea level rise in the southwest corner of the North Sea. In: Nio, S.D., Scuttenhelm R.T.E. and T.C.E. van Weering (eds.), Holocene Marine Sedimentation in the North Sea. International Association of Sedimentologists, 221-227, 1981.

Eisma, D., Composition, Origin and Distribution of Dutch Coastal Sands between Hoek van Holland and the Island of Vlieland. Brill Publishers, Leiden, 267 pp, 1968.

Eisma, D., Mook, W.G. and Laban. C., An early Holocene tidal flat in the Southern Bight. In: Nio, S.D., Scuttenhelm R.T.E. and T.C.E. van Weering (eds.), Holocene Marine Sedimentation in the North Sea. International Association of Sedimentologists, 229-237, 1981.

Fitzgerald, D.M. and Penland, S., Backbarrier dynamics of the East Frisian islands, J. Sediment. Petrol., **57**(4), 746-756, 1987.

Franken, A.F., Reconstructie van het paleo-getijklimaat in de Noordzee. Waterloopkundig Laboratorium, Raport X 0029-00, 74pp. + app, 1987.

Gallagher. K., Sambridge. M., and Drijkoningen, G., Genetic algorithms : an evolution from monte carlo methods for strongly non-linear geophysical optimizing problems, Geophysical Research Letters, **18**, 12, 2177-2180, 1991.

Gans, W. de, Kwartairgeologie van West-Nederland, Grondboor en Hamer, 5/6, 115-124, 1991.

Henriët, J.P., Verschuren, M. and Versteeg, W., Very high resolution 3D seismic reflection imaging of small-scale structural deformation., First Break, **10**(3), 81-88, 1992.

Jansen J.H.F., van Weering T.C.E., and Eisma D., Late Quarternary sedimentation in the North Sea. In : Oele E., Schüttenhelm R.T.E. and Wiggers A.J. (eds) : The quaternary history of the North Sea Acta. Univ. Ups. 2, 175-187, 1979.

Jelgersma J., Sea level changes in the North Sea basin. In : Oele E., Schüttenhelm R.T.E. and Wiggers A.J. (eds) : The quaternary history of the North Sea Acta. Univ. Ups. 2, 233-248, 1979.

Jelgersma J., Oele E and Wiggers A.J., Depositional history and coastal development in the Netherlands and the adjactent North Sea since the Eemian. In : Oele E., Schüttenhelm R.T.E. and Wiggers A.J. (eds) : The quaternary history of the North Sea Acta. Univ. Ups. 2, 115-142, 1979

Joon B., Laban C. and Meer J.J.M., The Saalian glaciation in the Dutch part of the North Sea. Geologie en Mijnbouw, **69**, 151-158, 1990.

Kosters E.C., VanMierlo B.J.E.M., Verbeek N.H., Posthumus B.J., McGee T.M. and Brouwer J. Late Quarternary Stratigraphic Signature, Offshore from the Dutch Barrier Shoreline. Sedimentary Geology, **80**, 199-212, 1992

Lines L.R. and Treitel S., A review of least-square inversion and its application to geophysical problems, Geophysical Prospecting, **32**, 159-186, 1984.

Lomax, A., and Snieder. R., Finding sets of acceptable solutions with a genetic algorithm with application to surface wave group dispersion in Europe, Geophysical Research Letters, **21**, 24, 2617-2620, 1994.

Long D., Laban C., Streif H., Cameron T.D.J and Schüttenhelm R.T.E. The Sedimentary record of climatic variation in the Southern North Sea. Phil. Trans. R. Soc. Lond., B 318, 523-537, 1988

McGee, T.M., Single-channel Marine Seismic Profiling and The Analysis of Reverberatory Sequences, PhD Thesis University of Utrecht, The Netherlands, Geologica Ultraiectina, **78**, 87pp, 1991.

McGee, T., Davis, A., Anderson, H., and Verbeek, N., High-resolution marine seismic source signatures. European Conference on Underwater Acoustics, M. Weydert ed., 639-643. Elsevier Applied Science Series, 1992.

McGee, T. M., A method of calculating digitization rates for subbottom reflection data. Second European Conference on Underwater Acoustics, Copenhagen. L. Bjorno ed. Elsevier Applied Science Series, 1994.

Meene, v.d., J.W.H., The shoreface-connected ridges along the central Dutch coast. PhD Thesis University of Utrecht, The Netherlands, 209pp, 1994.

Niessen A.C.H.M., Project Kustgenese; Geologisch onderzoek van het kustgebied van de Wadden eilanden, Rijks geologische dienst, pp 1-22, 1990

Nolte, B., and Frazer, L. N., Vertical Seismic profile inversion with genetic algorithms, Geophysic Journal International, **117**, 162-178, 1994.

Oele, E. and Schüttenhelm, R.T.M., Development of the North Sea aftre the Saalian glaciation. In : E. Oele, R.T.M. Schüttenhelm & A.J. Wiggers (eds.) : The quarternary history of the North Sea - Acta. Univ. Ups. 2 : 191-215, 1979.

Owen, T.R.E. and Sinha, C., A PC-based seismic acquisition system, First Break, **8**(2), 57-62, 1991.

Parkes, G. and Hatton, L., The marine seismic source, D. Reidel Publishing company, Dordrecht, 1986.

Posthumus, B.J., MDAS, a Marine Data Acquisition System, Internal publication of the Department of Exploration Geophysics, Utrecht University, The Netherlands, 1991.

Press, W.H., Flannery, B.P., Teukolsky, S.A. and Vetterling, W.T., Numerical Recipes in C, Cambridge University Press, Cambridge, 1988.

Riel van P. and Berkhout A.J., Resolution in seismic trace inversion by parameter estimation, Geophysics, **50**, 9, 1440-1455, 1985.

Robinson, E.A., and Treitel, S., Geophysical Signal Analysis, Englewood Cliffs, N.J., Prentice-Hall Inc, 1980.

Roep, Th.B., VanderValk, L. and Beets, D.J., Strandwallen en zeegaten langs de Hollandse kust. Grondboor en Hamer, 5/6, 115-124, 1991.

Sambridge, M., and Drijkoningen, G., Genetic algorithms in seismic waveform inversion., Geophysic Journal International, **109**, 323-342, 1992.

Schock, S.G., LeBlanc, L.R. and Mayer, L.A., Chirp subbottom profiler for quantitative sediment analysis, Geophysics, **54**, 4, 445-450, 1989.

Sen, M. K. and Stoffa, P. L., Rapid sampling of model space using genetic algorithms : examples from seismic waveform inversion., Geophysic Journal International, **108**, 281-292, 1992.

Sha L.P., Sedimentological studies of the ebb-tidal deltas along the West Frisian Islands, The Netherlands. PhD thesis, University of Utrecht, The Netherlands, Geologica Ultraiectina, **64**, 160 pp., 1990.

Sluis v.d. A. and v.d. Vorst H.A., Numerical solution of large, sparse linear algebraic systems arising from tomographic problems, in : G. Nolet (ed), Seismic Tomography; with applications in global seismology and exploration geophysics, 49-83, 1987.

Snedden, J.W., Tillman, R.W., Kreisa R.D., Schweller, W.J., Culver, S.J. and Winn R.D., Stratigraphy and genesis of modern shoreface-attached sand ridge, Pheahala ridge, New Jersey. Journal of Sedimentary Research, **B64**, no. 4, 560-581, 1994.

Stoffa, P. L. and Sen, M. K., Nonlinear multiparameter optimization using genetic algorithms : Inversion of plane wave seismograms., Geophysics, **56**, 1794-1810, 1991.

Streif H. Barrier islands, tidal flats, and coastal marshes resulting from a relative rise of sea level in East Frisia on the German North Sea coast. Proceedings KNGMG Symposium "Coastal lowlands, Geology and Geotechnology", 213-225, 1989

Telford, W.M., Geldart, L.P. and Sheriff, R.E., Applied Geophysics, Cambridge University Press, Cambridge, 1990.

Tree, E.L., Lugg, R.D. and Brumitt J.G., Why waterguns ?, Geophysical prospecting, **34**, 302-329, 1986.

Urick, R.J., Principles of underwater sound, McGraw-Hill Book Company, 1983.

VanAlphen J.S.L.J., and Damoiseaux M.A., A geomorphological map of the Dutch shoreface and adjactent part of the continental shelf. Geologie en Mijnbouw, **68** (4), 433-445, 1989.

Van der Spek, A.J.F., Development of the Dutch Waddensea system under Holocene sea level rise. Mededelingen Rijks Geologische Dienst, Haarlem, 1992.

Van Mierlo B.J.E.M., Post Saalian sedimentation and its preservation in relation to the Holocene sea-level rise offshore Terschelling and Ameland, The Netherlands. MSc thesis, Utrecht University, Institute for Earth Sciences, 72 pp, 1991.

Verbeek, N.H., Directivity of high-resolution marine seismic sources. European Conference on Underwater Acoustics, M. Weydert ed., 644-647. Elsevier Applied Science Series, 1992.

Verbeek N.H., OldeMonnikhof C., Koktas M., McGee T.M., DeGans W. and Zwaan H., Second European Conference on Underwater Acoustics, L. Bjørnø (ed.), 937-941, Elsevier applied science series, 1994.

Verbeek, N.H. and McGee, T.M., Characteristics of High-Resolution Marine Reflection Profiling Sources, accepted for publication in Journal of Applied Geophysics, 19pp, 1995.

Wilson, W.G. and Vasudevan, K., Application of genetic algorithm to residual statics estimation, Geophysical Research Letters, **18**, 12, 2181-2184, 1991.

Yilmaz, O., Seismic Data Processing, Volume 2 of Investigations in Geophysics, Society of Exploration Geophysics, Tulsa, 1987.

Zagwijn W.H. The Netherlands during the Tertiary and the Quarternary : A case history of Coastal lowland evolution. Geologie en Mijnbouw, **68**, 107-120, 1989.

Ziolkowski,A. Why don't we measure seismic signatures? Geophysics, **56**, 190-201, 1991.

Samenvatting (Summary in Dutch)

Reflectie seismiek, intensief gebruikt in de olie-exploratie, geeft een nauwkeurig beeld van de ondergrond. Toepassing hiervan, met sterk verhoogde resolutie , maakt een gedetailleerde 'afbeelding' van de bovenste tientallen meters van de aarde mogelijk. Wanneer reflectie seismiek vanaf het water wordt uitgevoerd wordt het mariene seismiek genoemd. In dit proefschrift worden een aantal aspecten van de hoge resolutie mariene seismiek behandeld, in het bijzonder marien seismische bronnen en deconvolutie technieken. De laaste 3 hoofdstukken van het proefschrift beschrijven een aantal toepassingen van hoge resolutie seismiek.

Het werk in hoge resolutie mariene seismiek startte in Utrecht rond 1987. Hiertoe werden een data acquisitie systeem en een ontvanger groep (streamer) ontworpen en gebouwd. In het eerste hoofdstuk wordt de verzameling (acquisitie) van marien seismische data behandeld. Hierbij worden het acquisitie systeem en de streamer besproken. Ook wordt de relevantie van de bron-ontvanger geometrie voor de signaal-ruis verhouding behandeld. Ruis in de opgenomen data kan het gereflecteerde signaal verstoren. Daarom wordt in het eerste hoofdstuk ook gekeken naar manieren om ruis tijdens de opname van data te reduceren. Ook wordt aandacht besteed aan marien seismische bronnen en positionering tijdens de opname van data.

De seismische bron die gebruikt wordt tijdens de metingen bepaalt gedeeltelijk welke informatie over de ondergrond wordt verkregen. In hoofdstuk 2 wordt dieper ingegaan op een aantal eigenschappen van marien seismische bronnen die van belang zijn voor hoge resolutie mariene seismiek. De volgende eigenschappen worden onder andere besproken: dominante frequentie, bandbreedte van de frequentie, vorm en herhaalbaarheid van het signaal en de richtingsgevoeligheid van de bron.

Om een gedetailleerd beeld van de ondergrond te krijgen is een hoge resolutie wenselijk. Dit heeft implicaties voor de hardware, zoals besproken wordt in de hoofdstukken 1 en 2. De data verwerking van seismische gegevens heeft in het algemeen twee doelen. Ten eerste wil men de signaal-ruis verhouding verbeteren waardoor het gemakkelijker wordt het signaal (gewenst) van de ruis (ongewenst) te onderscheiden. Ten tweede wil men de resolutie van de data verbeteren om met een groter oplossend vermogen de data te interpreteren. Een veel gebruikte techniek om de resolutie te verbeteren is deconvolutie. Hierbij

probeert men in het algemeen de gereflecteerde golfvormen te transformeren naar een enkele puls op het tijdstip waarop de gereflecteerde golf arriveerde. Dit doet men omdat de aankomsttijd van een gereflecteerde golf vaak niet precies te bepalen is.

In hoofdstuk 3 wordt een iterative deconvolutie methode besproken. In deze methode wordt op een iterative manier gezocht naar een beperkt aantal reflectoren (of aankomsttijden van gereflecteerde golven). De methode start met een model waarin de posities van de reflectoren vastliggen, en bij dit reflector model worden de juiste amplitudes van de reflectoren gezocht. Dit gebeurt met behulp van Singular Value Decomposition. Deze stap wordt gevolgd door een stap waarbij de amplitudes van de reflectoren gelijk worden gehouden, maar waarbij de posities (aankomsttijden) van de reflectoren worden veranderd. Nadat de nieuwe posities voor de reflectoren zijn gevonden, worden op deze nieuwe posities nieuwe amplitudes berekend. Deze stappen worden een aantal keer herhaald totdat de reflectoren zijn geconvergeerd naar een vaste positie met een vaste amplitude.

In hoofdstuk 4 wordt een niet-lineaire deconvolutie techniek besproken. Hierbij wordt gebruik gemaakt van een "genetisch algoritme" om het reflector model te vinden. Het voordeel van deze methode is dat alleen voorwaartse model berekeningen worden uitgevoerd waardoor de methode niet gevoelig is voor instabiliteiten. Eerst worden de basis principes van genetische algoritmes besproken, te weten: bitstring model representatie, model selectie, crossover en mutatie, waarna er dieper op ieder van deze stappen wordt ingegaan. Er wordt aangetoond dat de waarden van allerlei controle parameters de uitkomst van het algoritme kunnen beinvloeden. Het is goed om een aantal verschillende "inversies" te doen met genetische algoritmen en de resultaten daarvan te combineren. Een manier van combineren wordt toegelicht waarbij men een indruk krijgt welke delen van het model goed en welke delen van het model minder goed zijn opgelost.

In de laatste drie hoofdstukken (5, 6 en 7) worden een aantal voorbeelden van hoge resolutie marien seismisch onderzoek behandeld. Hierbij worden ook kort enkele andere dataverwerkingsmethoden besproken. In hoodstuk 5 wordt een studie besproken waarin wordt gekeken of met behulp van hoge resolutie mariene seismiek uitspraken gedaan kunnen worden over de holocene sedimentaire geschiedenis van het Noordzee gebied, tot ongeveer 30 km ten noorden van de Waddeneilanden. In hoofdstuk 6 wordt de seismische studie langs de Zeeland Brug behandeld. Langs deze brug werd een boomer als bron gebruikt. Deze bron gaf hoge resolutie data maar het dieptebereik was minder dan was voorzien. Om te testen welke bronnen eventueel beter geschikt zouden zijn voor hoge resolutie

seismiek, waarbij ook een redelijke penetratie gewenst is, is een studie in het Noordzee Kanaal uitgevoerd waarbij vier verschillende bronnen zijn getest. Deze studie wordt in hoofdstuk 7 beschreven. Omdat de Rijks Geologische Dienst veel boringen langs het Noordzee Kanaal heeft is dit kanaal gekozen voor het onderzoek. Het blijkt dat een multitip sparker een geschikte bron is voor marien seismisch werk waarbij een hoge resolutie en een redelijke penetratie gewenst zijn.

Dankbetuiging / Acknowledgements

Graag wil ik van deze gelegenheid gebruik maken om alle mensen te bedanken die het mij mogelijk gemaakt hebben dit proefschrift te voltooien.

Prof. Dr. K. Helbig ben ik uitermate erkentelijk dat hij mijn promoter heeft willen zijn. Mijn begeleiders, Jan Brouwer, Tom McGee en Liesbeth Kosters, ben ik dank verschuldigd voor hun hulp tijdens mijn AIO-schap. Vooral Jan Brouwer en Tom McGee hebben mij gesteund in de laatste fase van het onderzoek. De leden van de beoordelingscommissie, Prof. D. Eisma, Prof. J.P. Henriët en Prof. J.C. Mondt dank ik voor het lezen en becommentariëren van het proefschrift.

Verschillende medewerkers van de Vakgroep Geofysica hebben bijgedragen aan de totstandkoming van dit proefschrift. Zonder de hulp van de technische medewerkers van Exploratie Geofysica, met name Henk van der Meer, was het niet mogelijk geweest de gewenste metingen te verrichten. Mijn kamergenoten tijdens mijn AIO-schap, Vincent Nijhof en Bart Posthumus, waren prettige collega's van wie ik veel heb geleerd. Filip Neele, Wim Spakman, Jaap Mondt, Kabir Roy Chowdhury, Anthony Lomax, Andrew Curtis, Dick Verwey, Joop Hoofd, Dee Pattynama en Arie van Wettum dank ik om uiteenlopende redenen voor hun bijdragen aan dit proefschrift.

Het NIOZ en de bemanning van de R.V. Pelagia en de R.V. Aurelia dank ik voor de mogelijkheden die zij mij gegeven hebben om gedurende 4 weken metingen te kunnen doen op de Noordzee.

Ik wil ook graag Bert Michels bedanken voor zijn enthousiasme en interesse tijdens de studie geofysica en mijn periode als AIO.

Tenslotte wil ik Petra bedanken voor haar steun en bemoediging in de afgelopen jaren.

Curriculum Vitae

7 September 1966	Born in Geldrop, The Netherlands
1978 - 1984	Atheneum-B, Eemland College Noord in Amersfoort
30 - 06 - 1986	Propedeutisch Examen Geophysics
27 - 06 - 1990	Doctoraal Examen Geophysics
1990 - 1994	Research Assistant (AIO) at the Department of Exploration Geophysics, Utrecht University, The Netherlands.
February 1995 - present	Post-Doctoral researcher (Toegevoegd Onderzoeker) at the Department of Exploration Geophysics, Utrecht University, The Netherlands.